Dissertation

submitted to the
Combined Faculties for the Natural Sciences and for Mathematics
of the Ruperto-Carola University of Heidelberg, Germany
for the degree of
Doctor of Natural Sciences

Put forward by
Arne Kersting
born in Warstein

Oral examination: May 09, 2018

Dating of groundwater and ocean samples with noble gas radioisotopes – sample preparation and field applications

Referees:

Prof. Dr. Werner Aeschbach

Prof. Dr. Norbert Frank

Abstract

The noble gas radioisotopes ^{39}Ar (half-life 269 yr) and ^{85}Kr (half-life 10.8 yr) are desired tracers for dating water and ice in the past 1000 years, particularly because of their conservative properties. However, their application has long been hindered due to their low isotopic abundance and consequently, large required sample sizes. Due to recent improvements of the detection method Atom Trap Trace Analysis (ATTA), dating with ^{39}Ar and ^{85}Kr on a few kilograms of water and ice has become feasible. In order to make this recent progress available for field studies, sample preparation systems for both argon and krypton have been set up and characterized. Argon purity and recovery > 95 % could be achieved as well as a krypton purity and recovery > 90%. In the course of this thesis, these sample preparation systems could be employed in three different field studies applying ^{39}Ar and ^{85}Kr among other tracers. In a groundwater study, the freshwater lens on Rottnest Island in Western Australia was investigated with a multi-tracer approach and evaluated with a lumped parameter model. Weekly atmospheric samples for ^{85}Kr were taken in Adelaide and compared to other ^{85}Kr monitoring stations. An interhemispheric exchange time of about seventeen months was derived from the data and ^{85}Kr input functions for the northern and southern hemisphere could be retrieved. The third study represents the first ^{39}Ar ocean campaign with ATTA. Twenty samples from three depth profiles near Cape Verde were taken, purified and analyzed in the context of this thesis. A fast decrease in ^{39}Ar to under 50 pmAr below 2000 m was observed and mean ages of the sampled water body were estimated by combining ^{39}Ar with CFC-12 results. The three field applications show the importance of the noble gas radioisotopes ^{39}Ar and ^{85}Kr in multi-tracer studies, especially in the light of an advancing ATTA technology.

Zusammenfassung

Die Edelgas-Radioisotope ^{39}Ar und ^{85}Kr (mit Halbwertszeiten von 269 und 10,8 Jahren) sind wertvolle Tracer für die Datierung von Wasser- und Eisproben, insbesondere wegen ihrer konservativen Eigenschaften. Ihre bisherige Anwendung war schwierig, da aufgrund ihrer geringen Isotopenhäufigkeit große Probenmengen benötigt wurden. Die stetige Optimierung der Detektiermethode Atom Trap Trace Analysis (ATTA) ermöglicht jedoch nun die Messung von ^{39}Ar und ^{85}Kr in wenigen Kilogramm Wasser oder Eis. Um diesen Fortschritt in Feldkampagnen zu nutzen, wurden im Rahmen dieser Arbeit Probenaufbereitungsanlagen aufgebaut und charakterisiert. Eine Reinheit und Ausbeute von > 95 % für Argon und von > 90 % für Krypton wurden erzielt. Weiterhin wurden drei Feldkampagnen unter dem Einsatz der Systeme durchgeführt. Mit Hilfe verschiedener Tracer wurde die Frischwasserlinse auf Rottnest Island im Westen Australiens untersucht und Daten mit einem Lumped-Parameter Modell ausgewertet. Desweiteren wurden in Adelaide wöchentlich Luftproben zur Untersuchung der atmosphärischen ^{85}Kr Konzentration der südlichen Hemisphäre genommen. Unter Verwendung weiterer ^{85}Kr Daten konnte eine zwischenhemispärische Austauschzeit von 17 Monaten berechnet und atmosphärische Eintragsfunktionen für die nördliche und südliche Hemisphäre abgeleitet werden. Die dritte Kampagne stellte die erste Ozeanstudie mit ^{39}Ar unter Verwendung von ATTA dar. Es wurden drei Tiefenprofile mit insgesamt 20 Proben in der Nähe Kap Verdes genommen, aufbereitet und evaluiert. Ein starker Abfall der ^{39}Ar Konzentration auf unter 50 pmAr unterhalb von 2000 m wurde beobachtet und mittlere Alter der Proben aus der Kombination von ^{39}Ar und CFC-12 wurden berechnet. Diese drei Studien demonstrieren die Relevanz der Edelgas-Radioisotope ^{39}Ar und ^{85}Kr, insbesondere in Hinblick auf zukünftige Anwendungen mit ATTA.

Contents

1. Introduction

Jacques Yves Cousteau, the famous marine researcher and photographer once stated solemnly: "We forget that the water cycle and the life cycle are one". This is very true in many aspects. Considering the significant groundwater depletion in already arid regions caused by excessive groundwater abstraction for agriculture, the melting of glaciers due to global warming and the pollution of surface water, one can see that humanity deprives itself and nature of this most vital resource water.

To quantify the impact of these destructive processes and to navigate into a hopefully more sustainable future, a deeper understanding of the dynamics within the affected water reservoirs is crucial. Environmental tracers and especially age tracers are useful tools to investigate these dynamics.

Whenever water is in contact with the atmosphere, it receives an imprint of the atmospheric composition through gas exchange processes. Once the water enters the interior of the ocean or an aquifer (or ice enters the interior of a glacier), it is sealed off from the atmosphere while the atmospheric signature is ideally preserved. Some substances reveal information on when the sampled water or ice was last in contact with the atmosphere. These age tracers give insight in the age distribution of a sample. It is a distribution of many different ages rather than a distinct age, as mixing is always taking place. The age distribution is an important parameter as it is linked to the flow within a reservoir.

A broad spectrum of dating tracers is used in hydrology and glaciology, all with different properties, advantages and disadvantages (Leibundgut et al., 2009). The noble gas radioisotopes ^{39}Ar, ^{81}Kr and ^{85}Kr can be considered nearly ideal tracers. Due to their inertness, their concentrations are not directly altered by biological or chemical processes in the reservoir. Their atmospheric history is well known and except few groundwater systems, the atmosphere can be considered the only source.

However, their application has long been hindered by their low isotopic abundance in the order of 10^{-15} for ^{39}Ar, 10^{-12} for ^{81}Kr and 10^{-11} for ^{85}Kr. ^{39}Ar and ^{85}Kr (half-life 269 yr and 11 yr respectively) can be measured by decay counting, but the required sample size of up to a ton of water restricted the routine application to groundwater studies. ^{81}Kr could not be measured at all by decay counting due to its very long half-life. With the advent of Atom Trap Trace Analysis (ATTA) (Chen et al., 1999) and its further optimization (Ebser, 2018; Jiang et al., 2012), the required sample sizes for all three isotopes could be reduced significantly to about 5 L of water or 2 kg of ice for ^{39}Ar, and 10-20 kg of water or ice for ^{81}Kr and ^{85}Kr. This allows the application of ^{39}Ar and ^{85}Kr in the ocean and glacier ice for the first time.

Measuring the noble gas radioisotopes can be seen as the third of four steps in environmental studies. The first step is to collect the samples. Here, new techniques have to be developed, especially for ocean and ice applications if the sampling wants to be integrated in the regular sampling procedure on board or on a glacier. Secondly, the samples have to be prepared, i.e. they have to be degassed and the argon and krypton fraction must be separated. The purified argon and krypton is then measured, either with an ATTA apparatus or, in case of sufficient gas amounts, with a decay counting method. The fourth step is the evaluation of the data and the combination with other tracer results in order to derive the age distribution of the sample. Laboratories that want to apply noble gas radioisotopes for dating must upgrade their capabilities in order to sample for argon and krypton and even more crucial, to prepare the samples for analysis with ATTA.

In the course of this thesis, methods for sampling and purifying argon and krypton have been developed for two laboratories: for the *Institute of Environmental Physics* (IUP) in Heidelberg, Germany and for the tracer laboratory of the Land and Water Department of the *Commonwealth Scientific and Industrial Research Organization* (CSIRO) in Adelaide, Australia. The applied sampling methods, developed purification setups and used detection methods are described in chapter 3. Furthermore, three studies focusing on the noble gas radioisotopes ^{39}Ar and ^{85}Kr have been conducted in the context of this thesis. In May 2016, a field campaign was performed to investigate the groundwater regime on Rottnest Island, 20 km off the coast of Perth, in Western Australia. In a multi-tracer study also applying ^{85}Kr, the island's freshwater lens was analyzed (chapter 4). During the stay in Adelaide, sampling of atmospheric air for ^{85}Kr analysis has been started. In cooperation with the *Bundesamt für Strahlenschutz* (BfS) in Freiburg, Germany, the ^{85}Kr concentration of the southern hemisphere was investigated. The analysis of the data that has been collected over more than two years is done in chapter 5. Chapter 6 reports on the first ^{39}Ar ocean campaign in ATTA-times, conducted in the context of the ocean cruise M116 in May 2015. Near Cape Verde, 24 seawater samples from 3 depth profiles were taken, purified at the IUP and analyzed with the ATTA apparatus at the Kirchhoff-Institute for Physics in Heidelberg. Finally, chapter 7 sums up the findings of this work and gives an outlook on what to expect from the application of ^{39}Ar, ^{81}Kr and ^{85}Kr in the near future.

2. Fundamentals

In the following, the theoretical basics are presented which are fundamental for the understanding of the technical and analytical methods used in this thesis. First, a short summary of the basics of the hydrological cycle is given, focusing on the three major reservoirs: the ocean, ice and groundwater. Then the tracers are introduced that were used during field campaigns to investigate the mentioned environmental reservoirs. Finally, the theory of sorption processes is explicated, which is crucial to understand the developed methods for argon and krypton purification.

2.1. The ocean, glaciers and groundwater - a short introduction

About 96.5 % of the water on our planet is salt water in the oceans. The remaining 3.5 % of fresh water is mainly stored as glacier ice and as groundwater. Water cycles through these reservoirs on very different time scales of days, between precipitation and evaporation on the oceans surface and million of years in the polar ice sheets. In the following, a brief introduction to three major reservoirs of the hydrological cycle is given: the ocean, groundwater and glaciers. The section mainly focuses on the hydrodynamics within these reservoirs as the dating methods that are applied in the framework of this thesis are key techniques to investigate these dynamics.

2.1.1. Basics of physical oceanography

The following section will focus on the hydrodynamics in the ocean, particularly on the large scale ocean circulation, that is often referred to as the global conveyor belt. Better defined terms are the meridional overturning circulation (MOC) or the thermohaline circulation. Giving a detailed introduction into this topic would go beyond the scope of this thesis, so the focus will rather be on introducing the main concepts behind the ocean dynamics on a qualitative level. The section mainly follows Stewart (2008).

At first, a few general statements. There is only one ocean which is divided into three parts named the Atlantic, Pacific and Indian Ocean by international agreement. Together with the seas it covers 70.8 % of the Earth's surface. The ocean's typical mean depth is between 3-4 km. Considering its horizontal dimensions of several thousands of kilometers, the ocean forms a thin layer on top of the oceanic crust. Because of that, the vertical scale of cross-sectional plots of ocean basins are often 200

times the horizontal scale and what appears as steep cliffs at the edges of the ocean basins are in general gentle slopes.

The ocean plays an important role in the Earth climate as its currents transport substantial amounts of heat from the tropics to higher latitudes and it acts as a major sink for carbon dioxide. Ocean currents can be subdivided into ocean surface currents which are wind driven, and the deep ocean currents or thermohaline currents which are driven by density gradients. Before getting into the specifics of these currents, a brief discourse on the density of water and on the concept of water masses is helpful.

The density of water is in most cases not measured directly, but derived from its temperature, salinity and pressure. The function $\rho(T, S, p)$ is called the equation of state of water and its accurate determination has been subject to lots of research over the last decades (Millero, 2010). A detailed explanation of the widely accepted determination of the equation of state, the *Thermodynamic Equation of Sea Water 2010* is found in McDougall et al. (2009).

In the context of this thesis, an approximation of the effect of temperature, salinity and pressure on the density of water is sufficient. The change in density of water with changing parameter T, S or p is expressed through

$$\alpha(T) = -\frac{1}{\rho}\left(\frac{\delta\rho}{T}\right)_{\mathrm{S,p}} [\mathrm{K}^{-1}] \;\; ; \;\; \beta_{\mathrm{S}} = \frac{1}{\rho}\left(\frac{\delta\rho}{S}\right)_{\mathrm{T,p}} [‰^{-1}] \;\; ; \;\; \gamma = \frac{1}{\rho}\left(\frac{\delta\rho}{p}\right)_{\mathrm{T,S}} [\mathrm{Bar}^{-1}] \tag{2.1}$$

with α : thermal expansion coefficient
β_{S} : saline contraction coefficient
γ : isothermal compressibility coefficient

As the sign of the coefficients indicates, the density of water increases with increasing pressure and salinity, and with decreasing temperature. Fresh water under ambient pressures has its maximum density ($\alpha(T_{\max}) = 0\,$℃) for $T_{\max} \approx 4\,$℃ with $\rho_0 = 999.972\,\mathrm{kg/m^3}$, whereas $T_{\max}$ decreases with increasing salinity.

Ignoring the compressibility of water, the density can be calculated in good approximation as

$$\rho(T, S) = \rho(T)(1 + \beta_{\mathrm{S}} S) = (\rho_0 - 7 \cdot 10^{-3})(T - T_{\max}) \cdot (1 + \beta_{\mathrm{S}} S) \tag{2.2}$$

β_{S} depends on the composition of the salts contained in the water and is for seawater ~$7.6{\cdot}10^{-3}\,‰^{-1}$. The typical density of water at the sea surface is $1027\,\mathrm{kg/m^3}$. Oceanographers often quote only the last two digits and refer to the quantity as

$$\sigma(S, T, p) = \rho(S, T, p) - 1000\,\mathrm{kg/m^3} \tag{2.3}$$

There are different ways to define and measure the salinity. It is most commonly defined as the total

amount of dissolved salts per gram in one kilogram of water, mostly written in units of [‰]. The definition of *practical salinity* from 1978 defines the salinity of a water sample only via its conductivity in relation to a specific standard (Lewis, 1980). This *Practical Salinity Scale* is currently the most common method to determine the salinity of seawater.

Especially when going to a greater depth, water can no longer be assumed as an incompressible medium. As a rule of thumb, the pressure increases with every 10 m of depth by about 1 Bar. This pressure increases the density of ocean water according to $\gamma = 45 \cdot 10^{-6}$ Bar^{-1} (for $T = 5$ °C, $S = 35$ ‰, $p = 1$ atm, after Lepple et al. (1971)). Pressure differences within the ocean, caused by density differences of water masses, are the driving force of ocean dynamics, as water that is less dense than its environment rises and vice versa. When the density of water parcels of different depth are compared, the density increase due to the pressure increase is an effect that must be corrected for in order to investigate stratification and ocean dynamics.

When a water parcel sinks, its compression causes a rise of the *in situ* temperature. Assuming the compressed water parcel does not exchange heat with its environment, its increase in temperature is expressed through the lapse rate Γ:

$$\Gamma(T, S, p) \equiv -\frac{\alpha g T^*}{c_\mathrm{p}} \tag{2.4}$$

with T^* : absolute temperature [K]
c_p : heat capacity of water at constant pressure

To correct for this effect, the concept of *potential temperature* (Θ) is used. It is defined as the temperature a water parcel at depth z would have, if brought adiabatically to a reference depth z_0, which is the ocean surface in most cases:

$$\Theta(z, z_0) = T(z) - \int_\mathrm{z}^{\mathrm{z_0}} \Gamma(\Theta(z, z'), S(z), p(z'))dz' \tag{2.5}$$

This leads to the definition of *potential density*

$$\sigma_\Theta = \sigma(\Theta, S, p(z_0)) \tag{2.6}$$

When comparing water from great depth it is not useful to choose the surface as the reference depth, but rather a depth z_0 close to z, as the definition of potential density ignores the effects of pressure on the coefficients α and β.

The salinity and (potential) temperature are characteristics of a water parcel, giving it a specific density. Therefore, it is located at a specific depth in the ocean, above water with higher density and below water with lower density. This leads to the concept of water masses. Tomczak (1999) defines water masses as "a body of water with a common formation history, having its origin in a particular

region of the ocean.[...] A source region or formation region of a water mass is that part of the worlds ocean where a water mass attains its characteristic properties.[...] A conservative property is a water mass characteristic or property which has no sources or sinks in the ocean interior". For the deep ocean, temperature and salinity are conservative tracers. As seen in Figure 2.1, there are only a few formation regions for deep ocean water where it accquires its characteristic T and S signature.

The mean temperature of the ocean's water is $T = 3.5\,°\mathrm{C}$ and the mean salinity is about $S = 34.7\,‰$ with 50 % of the water being in the range of:

$$\begin{aligned} 1.3\,°\mathrm{C} < T < 3.8\,°\mathrm{C} \\ 34.6\,‰ < S < 34.8\,‰ \end{aligned} \tag{2.7}$$

To understand large scale ocean dynamics, it is important to realize that basically all forcing on the ocean originates from the atmosphere. This forcing happens via three physical processes: Heat transfer, precipitation/evaporation and wind stress. Only a comparably thin layer of maybe 30 to 300 m of the upper ocean is directly influenced by the atmosphere, hence the ocean's interior is affected only indirectly by the processes started in the upper layer (Stewart, 2008).

Heat transfer changes the water's temperature and with that its density. Depending on the latitude, the upper hundred meters are characterized by a temperature dependent stratification with a relatively homogeneous warm upper layer mixed by the wind, followed by the thermocline with steep temperature gradients isolating the underlying water masses from the direct influence of the atmosphere. In higher latitudes the heat flux from the ocean into the atmosphere cools the water and with that increases its density.

Precipitation and evaporation can be interpreted as an addition or subtraction of fresh water, changing the salinity. This is the reason why the Mediterranean Sea has such a high salinity and water flowing out of the Straight of Gibraltar, although warm, sinks down to its corresponding layer of equal density. In the Labrador Sea, one of the main formation regions for deep ocean water, it is not only the cooling that increases the waters density, but also the formation of ice which by fresh water extraction leads to an increase in density.

The third atmospheric forcing is the wind stress. It is responsible for the ocean surface currents like the Gulf Stream, just to mention the most prominent example. How the wind drives the major ocean currents can not be easily understood by looking at a map showing the winds over the ocean, which also changes during the seasons. It must be seen as a chain of events. Focusing on the Atlantic on the northern hemisphere and starting in low latitudes close to the equator: Strong and constant easterly winds move large water masses. But the wind stress is not the only force affecting the water masses. The Coriolis force and the friction result in a net flux perpendicular to the wind direction. This is

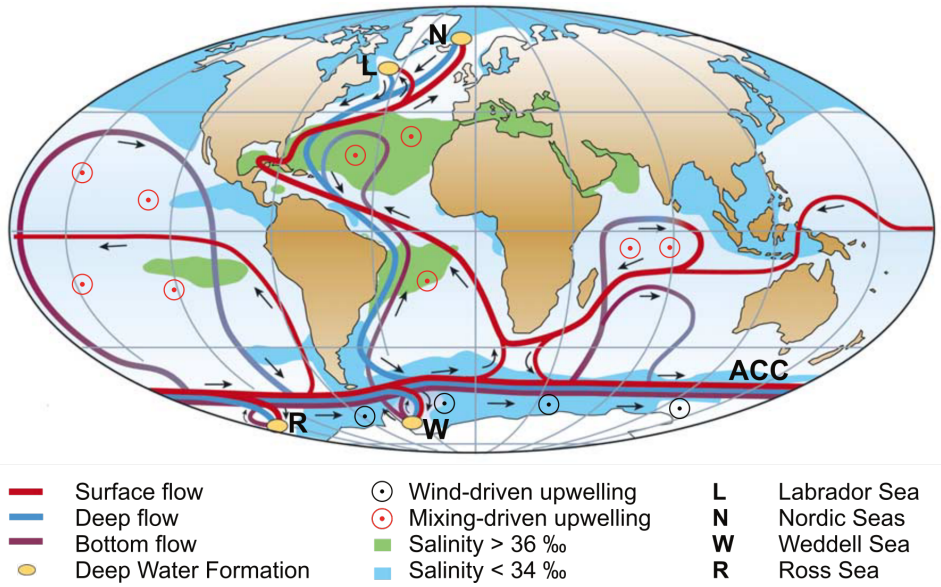

Figure 2.1.: The interconnection of major currents in the ocean, often referred to as the global conveyer belt and the salinity distribution in the ocean after Kuhlbrodt et al. (2007). ACC stands for Antarctic Circumpolar Current, a current that connects all three parts of the ocean.

called the *Ekman Balance* leading to a 90° net flux to the right of the wind direction on the northern hemisphere and to the left on the southern hemisphere. This affects the water column down to the so called *Ekman depth* which depends on the wind speed and the latitude and goes down to typically a few hundred meters. The next step in the chain of events is a piling up of water masses to the right of the wind, leading to an ocean topography which is nowadays even detectable by satellites. Although the 'hill' of water is only in the order of a few centimeters, the large water amounts result in a horizontal pressure gradient which causes a geostrophic current. It is a stationary current where pressure gradients and Coriolis force balance each other. Because of the perpendicular Coriolis force, it finally becomes a clockwise current. The last factor is the geographical structure of the ocean basin, so the coastlines, which are forcing the water masses in a specific direction. All this is leading to the so called *North Atlantic Gyre*, a gigantic clockwise current of which the gulf stream is the most pronounced one.

All these effects can be described quantitatively by the equation of motion of water, which is the so called Navier-Stokes equation. The brief explanation follows Stewart (2008).

For fluid mechanics and from a Lagrangian perspective one can write Newton's second law as

$$F = \rho \cdot V \left(\frac{d\vec{v}}{dt} \right) . \tag{2.8}$$

Transforming the Lagrangian total derivative into the Euler system leads to

$$\vec{a} = \frac{d\vec{v}}{dt} = \frac{\partial \vec{v}}{\partial t} + (\vec{v} \cdot \nabla)\vec{v}. \tag{2.9}$$

The relevant forces acting on a water parcel are pressure gradients, Coriolis force, gravity and friction. The force per mass, or the acceleration of a water parcel can then be described by the Navier-Stokes equation for incompressible fluids:

$$\frac{d\vec{v}}{dt} = \frac{\partial \vec{v}}{\partial t} + (\vec{v} \cdot \nabla)\vec{v} = \underbrace{-\frac{1}{\rho}\nabla p}_{\text{pressure}} - \underbrace{2\vec{\Omega} \times \vec{v}}_{\text{coriolis}} + \underbrace{\vec{g}}_{\text{gravitiy}} + \underbrace{\nu \Delta \vec{v}}_{\text{friction}} \tag{2.10}$$

with Ω : angular velocity vector of Earth
ν : viscosity
g : gravitiy

This is a non-linear partial differential equation and practically impossible to solve. Analytical solutions can be found for a few special cases. Two of these cases are the geostrophical balance and the Ekman balance that were described earlier. Both cases assume a steady homogeneous horizontal flow on a rotating Earth. The geostrophic flow is a result of a balance between horizontal pressure gradients and Coriolis force whereas the Ekman current is a result of the balance between frictional and Coriolis forces. The calculations are not needed in this thesis and can be found in any book about fluid mechanics, e.g. Stewart (2008).

As stated above, the direct impact of the wind only affects the Ekman layer, so down to a few hundred meters maximum. The secondary effect, the geostrophic flow triggered by the pressure gradient, goes down to about thousand meters. Beneath that depth the deep ocean begins and with that, a different circulation regime: the thermohaline deep ocean currents. As pictured in Figure 2.1, there are only a few locations where deep water is formed which is in the pole regions in the north Atlantic (mainly the Labrador Sea and the Nordic Sea) and in the Antarctic. The processes behind the formation were mentioned already. The water gets denser due to the colder temperatures and saltier due to the removal of fresh water by forming new ice. This leads to the formation of distinct water masses with particular T-S signatures but also specific oxygen or phosphate content. In Figure 2.2 the major water masses in the deep Atlantic Ocean are shown.

Temperature, salinity and other tracers like oxygen are very useful to identify these water masses. However, they can give only very limited information concerning the dynamics in the deep ocean. While surface currents like the gulf stream have velocities of up to several meters per second, the deep ocean circulation is by one to two orders of magnitude slower in most regions. That makes age tracers so valuable, especially ^{39}Ar, as water masses here have typical residence times of several hundreds of years, which is well covered by the dating rage of ^{39}Ar.

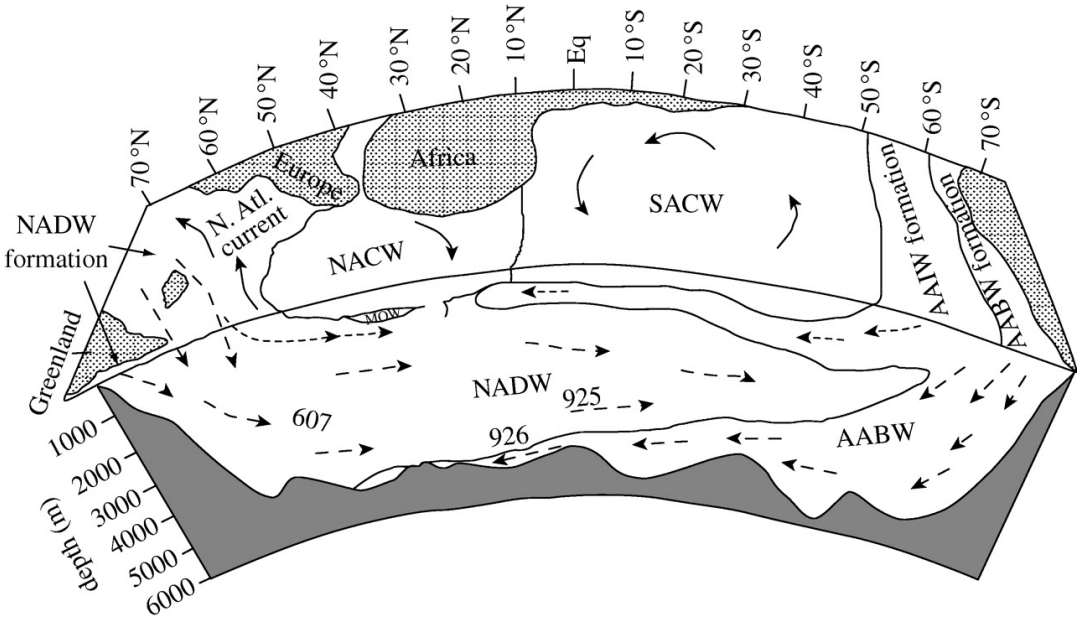

Figure 2.2.: A cross-section of the Atlantic showing the main water masses, the North Atlantic Deep Water (NADW), the North Atlantic Central Water (NACW), South Atlantic Central Water (SACW), Antarctic Intermediate Water (AAIW) and the Antarctic Bottom Water (AABW), after Pickard et al. (2016) and Dwyer et al. (2002).

2.1.2. Basics of groundwater hydrology

Roughly 30 % of the Earth's freshwater is stored in the form of groundwater, which makes it an extremely valuable resource and with that, important to manage especially in regions suffering from water scarcity. Groundwater refers to all water beneath the Earth's surface that fills up the soil pore space or fractures of rock formation. Its origin is precipitation infiltrating the ground, either directly via surface waters or as melted ice. This happens in the recharge area. When water infiltrates the soil, it passes the unsaturated zone in which not all pore space is filled with water. This is where the water last equilibrates with the atmosphere. The water table is defined as the depth in which the complete pore space starts to be filled with water. Beneath the water table lies the saturated zone.

Layers of higher permeability, consisting of gravel, sand or fractures in the rock in which the groundwater can flow, are called aquifers. Nearly impermeable layers, often clay or closed rock formations, are called aquitards. Those aquitards often close off deeper aquifers and prevent mixing as well as balancing of pressure gradients between different aquifer layers. As seen in Figure 2.3, this leads to the distinction between *confined* and *unconfined* aquifers. Confined means that the aquifer has a higher internal pressure so that the water within a well tapping the aquifer will rise above its upper boundary. The height of the resulting water level in the well is called the hydraulic head or potentiometric height of the confined aquifer at that location. Its height depends on the height difference of the recharge area

to the well, the flow resistance in the aquifer and the geological formation limiting the dimensions of the aquifer. Unconfined is an aquifer according to that definition when its hydraulic head is equal to its upper boundary, which is typically the case for the topmost aquifer with the water level equal to its potentiometric height.

The expression *artesian well* is not used consistently by groundwater hydrologists. In English literature it mainly refers to a well drilled in a confined aquifer with the special case of a flowing artesian well as one with a hydraulic head above the Earth surface. In the German groundwater community, a well is only artesian when its water reaches the Earth surface without pumping, so corresponding to a flowing artesian well in English literature.

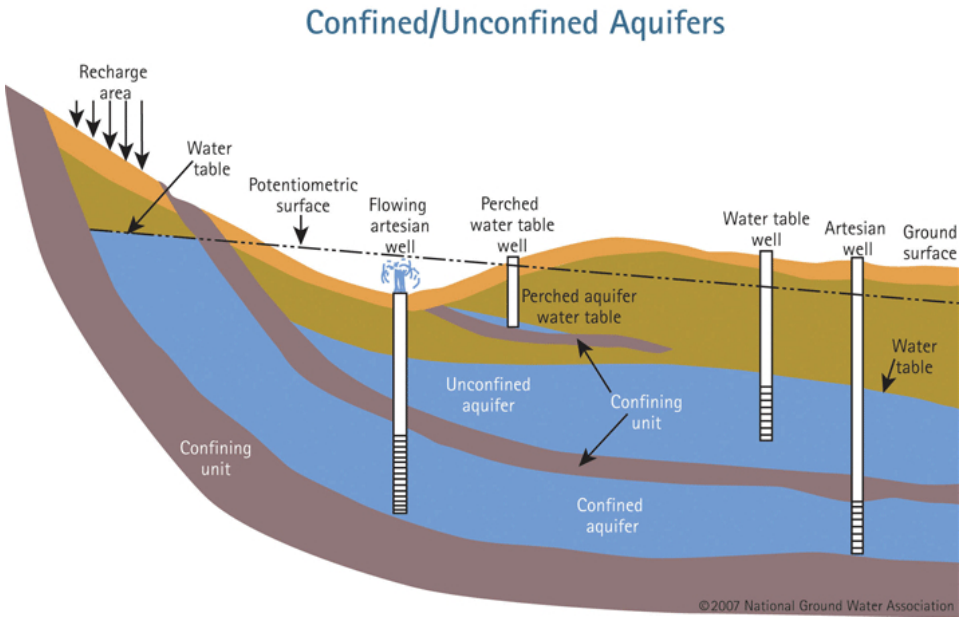

Figure 2.3.: Sketch showing the different types of aquifers and wells in a groundwater system (National, 2015).

By measuring the hydraulic heads of enough wells tapping an aquifer, one can extrapolate the so called potentiometric surface of an aquifer. The groundwater flow is driven by the gradient of that potentiometric surface while its velocity is determined by the permeability of the porous medium the water flows through. This is described by Darcy's law, here in one dimension:

$$q = \frac{Q}{A} = -K\frac{\mathrm{d}h}{\mathrm{d}l} \qquad \left[\frac{\mathrm{m}}{\mathrm{s}}\right] \tag{2.11}$$

with the Darcy velocity q describing a water flux Q through a cross-sectional area A. This velocity is proportional to the hydraulic head gradient. The parameter K (a three-dimensional tensor) is called the hydraulic conductivity and varies drastically for different soil components between 10^2 m/s for gravel and 10^{-13} m/s for crystalline rock (Aeschbach-Hertig, 2012).

The time since rain water was last in equilibrium with the atmosphere, or to be more precise, the time since the last equilibration of the infiltrated water with the soil air in the unsaturated zone took place, to the moment of sampling the water from a well, refers to something like an age of that sampled water body. The term age is misleading as many processes in the subsurface lead to mixing either within an aquifer, or even with adjacent aquifers (Suckow, 2014b). This leads to an age distribution within a water parcel. Multi tracer approaches are required to get an idea of the 'true' age distribution of a water body, which is discussed in more detail in section 2.3

Beside its crucial role as freshwater supply and source for irrigation in agriculture, groundwater is an important climate archive as it preserves a climate signal from the time and location it was formed. The mean age, or mean residence time of aquifers lies on the timescale of decades for shallow aquifers close to the recharge area and on timescales of up to millions of years in deep large basins like in some areas of the great artesian basin in Australia (Torgersen et al., 1991) or in the Nubian Aquifer in Egypt (Sturchio et al., 2004). Hence, groundwater studies can deliver valuable contributions to paleoclimate reconstructions over large time scales.

2.1.3. Basics of glaciology

60 % of the Earth freshwater is present in the form of ice. It covers approx. 10 % of the Earth surface and is present in different forms. Sea ice is mostly formed seasonally in the polar regions when the water temperature sinks below roughly -2 °C which is the melting point of ocean water due to its salinity. Glacier ice originates from precipitation of snow. If it covers an area larger than 50,000 km^2 these ice masses are called ice sheets, while smaller ice masses are called ice caps (Cuffey et al., 2010). Since the beginning of the Holocene (i.e. since the end of the Last Glacial Maximum (LGM) 12,000 yrBP), the only existing ice sheets are in Antarctica and Greenland. Glaciers are bodies of dense ice that are constantly moving due to pressure gradients. The terminology is not always clear as ice sheets and caps are moving too but often only when their ice masses reach the rim of a continent or flow down a valley they are called glaciers. As ice samples analyzed in this thesis are all coming from alpine glaciers, ice sheets, ice shelfs, sea ice and other objects of the cryosphere like permafrost won't be further investigated.

Before classifying different glaciers depending on their zones and describing their dynamics, first a short excursion on the terminology snow, firn and ice.

It is hard to have clear definitions especially for firn. While the term snow is used as long as it has not much changed after precipitation, firn is the in-between state denser than snow, but not yet ice. Dense firn or frozen water is called ice when the entrapped air or water bubbles are completely closed off from one another and the atmosphere. This occurs at densities of 830 kg/m^3. A list of typical densities is shown in table 2.1.

Table 2.1.: Typical densities taken from Cuffey et al. (2010)

Material	density [kg m^{-3}]
New snow	50-70
Damp new snow	100-200
Wind-packed snow	350-400
Firn	400-830
Glacier ice	830-923

The formation process of glacier ice from snow is a process of densification. It occurs on the one hand due to increasing pressure with more snow piling up and on the other hand by melting. The process of densification highly influences the amount of air that is entrapped in the final ice. Assuming that a fraction μ of the glacier ice is bubbles, the density of glacier ice is then

$$\rho = \mu\rho_\mathrm{b} + (1-\mu)\rho_\mathrm{i}, \tag{2.12}$$

with ρ_b for the density of the medium filling the bubble, usually air or water, and ρ_i for the density of bubble free glacier ice. For temperatures near the melting point and nearly atmospheric pressures, a typical value of 917 kg/m^3 is taken. The maximum value of 923 kg/m^3 given in Table 2.1 is only found in the center of ice sheets at low temperatures and high pressures.

Glacier ice with densities as low as 830 kg/m^3 therefore contains 10 % air bubbles. These large amounts of entrapped air are only found when the ice is formed out of new snow under dry conditions, which means under temperatures permanently beneath the melting point. In alpine glaciers this is typically not the case. Melting speeds up the process of densification but reduces the amount of entrapped air through denser packing. Often layers of pure ice can be found in mountain glaciers formed by melt water that refroze.

Entrapped air bubbles contain a climate signal from the time the glacier ice was formed. It is important to keep in mind, that this is not the same time the surrounding ice snowed down. In the state of firn, the passageways between the bubbles are not yet sealed off and with that, the air in the bubbles is still in equilibrium with the atmosphere. The firn-ice transition occurs at a specific depth depending on the region on Earth. The age of the firn or ice at this transition depth varies drastically depending on the rate of snow accumulation and the temperature conditions. An extreme example is the Vostok station, in the dry-zone in central Antarctica. Here, the transition from firn to ice takes place at a depth of 95 m and it takes the ice roughly 2500 years to get to this depth, which gives an enormous offset to potential ^{39}Ar data. Due to a higher snow accumulation rate and warmer conditions, the firn-ice transition depth is around 10 to 40 meters in alpine regions which corresponds to not more than a few decades of age difference between the entrapped air and the surrounding ice (Cuffey et al., 2010).

Instead of categorizing glaciers according to their ice temperature or amount of melting, the ideas

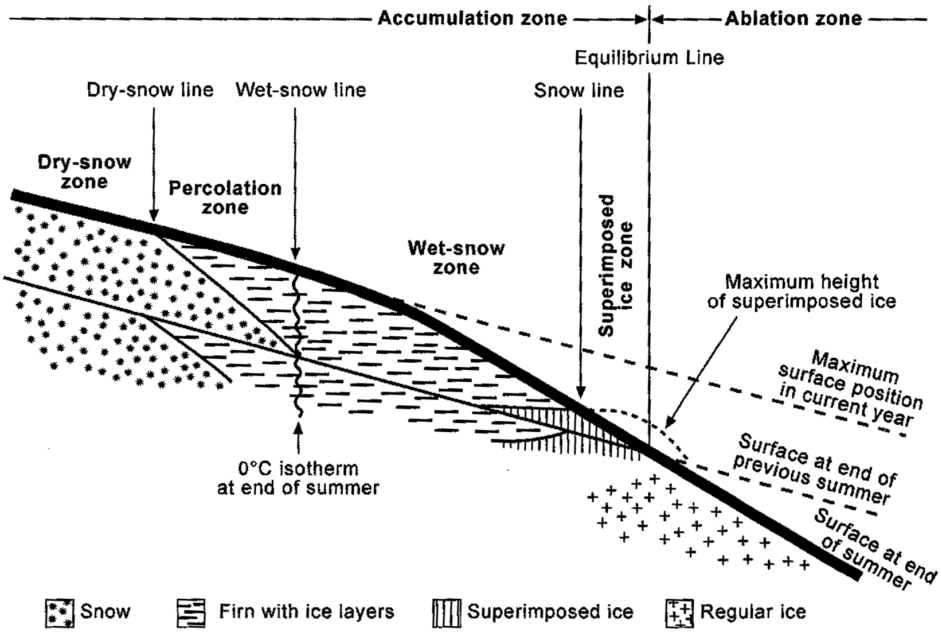

Figure 2.4.: The five zones of a glacier after Benson and Müller taken from Cuffey et al. (2010, S.14).

of zones developed by Müller (1962) and Benson (1962) will be presented. Figure 2.4 shows these zones and their boundaries although most glaciers do not have the whole sequence of zones with these idealized boundaries.

The first zone is the *Dry-snow zone*. Throughout the year no melting occurs here and the topmost layers consist of dry snow. Glaciers having this zone exist only in the interiors of Greenland, Antarctica and on the highest summits of the Himalaya. The dry-snow line marks the boundary to the next zone, the *Percolation zone*. It is characterized by melt water on the surface during the summer that infiltrates down the uppermost layers and refreezes there forming ice layers and ice lenses. But still even at the end of the summer, most of the material accumulated since the last summer is beneath the melting point. Both the percolation zone and the adjacent *Wet-snow zone* mainly exist out of firn and ice layers, but the latter is characterized by the fact, that at the end of the summer, all material accumulated since the last summer is at melting point and that the melt water percolates down to deeper layers of former years. The fourth zone is the *Superimposed-ice zone*. Here, no more firn is present and the melt water and ice layers merge to a continuous mass called superimposed ice. The boundary separating *Wet-snow zone* and *Superimposed-ice zone* is the Snow line. It can be easily seen at the end of the summer as it marks the boundary between firn and ice on the glaciers surface. All these zones are part of the *Accumulation zone*, which is the part of the glacier which gained mass at the end of one seasonal cycle. The fifth and last zone is called the *Ablation zone*. It is separated from the first four zones by the equilibrium line and is characterized by a net loss of mass at the end of a seasonal cycle. It consists of regular ice with streams of melt water forming channels and ponds.

Glaciers are constantly in motion. The positive mass balance in the accumulation zone and the negative one in the ablation zone as well as the location at slopes result in pressure gradients and gravitational forces. The motion of glaciers can be subdivided into deformation within the glacier and the basal slip. The latter summarizes two effects of a glacier moving relative to the underlying rock bed. Either the base of a glacier melts and is then slipping on its melt water, or the glacier's base is frozen to the underlying rocks and gravel and those rocks move relative to the solid ground. Both effects are summarized as basal slip. Deformation within the glacier means, that the ice itself can be seen as a viscous fluid creeping down the slope. Both effects are highly temperature dependent as for example the viscosity of the ice is increased by a factor of 5 when ice gets cooled from -10 °C to -25 °C (Cuffey et al., 2010). The flow velocities of glaciers range from a few meters up to several kilometers per year depending on the bed structure, the steepness of the slope, the temperature and the glaciers mass balance.

An ice parcel that enters the interior of a glacier at a specific elevation in the accumulation zone travels along flow lines and reaches the surface at a specific elevation in the ablation zone. In this idealized picture and for a stationary glacier, one expects an increasing age at the surface of the ablation zone with increasing distance from the equilibrium line. This is a practical way to sample large amounts of ice without drilling as blocks can easily been cut out of the surface in the ablation zone in different distances from the equilibrium line.

2.2. Age tracers in environmental physics

Water reservoirs as objects of research in geoscience can be studied in many aspects. Oceanographers are interested in the ocean circulation, its storage capacity for anthropogenic greenhouse gases and regional changes in the chemical compositions within the ocean. Local water suppliers depending on groundwater are interested in the vulnerability of an aquifer to contaminants and in the storage capacity and recharge rates of aquifers. In glaciology, the growth-rate and flow behavior of glaciers are of interest and for climate studies, ocean, groundwater and glaciers are important climate archives. For all these topics and disciplines an information on age, meaning the time since the water was last in contact with the atmosphere, is of great importance.

In this section a selection of the most prominent age tracers is presented, which were also applied or worked with in the context of this thesis. After describing dating principles in general, the single tracers are introduced.

In Figure 2.5, the dating tracers used in this thesis are displayed along the age range they cover. These tracers can be subdivided into young tracers covering the last 60 years and old tracers in the range of thousands to millions of years. ^{39}Ar can be seen as intermediate tracer as it is the only tracer filling the gap of 50 to 1000 years. In some groundwater studies, the accumulation of ^{4}He allows for dating in the

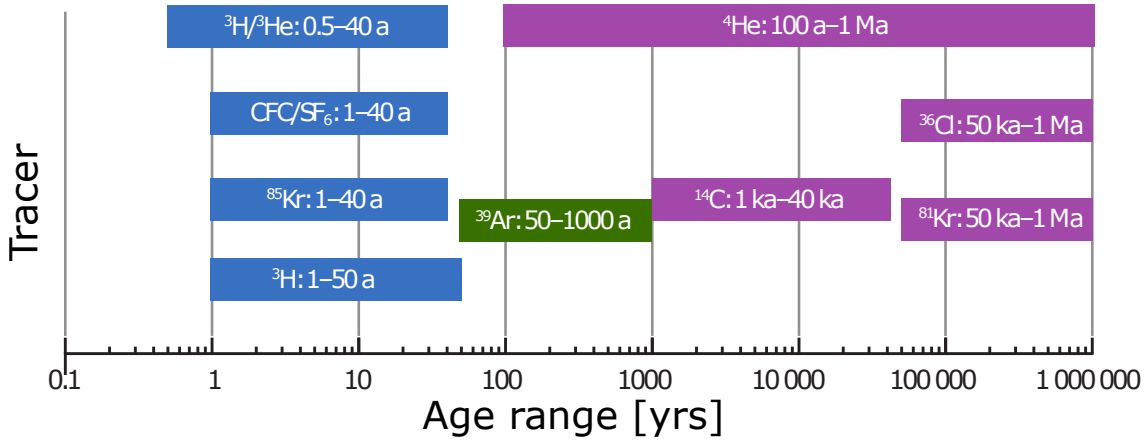

Figure 2.5.: Tracers in hydrology after Aggarwal (2013).

same range, as will be explicated later.

Age tracers can as well be categorized according to the underlying dating technique. As displayed in Figure 2.6, one can distinguish four concepts.

Radioactive decay

The initial amount N_0 of a radioactive tracer decreases exponentially through radioactive decay depending on its decay constant λ or with its half-life $T_{1/2}$:

$$N(t) = N_0\, e^{-\lambda t} = N_0 \cdot 2^{-t/T_{1/2}} \tag{2.13}$$

The relevant decay types of the applied tracers are:

$$\begin{aligned} \alpha - \text{decay}: &\quad {}^{\text{A}}_{\text{Z}}X_{\text{N}} \rightarrow {}^{\text{A-4}}_{\text{Z-2}}Y_{\text{N-2}} + \alpha &\qquad \alpha = {}^{4}_{2}\text{He}_2 \\ \beta^- - \text{decay}: &\quad n \rightarrow p + e^- + \overline{\nu_e} &\qquad {}^{\text{A}}_{\text{Z}}X_{\text{N}} \rightarrow {}^{\text{A}}_{\text{Z+1}}Y_{\text{N-1}} \\ \beta^+ - \text{decay}: &\quad p \rightarrow n + e^+ + \nu_e &\qquad {}^{\text{A}}_{\text{Z}}X_{\text{N}} \rightarrow {}^{\text{A}}_{\text{Z-1}}Y_{\text{N+1}} \end{aligned} \tag{2.14}$$

with
X : radioactive mother atom
Y : daughter atom
p, n : proton, neutron
Z, N, A : number of protons, number of neutrons, number of nucleons
ν_e, $\overline{\nu_\text{e}}$: electron-neutrino, anti electron-neutrino

A radioactive isotope can have one or more of the following four sources: It can be *primoridal*, meaning it was already present during the formation of the Earth. The isotope can be *cosmogenic*,

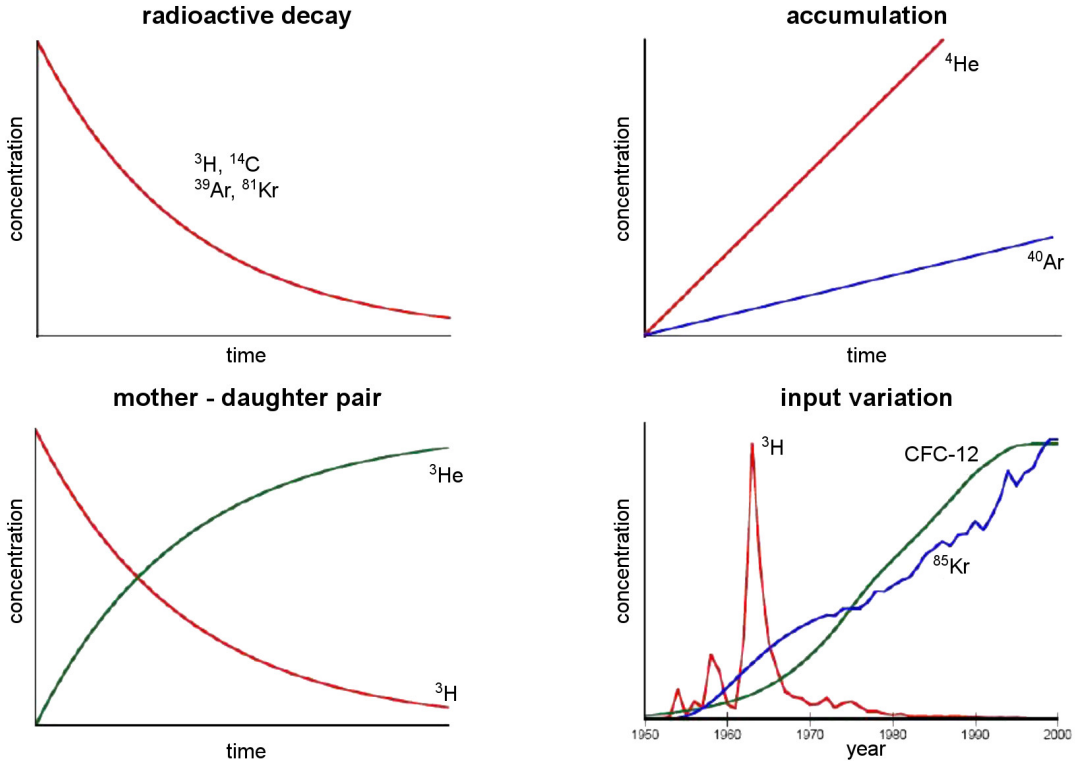

Figure 2.6.: Illustration of the 4 dating principles for age tracers (Aeschbach-Hertig, 2012).

meaning a product of high energetic cosmic rays interacting with the atmosphere. It can be built in *subsurface production* or it can be of *anthropogenic* origin.

^{39}Ar is an example for a radioactive tracer with nearly perfect properties. For most applications it can be considered as purely cosmogenic with an almost constant atmospheric concentration over the past thousand years (Oeschger et al., 1974). That means one has a well known boundary condition N_0 and once a water or ice parcel enters the interior of the ocean, aquifer or glacier, ^{39}Ar concentrations only depend on the flow dynamics within the systems and its half-life of 269 years.

In contrast, ^{14}C as tracer for groundwater dating is an example for a tracer that is hard to interpret. It is of cosmogenic and anthropogenic origin, is influenced by chemical reactions, and its relative concentration (to ^{12}C) often depends on biological and geological subsurface processes. This makes it hard to determine the initial infiltration concentration and to distinguish the depletion through radioactive decay from that of dilution.

Mother-daughter pair

When a radioactive tracer has a non-unique or not well known input function and low concentrations, one can use its decay product in addition to derive its initial input concentration. Taking tritium and its decay product helium-3 as an example: Once the ^{3}H and the ^{3}He$_{\text{trit}}$ concentration, as result of tritium

decay, is known, one can determine the tritium age without any knowledge of the input function as

$$t = \lambda^{-1} \ln \left(\frac{^3\mathrm{He}_{\mathrm{trit}}}{^3\mathrm{H}} + 1 \right) \tag{2.15}$$

The hard part is to distinguish the different sources of ^{3}He to determine the tritiogenic $^3\mathrm{He}_{\mathrm{trit}}$ concentration (Solomon et al., 2000; Aeschbach-Hertig, 1994).

Accumulation

Subsurface production of stable isotopes increases their concentration over time. For example, in the decay chain of ^{238}U, 8 α particles are emitted. Assuming constant soil composition of an aquifer one can in principle determine the slope of the ^{4}He accumulation in time. Then, by using an absolute age tracer, one can calibrate the accumulation rate and derive absolute tracer ages from the ^{4}He concentration in a groundwater sample. In most cases the assumption of a constant input over a larger area in an aquifer is not justified but ^{4}He data can still deliver valuable additional information in multi-tracer approaches (Aggarwal et al., 2012).

Input variation

The last dating principle is based on a varying but well known (atmospheric) input function. Prominent examples are chlorofluorocarbons (CFCs) which were widely used since the 1950s as refrigerants. In the simplest case, the concentration in a sample can directly be related to a year with the corresponding atmospheric concentration. This only works as long as the atmospheric concentrations are unique which is the case as long as the atmospheric concentration of a conservative tracer is constantly rising.

When it was discovered that CFCs contribute significantly to ozone depletion, their emission was regulated resulting in a decreasing atmospheric concentration of most CFCs. The peak of the atmospheric concentration in CFC-11 was around 1995 (Plummer et al., 2006). Hence, CFC-11 in samples might lead to non-unique formation times. For radioactive tracers as ^{85}Kr it is relevant that all decay corrected concentrations can be clearly assigned to one specific tracer age.

2.2.1. The noble gas radioisotopes ^{39}Ar, ^{81}Kr and ^{85}Kr

As noble gas isotopes, ^{39}Ar, ^{81}Kr and ^{85}Kr are of special interest for dating environmental samples as they have nearly ideal tracer properties (Lu et al., 2014). Due to their chemical inertness, their initial concentration is altered neither by chemical nor by biological processes. Beside some geological formations as investigated by Loosli et al. (1989), underground production is negligible and the atmospheric concentration for ^{39}Ar and ^{81}Kr is well known. Gaps of the atmospheric ^{85}Kr input function on the southern hemisphere are covered within the framework of this thesis chapter 5.

^{39}Ar

The detection of ^{39}Ar was first reported by Brosi et al. (1950) who radiated potassium with neutrons triggering the ^{39}K(n,p)^{39}Ar reaction. In nature ^{39}Ar is mainly produced via cosmic ray induced spallation in the upper atmosphere (Loosli, 1983). Its isotopic abundance was measured in 1969 by Loosli et al. (1969) via Low-Level counting to be $^{39}\mathrm{Ar/Ar} = (8.1 \pm 0.3) \cdot 10^{-16}$ and was recently confirmed in the context of the application of ^{40}Ar for a dark matter detector (Benetti et al., 2007). ^{14}C measurements on tree rings indicate variations of this isotopic ratio of up to 7 % within the last 1000 years due to fluctuations in cosmic ray flux (Oeschger et al., 1974).

^{39}Ar β-decays with a half-life of 269 years to ^{39}K. As seen in Figure 2.5, ^{39}Ar is practically the only available tracer in the age range of 100 to 1000 years, filling the dating gap between 'young' tracers like ^{3}H and 'old' tracers like ^{14}C, which makes it an extremely valuable tool for the geoscience community. Because of its low solubility, 99 % of all argon resides in the atmosphere while basically all of the remaining 1 % is stored in the ocean (excluding the argon in the Earths crust and mantle). In contrast to that, ~93 % of the ^{14}C inventory resides in the ocean, ~2 % in the atmosphere and ~5 % in the biosphere (Levin et al., 2000).

^{81}Kr

In 1950, Reynolds (1950) discovered ^{81}Kr after neutron activation of a bromine target. Similar to ^{39}Ar, ^{81}Kr is mainly produced in the upper atmosphere by proton and neutron-induced spallation of other krypton isotopes (Kutschera et al., 1994). With a half-life of $(2.29 \pm 0.11) \cdot 10^5$ yr (Baglin, 1993) it is a much desired tracer for dating samples in the age range of up to a million years. The long half-life combined with its low isotopic abundance of only $(5.2 \pm 0.4) \cdot 10^{-13}$ (Collon et al., 2004) makes decay counting as a detection method for ^{81}Kr extremely time consuming and routine application virtually impossible. This is why the first application of dating with ^{81}Kr, a groundwater study in the Great Artesian Basin in Australia, was performed with Accelerator Mass Spectrometry (AMS) (Collon, Kutschera, Loosli, et al., 2000) before Atom Trap Trace Analysis took over (Sturchio et al., 2004).

^{85}Kr

^{85}Kr was detected in 1950 as one of the many fission products of ^{235}U and was first published by Zeldes et al. (1950). It beta-decays with a half-life of (10.76 ± 0.002) yr and a probability of 99.56 % to ^{85}Rb (Firestone et al., 1996) with a maximum energy of 687 keV and an average energy of 251 keV (Meyer et al., 1980). Although there is a cosmogenic contribution to the atmospheric ^{85}Kr inventory, the anthropogenic production is higher by a factor of 10^4 (Styra et al., 1991). As a fission product of ^{235}U and ^{239}Pu it is accumulated in the fuel rods of nuclear power plants and is released into the atmosphere in reprocessing facilities when the fuel rods are dissolved in nitric acrid (Von Hippel et al., 1985). This

leads to a modern isotopic abundance of about $2 \cdot 10^{-11}$. Almost all sources of anthropogenic ^{85}Kr are located in the northern hemisphere leading to an approximately 13 % lower ^{85}Kr activity on the southern hemisphere (chapter 5).

2.2.2. Tritium, CFCs, SF_6 and Halon-1301

Tritium, CFCs and SF_6 are tracers to date young water that was in contact with the atmosphere within the last 60 years. As pictured in Figure 2.7, their atmospheric concentration increased significantly in the 1950s either due to nuclear bomb tests (as for ^{3}H, ^{36}Cl and ^{14}C) or through industrial production. The trend of the atmospheric input functions of the discussed tracers is shown in Figure 2.7.

Tritium

The concentration of Tritium is usually expressed in tritium units (TU) which corresponds to one molecule of ^{3}H^{1}HO in 10^{18} molecules of ^1H_2O. The natural background of tritium varies seasonally and with latitude due to spacial and temporal variations in the interaction between the stratosphere and the troposphere, the so called "spring leak of the tropopause" (Hebert, 2011). Tritium has been measured in rainfall and on wine samples from before 1950s in different locations on the world. Allison et al. (1977) determined it to be between 1-3 TU in South Australia and Kaufman et al. (1954) report values around 3-6 TU in North America.

With the start of the nuclear bomb testing in 1952, the atmospheric concentration of tritium rose to values of about 5000 TU in the northern hemisphere, while average values on the southern hemisphere peaked around 40 TU. The huge concentration differences between the hemispheres is caused by the fact that basically all bomb tests were performed on the northern hemisphere and that most of the tritium mixed into the ocean and the biosphere within the interhemispheric exchange time. After the atmospheric test ban treaty in 1963, the atmospheric tritium concentration decreased rapidly mainly because of mixing into other reservoirs and due to radioactive decay.

It is hard to derive a tracer age when only the tritium concentration of a sample is known, as the atmospheric input function declined rapidly after the bomb-peak and because of seasonal variations, both leading to non-unique solutions. Multiple samples are required in order to trace the bomb-peak itself as a fix point to the year 1963. Tritium has a half-life of (12.32$\pm$0.02) yr (Lucas et al., 2000) and β^--decays to ^{3}He. This allows for the former described mother-daughter pair dating method as long as one can identify the tritiogenic ^{3}He component (He_{tri}):

$$^3He_{tri} = {}^3He_{tot} - {}^3He_{eq} - {}^3He_{ter} - {}^3He_{ex} \tag{2.16}$$

with $^3He_{tot}$: total amount of ^3He
$^3He_{eq}$: ^3He through equilibration with the atmosphere
$^3He_{ter}$: primordial ^3He from the Earth mantle
$^3He_{ex}$: excess air component of ^3He

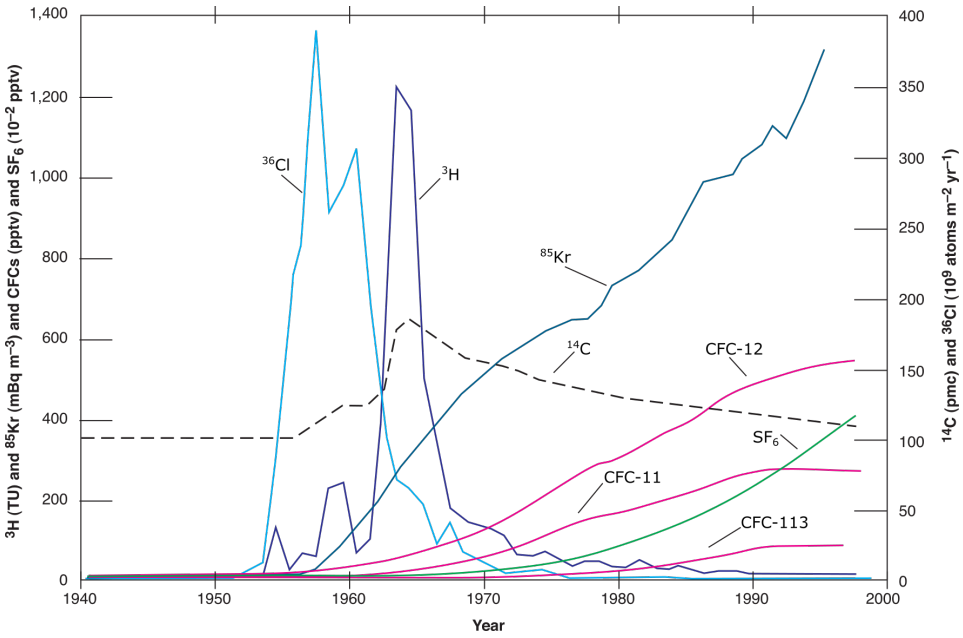

Figure 2.7.: Atmospheric concentrations between 1940 and 2000 of tracers for young waters and ^{14}C and ^{36}Cl. Clearly visible is the increase of tracer concentrations caused by nuclear bomb tests and the rise of industrially produced tracers since the 1950s (Alley et al., 2002).

CFCs

Chlorofluorocarbons (CFCs) are another example for anthropogenic tracers. They are synthetic compounds of carbon, chlorine and fluorine and were produced mainly for refrigeration since the early 1930s (Plummer et al., 2006).The major molecules for dating are CFC-11 ($CFCl_3$), CFC-12 (CF_2Cl_2) and CFC-113 ($C_2F_3Cl_3$). Their atmospheric concentration peaked around 2001 with 546 pptv (CFC-12), 262 pptv (CFC-11) and 82 pptv (CFC-113) respectively. The unit pptv stands for part per trillion by volume. Concentrations in water are usually given in pmol/kg and are converted to the corresponding atmospheric concentration, assuming equilibrium conditions, with Henry's law Equation 2.34 when knowing the infiltration parameters T, S and p. The inferred atmospheric concentration is then compared with the known (local) input function to derive the tracer age. As a result of the *Montreal Protocol to Reduce Substances that Deplete the Ozone Layer* in 1987, industry emissions decreased, the atmospheric input curves flattened and finally decreased for most CFCs, making the tracer less reliable for very young waters.

Despite the uncertainties related to the decreasing input function, other difficulties for dating with

CFCs are potential microbial degradation under anaerobic conditions in the subsurface, especially of CFC-11 (Bauer et al., 1996) and contamination related to inappropriate sampling equipment like silicone rubber tubes. Contamination and degradation usually affects CFC-11 and CFC-113 stronger than CFC-12 so an analysis of all three CFCs is advised to detect and possibly correct for these effects.

SF_6

Sulphur hexafluoride (SF_6) is mainly used as an electrical insulator and its industrial production commenced in 1953. Its atmospheric concentration increased rapidly from its natural background of about 0.05 ppt to ~5 ppt in the late 1990s (Plummer et al., 2006). SF_6 is considered one of the most potent greenhouse gases, about 4 orders of magnitude stronger than CO_2. This is why it was included in the *Kyoto Global Warming Protocol Agreement* from 1997, following which its production was cut back. It has not only been used as a dating tracer but also in tracer release experiments to mark water masses and investigate transport mechanisms of water masses either in the ocean or in aquifers. Underground production can become a problem especially in igneous rocks and carbonate aquifers, where samples can show concentrations exceeding the anthropogenic contribution (Busenberg et al., 2000). With a similar dating range as CFCs and tritium, it is especially valuable as a backup for altered tritium or CFC values through one of the above mentioned contamination or degradation effects.

Both, CFCs and SF_6 are analysed via gas chromatography and are routinely applied especially in oceanography. Although SF_6 concentrations are ~100 times lower than CFC concentrations and with that, less precise to measure. Tritium and especially the $^3H/^3He$ method requires more analytical effort. Tritium is either analyzed via decay counting, or with the ingrowth method on a mass spectrometer in which ^3He as a decay product of ^3H is measured two times with several weeks difference during which the ^3He is enriched and the initial tritium can be derived from the accumulation rate of ^3He in the sample.

Halon-1301

Bromotrifluoromethane (CF_3Br), which is commonly known as Halon-1301, was suggested as new dating tracer for groundwater analysis less than 4 years ago, by Beyer et al. (2014). It was first detected by Busenberg et al. (2008) during analysis of CFCs and SF_6 but was confused for CFC-13 at that time. Over the last 3 years, it has been applied in only a handful of studies, mostly by the group located in Wellington, New Zealand, that 'invented' the dating tool.

Halo-1301 is of purely anthropogenic origin and was used as refrigerant gas and fire suppressant agent from the 1970s on. Before that time, its atmospheric concentration was beneath the detection limits and thus, can be assumed zero. Similar to CFCs, it causes ozone depletion and therefore, its production was cut back as a consequence of the Montreal Protocol from 1987. It has a very similar

input function as SF_6 and almost the same age information is derived from it.

The benefits of applying this tracer lie in the different reliabilities depending on the hydrological system the samples are extracted from. Beyer et al. (2017) did a large scale groundwater study in New Zealand in which they analyzed more that 300 samples with Halon-1301, $SF-6$, tritium and CFCs (CFC-11, CFC-12 and CFC-113). For each tracer they found groundwater aquifer conditions in which no interpretation was possible due to various effects. Tritium having a non-unique function sometimes results in up to 3 possible tracer ages, SF_6 was sometimes enriched due to subsurface production, the CFCs were sometimes degraded or contaminated by adjacent industry and Halon-1301 concentrations were sometimes reduced as well, likely due to microbial degradation under anoxic conditions. The actual degradation processes of Halon-1301 in the subsurface are not yet sufficiently understood (Beyer et al., 2017)

An advantage of the tracer is, that Halon-1301 can be analyzed with only a minimum of extra effort, as it is measured together with SF_6 from the same sample.

2.2.3. ^{14}C

^{14}C dating in oceanography, groundwater hydrology or glaciology can become very complicated. For a deeper understanding, books like Plummer et al. (2013) are recommended. Here, a very general introduction to the tracer and its application in the different reservoirs ocean, groundwater and ice is given.

In 1946 Willard F. Libby discovered ^{14}C in atmospheric CO_2 and determined its half-life to 5568 years (Libby half-life). He and his group then dated for the first time organic carbon which revolutionized research in many fields. Libby was honored for his research, winning a noble prize for chemistry in 1960. Later measurements indicated that the Libby half-life was ~3 % too low and a half-life of (5730 $\pm$ 40) years was determined (Godwin, 1962). To not conflict with former studies, conventional carbon ages were still calculated using the Libby half-life and need corrections before comparing with calender years.

There are many different definitions, units and conventions in the business of radiocarbon dating. Without going into too much detail, the following short section will give a brief overview of the later used units.

Even if since 1977 more and more samples are analyzed with accelerator mass spectrometry (AMS), where isotopic ratios are measured directly, most definitions and conventions in radiocarbon dating originate from decay counting. The basic information here is the specific activity of a sample (A_S) and of a standard (A_{STD}), both corrected for the activity of a background sample, mostly given in counts per minute per g carbon (cpm/g C) or Bq/kg C.

The two questions that arise are: First, does it make a difference from what kind of sample the carbon

is extracted from and second, what are the properties of the standard.

The gram carbon, the activity measurement is related to, consists basically out of the three isotopes ^{12}C, ^{13}C and ^{14}C. The ratios of these three isoptopes can differ from a predefined standard through fractionation processes, like photosynthesis, or evaporation and condensation processes. A measure to account for this fractionation is δ^{13}C:

$$\delta^{13}C = \left(\frac{\left(^{13}C/^{12}C\right)_{\text{Sample}}}{\left(^{13}C/^{12}C\right)_{\text{Standard}}} - 1 \right) \cdot 1000\,‰ \tag{2.17}$$

Originally, the common standard used was Pee Dee Belemnite (PDB) which is a marine fossil with a high ^{13}C/^{12}C ratio resulting in typically negative δ^{13}C values for water and air samples. As the effect of fractionation for ^{14}C in a sample is proportional to that for ^{13}C, both, A_{S} and A_{STD} can be corrected to the same sample type, which is by convention wood, with a δ^{13}C of -25 ‰.

The specific activity of the standard the ^{14}C measurements are related to, can be expressed either as an absolute standard activity of A_{abs} = 226 Bq/kg C (the ^{14}C activity in wood in 1890) or it is corrected for fractionation and decay to the time the sample is measured (A_{STDcorr}). This leads to the expression of percent Modern Carbon (pMC), which was used for the few ^{14}C samples taken in the course of this thesis.

$$^{14}C = \frac{A_{\text{S}}}{A_{\text{STDcorr}}} \cdot 100\,\% \qquad\qquad [\text{pMC}] \tag{2.18}$$

So a ^{14}C concentration of 50 pMC corresponds to the time one half-life ago, i.e. 5730 years before present (BP).

^{14}C is produced naturally in the upper atmosphere via cosmic ray induced neutron capture of nitrogen corresponding to the ^{14}N(n,p)^{14}C reaction. It then quickly oxidizes to $^{14}CO_2$ and is partly incorporated into the biosphere as organic carbon by photosynthesis of plants. Once the organism dies, or $^{14}CO_2$ infiltrates as inorganic carbon into the ocean, groundwater or ice, the radiogenic clock starts ticking and the ^{14}C concentration decreases through β^--decay.

The carbon that is dated can be present in different forms. It can be inorganic or organic carbon and either dissolved or present as larger particles. For dating groundwater or seawater, it is mainly sampled for dissolved inorganic carbon (DIC) which is the atmospheric CO_2 reacting with the water to bicarbonates.

In most cases it is not possible to derive an age of a sample directly from the measured ^{14}C concentration, as there are many effects influencing it. As stated above, for decay counting the ^{14}C content is derived from the activity per gram carbon, which means the ratio between ^{14}C and the two stable carbon isotopes ^{12}C and ^{13}C is indirectly measured. These ratios are usually altered by different effects:

The atmospheric $^{14}C/^{12}C$ ratio has not been constant over the last 50.000 thousand years as seen in measurements on tree rings and other carbonate archives (Reimer et al., 2009). A varying magnetic field of the Earth and a varying solar activity cause oscillations in the cosmic ray intensity, thus leading to fluctuations in the ^{14}C production rate. Moreover, two anthropogenic effects changed the $^{14}C/^{12}C$ ratio in the last centuries. First, the Suess-Effect, describing the dilution of ^{14}C in the atmosphere by burned radiocarbon free fossil fuels (Suess, 1955), and secondly the bomb-peak in the 1960s resulting from nuclear bomb tests. A well known atmospheric input curve is needed to account for these variations.

Another effect is the already described isotopic fractionation. During photosynthesis the uptake of lighter carbon dioxide isotopologues is preferred leading to a decrease of the $^{13}C/^{12}C$ and $^{14}C/^{12}C$ ratio. Another fractionation occurs when CO_2 is dissolved in water with a higher solubility for heavier isotopologues.

A discrepancy between 'true' and apparent ages derived from radiocarbon concentrations is often caused by so called reservoir effects. This means that another carbon reservoir than the atmosphere, one that is often depleted in ^{14}C, influences the measured ^{14}C activity. In groundwater the ^{14}C might be diluted by old, ^{14}C depleted carbon from calcium carbonate rocks. Shells from a marine environment seem on average 400 years older than terrestrial samples. On the one hand, because the transformation from dissolved atmospheric CO_2 to bicarbonates, which the shells are made of, takes time. On the other hand, due to upwelling transporting older, ^{14}C depleted waters to lower depth.

The last factor influencing ^{14}C dating is the sampling itself. Atmospheric contamination should be avoided as far as possible and the sterilization to prevent biological activity is often necessary, which as well enhances the risk of contamination.

2.3. Transit time distributions

All the introduced tracers are applied in hydrology in order to gain insight into the dynamics of a specific system. The time for transporting water from the surface or recharge area to the interior of a fluid system is a fundamental description of the flow. This 'transit time', is never one distinct time, but rather a distribution, as the different water molecules took different path ways to the investigated water parcel. Hence, the composition of the entire temporal flow history within a water parcel can be described as an age distribution or, as it will be called in the following, the transit time distribution (TTD) of a (sampled) water volume.

Surface water and freshly formed groundwater contain a signature of the atmospheric concentrations of the age tracers, which are transported along with the water to the interior of the water reservoir. From a mathematical perspective, the TTD is a type of Green function that propagates the initial tracer concentrations c_0(t) into the interior of the reservoir (Waugh et al., 2003). The resulting time series of the tracer concentration $c(\vec{r}, t)$ at position $\vec{r}$ in the interior with the transit time distribution $G(\vec{r}, t)$ is

given by:

$$c(\vec{r},t) = \int_0^\infty c_0(t-t') \cdot e^{-\lambda t'} \cdot G(\vec{r},t')dt' \tag{2.19}$$

with t : present time
t' : time span before t
λ : decay constant of a radioactive tracer

The measured tracer concentration at time t in location $\vec{r}$ is given by the convolution of the atmospheric input function c_0 of the tracer in the formation area and the TTD $G(\vec{r},t)$ of the sample (Hall et al., 1994). In case of a radioactive tracer, the output concentration has to be decay corrected.

As a probability function, the shape of the TTD can be examined by analyzing its moments. The k-th raw moment is defined as:

$$m_\mathrm{k} = E[X^\mathrm{k}] = \int_0^\infty x^\mathrm{k} G(x)\, dx \tag{2.20}$$

with $E[X]$: statistical mean of random variable X

The first raw moment gives the mean of the distribution, which will be called Γ. For moments of higher order, it makes sense to investigate the distribution around this mean:

$$\mu_\mathrm{k} = E[(X - E[X])^\mathrm{k}] = \int_0^\infty (x - E[X])^\mathrm{k} G(x)\, dx \tag{2.21}$$

with the second central moment μ_2 being the variance or width of the distribution which will be called Δ. The higher moments further quantify the shape, with the third central moment being the skewness and the fourth the kurtosis.

The TTDs that are usually applied for analysis are already fully determined by their first moment, the mean age, or by the first two moments, mean and width of the distribution function.

When the initial tracer history c_0(t-t') is known and $c(\vec{r}$, t) is measured, then the central moments of an assumed TTD can be constrained. This is usually done with so called lumped parameter models, which are simple one dimensional models treating the hydrological system as one box between recharge and discharge. They determine the mean age and the width of a pre-assumed TTD by tuning them to best describe the measured tracer concentrations. In Figure 2.8 this principle is illustrated.

In the following, the TTDs that are worked with in the course of this thesis are presented.

Different assumptions can be made when investigating the history of a water body. The simplest is, to neglect any kind of mixing processes. All water in the sample formed at the same time and traveled isolated from its environment through the ocean or aquifer. This view corresponds to the Piston Flow model, expressed by a delta distribution.

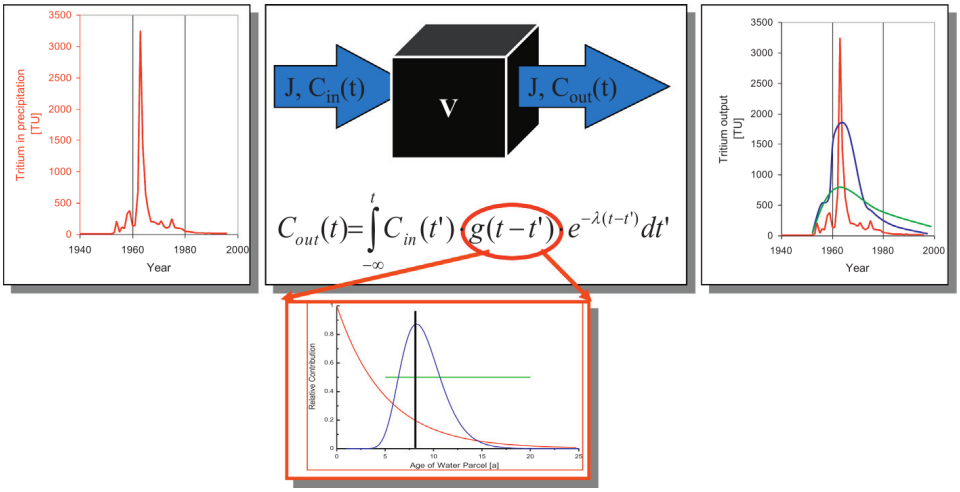

Figure 2.8.: The principle of a lumped parameter model is illustrated using tritium as an example. The known input curve is convoluted with an assumed TTD resulting in the modeled tritium concentrations for a water body described by the TTD (Suckow, 2014b).

$$G(t') = \delta(t' - \Gamma) \tag{2.22}$$

This model is usually not very realistic. Even if an aquifer has a well defined recharge area, dispersion widens the distribution and mixing with younger or older water often occurs.

A model more suitable for ocean surface waters, lakes or shallower aquifers is the exponential model. In Figure 2.9 the idea behind the model is illustrated. Assuming an unconfined aquifer with homogenous recharge R and porosity Θ over the entire area and with a well drilled to the very bottom of the aquifer. When the well is screened over the entire thickness of the aquifer, then the age distribution of the extracted water is described as:

$$G(t') = \frac{1}{\Gamma} e^{-\frac{t}{\Gamma}} \tag{2.23}$$

The underlying assumption here is, that the age of the water at the very bottom of the well tends towards infinity. An aquifer that is well described by all these properties is often called a Vogel-aquifer after Vogel (1968), who first used this model.

In many cases the screen of a well covers only a particular depth region. This scenario is described by the so called *Partial Exponential Model*. As it is the best description of the aquifer studied in chapter 4, the corresponding TTD will be derived in the following, after Jurgens et al. (2012).

The age to depth relation within an Vogel-aquifer is given by:

$$T(z) = \frac{L\Theta}{R} \ln\left(\frac{L - z}{L}\right) \tag{2.24}$$

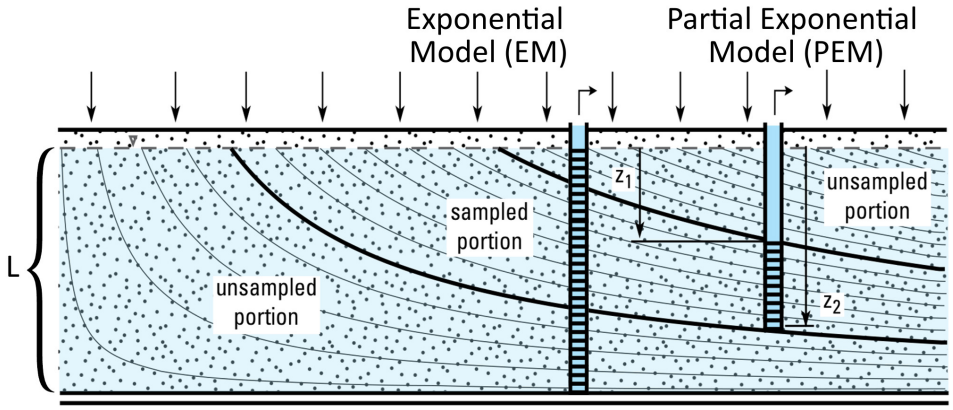

Figure 2.9.: Illustration of when the exponential model and the partial exponential model can be applied (Jurgens et al., 2012).

with L beeing the thickness of the aquifer and z the depth beneath the groundwater surface. The expression

$$\tau_{\text{aq}} = \frac{L\Theta}{R} \tag{2.25}$$

is the mean age of the entire aquifer, as it is the aquifer volume divided by the recharge, just one dimensional. The mean age of the water column within the screen (s), ranging from z_1 to z_2, is obtained by integrating the ages over these depths:

$$\tau_{\text{s}} = -\frac{1}{z_2 - z_1} \int_{z_1}^{z_2} \frac{L\Theta}{R} \ln\left(\frac{L-z}{L}\right) \mathrm{d}z \tag{2.26}$$

The general solution of Equation 2.26 is:

$$\tau_{\text{s}} = \frac{H}{z_2 - z_1} \frac{L\Theta}{R} \frac{L-z_2}{L} \ln\left(\frac{L-z_2}{L}\right) - \frac{L-z_2}{L} - \frac{L-z_1}{L} \ln\left(\frac{L-z_1}{L}\right) + \frac{L-z_1}{L} \tag{2.27}$$

Substituting now:

$$n_1 = \frac{L}{L-z_1} \quad \text{and} \quad n_2 = \frac{L}{L-z_2} \tag{2.28}$$

and applying Equation 2.25 leads finally to:

$$\tau_{\text{s}} = \left(\frac{1}{\frac{1}{n_1} - \frac{1}{n_2}}\right) \tau_{\text{aq}} \left(\frac{1}{n_1} \ln(n_1) + \frac{1}{n_1} - \frac{1}{n_2} \ln(n_2) - \frac{1}{n_2}\right) \tag{2.29}$$

This equation relates now the mean age of the entire aquifer, to the mean age of the water sampled from the screen. While the exponential model has only τ_{aq} as free parameter, the PEM has the three

additional variables L, z_1 an z_2. In most groundwater studies, the screen depth is usually known. Often the same applies for the thickness L, if not, then the parameter must be constrained by another tracer or has to be estimated.

The age distribution $G(t)$ of the PEM is that of the EM within the times related to the screen depth via Equation 2.25 normalized to 1 (see Figure 2.10):

$$G(t) = \left(\frac{1}{\frac{1}{n_1} - \frac{1}{n_2}}\right) \frac{1}{\tau_{\text{aq}}} \exp\left(\frac{-t}{\tau_{\text{aq}}}\right); \quad for \quad t_1 \leq t \leq t_2 \tag{2.30}$$

$$\text{with} \quad \begin{aligned} t_1 &= \tau_{\text{aq}} \ln(n_1) \\ t_2 &= \tau_{\text{aq}} \ln(n_2) \end{aligned}$$

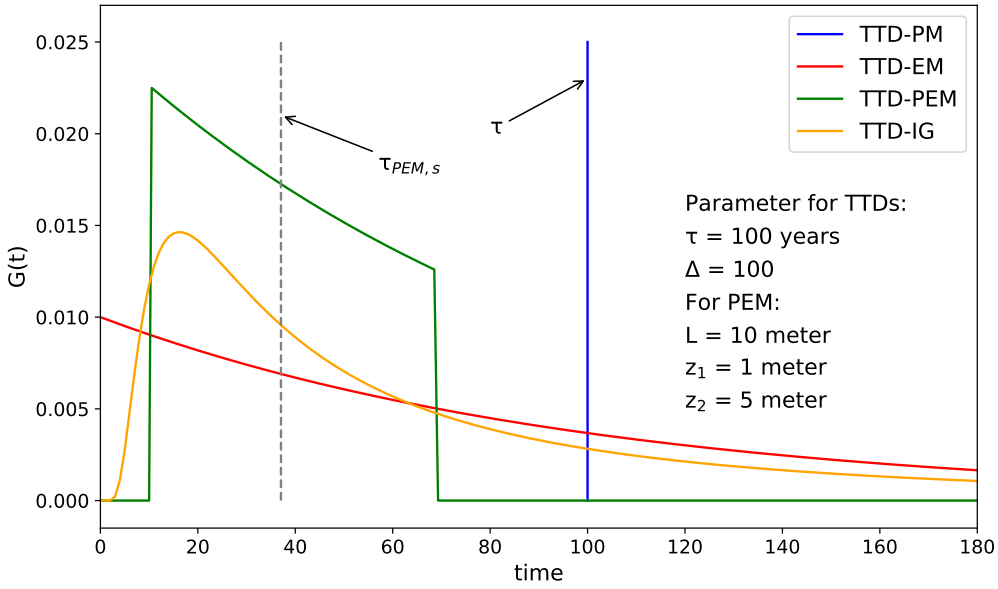

Figure 2.10.: The four TTDs that are applied in the course of this thesis are plotted. All with the same mean age of $\tau = 100$ yr.

A TTD that is often applied in oceanography is an inverse Gaussian distribution (Waugh et al., 2003; Stöven et al., 2014):

$$G(t') = \sqrt{\frac{\Gamma^3}{4\pi\Delta^2 t'^3}} \exp\left(\frac{-\Gamma(t'-\Gamma)^2}{4\Delta^2 t'}\right) \tag{2.31}$$

$$\begin{aligned} \text{with} \quad \Gamma &: \quad \text{mean residence time} \\ \Delta &: \quad \text{width of distribution} \end{aligned}$$

Here, two tracers working at very different time scale, while still having a significant overlap, need to be applied in order to constrain the two moments of the distribution. The ratio Δ/Γ can be understood as the proportionality between the advective and diffusive flow, which is the definition of the Péclet number. For $\Gamma >> \Delta$ the flow can be assumed purely advective and the distribution tends to a narrow Gaussian distribution around Γ.

Further considerations concerning lumped parameter models and transient time distributions are postponed to chapter 6 and chapter 4 when these tools are actually applied.

2.4. Gas exchange

Almost all tracer methods applied in the context of this thesis are based on gaseous tracers dissolved in water. Therefore this section gives a brief summary of exchange processes between a liquid and a gaseous phase.

The ratio between the concentration c of a substance in gas phase (G) and water phase (W) in equilibrium is given by the so called *Henry constant*:

$$H'(T,S) = \frac{c^{\mathrm{G}}}{c^{\mathrm{W}}} \tag{2.32}$$

H' is the dimensionless Henry constant, assuming the concentrations have the same units, which is typically the volumetric unit mol/L. With the ideal gas law,

$$c^{\mathrm{G}} = \frac{n_{\mathrm{i}}}{V} = \frac{p}{RT} \tag{2.33}$$

with
n : number of moles of the gas
V : volume of the gas phase
p : partial pressure of the gas
R : universal gas constant 8.3144 J mol^{-1} K^{-1}

c^G can be related to the partial pressure p of a substance:

$$p = H(T,S) \cdot c^{\mathrm{W}} \tag{2.34}$$

This is Henry's law in its most common form with the Henry-Coefficient $H = RTH'$ in [atm L mol^{-1}]. It says, that the concentration of a substance in the liquid phase increases linearly with the partial pressure of that substance in the gas phase above the liquid. The proportionality factor H depends on the salinity and the temperature of the liquid.

In literature the solubility λ of a substance is often given, which is the inverse of the Henry coefficient H, while the dimensionless solubility constant L is the inverse of the Henry constant H', which is

called the Ostwald solubility. Figure 2.11 illustrates the decreasing Ostwald solubility for gases with increasing temperature.

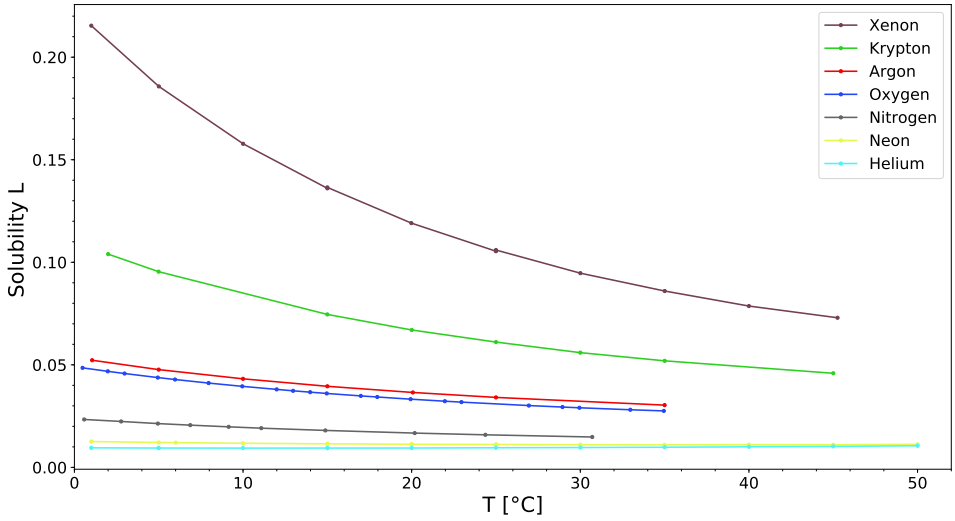

Figure 2.11.: The Ostwald solubility L in [(mol/L)/(mol/L)] for the noble gases, nitrogen and oxygen, plotted against the temperature, for $S = 0$. The values are calculated from Benson et al. (1976).

To compare the decreasing solubility with increasing salinity, the Ostwald solubility for different temperature ranges and $S = 0\,‰$ and $S = 35\,‰$ are listed in Table 2.2.

Table 2.2.: The ostwald solubility L in $10^3 \cdot$[(mol/L)/(mol/L)] of nitrogen, oxygen and argon in relation to the temperature for fresh water and for seawater, calculated after Weiss (1970).

S [‰]	0	35	0	35	0	35
T [°C]	N_2		O_2		Ar	
0	23.74	18.29	49.07	38.64	53.62	42.11
2	22.73	17.58	46.82	36.98	51.20	40.36
5	21.38	16.64	43.78	34.77	47.94	37.98
10	19.50	15.32	39.53	31.66	43.37	34.66
15	17.97	14.25	36.10	29.14	39.65	31.96
20	16.74	13.38	33.31	27.09	36.62	29.75
25	15.74	12.68	31.04	25.43	34.13	27.95

2.5. Sorption of gases on surfaces

A major task in the course of this thesis was the design and application of sample purification setups for argon and krypton. This means, that from an initial gas mixture of variable composition, the argon

or krypton fraction has to be separated from all reactive gases. This is done by exploiting different properties of so called sorbents. In particular, activated charcoal, Li-LSX zeolite and getter materials, mainly titanium sponge.

As the used terms are all very similar, a clear definition is important to prevent confusion. *Sorption* is the overall term for the physical or chemical process of one substance getting attached to another. In the context of this thesis, only sorption of gases on surfaces is of relevance. The gas that gets sorbed is called the *sorbate*, while the substance the sorbate is attached to is called *sorbent*. The process of sorption can now further be divided into a physical sorption of the sorbate onto the surface, which is called *adsorption* or sometimes *physisorption*, while the incorporation of the sorbate into the sorbent is called *absorption* or mostly *chemisorption*, to not rely on the one letter difference.

In the following, the two main processes, physisorption on activated charcoal and zeolite, and the chemisorption on getter material will be discussed. To not get lost in the deeper theory of thermodynamics, the introduction will be kept short and only focused on the background required for the application of the sorbents. The section mostly follows Yang (2003) and Keller et al. (2005) as well as Smíšek et al. (1970).

2.5.1. Physisorption on activated charcoal and zeolite

Two slightly different approaches to the theoretical description of adsorption will be made. First, by focusing on the interaction between adsorbent and adsorbate and secondly, by thermodynamic considerations.

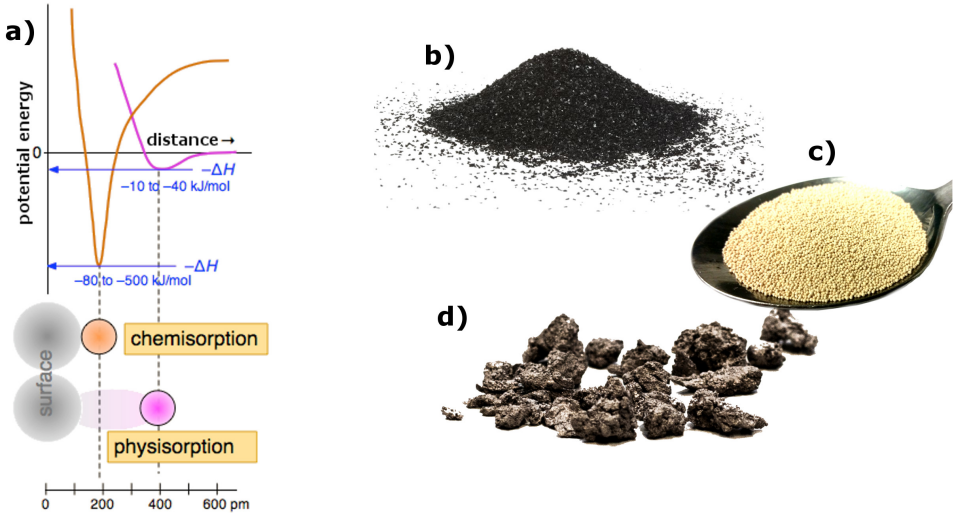

Figure 2.12.: In a) the two different sorption potentials for physisorption and chemisorption is illustrated, taken from Lower (2017) b-d) are pictures of the three sorbents used in the course of this thesis, activated charcoal, Li-LSX zeolite and titanium sponge.

Adsorbent-adsorbate interaction

Gas in the presence of an adsorbent is either in the adsorbed or desorbed state. Considering the vapor pressure p_0 of the adsorbed state, the energetically preferred state the gas molecules strive for can be described in first approximation with regard to the Gibbs-Energy for an ideal gas:

$$-\Phi = -\Delta G = RT \ln \frac{p_0}{p} \tag{2.35}$$

with
Φ : interaction potential energy
ΔG: change of Gibbs-Energy
p : pressure within the adsorbed gas state
R : universal gas constant 8.3144 J mol^{-1} K^{-1}

That means, as long as $p < p_0$, ΔG and with that Φ are negative and the gas molecules strive to the adsorbed state, hence, adsorption occurs. Moreover, the more negative the interaction potential Φ, the higher the saturation vapor pressure of the adsorbate, so the higher the fraction of adsorbed gas molecules.

For further considerations, the interaction between the adsorbed gas molecules on the surface will be ignored and the focus is on the adsorbent-adsorbate interaction. In Figure 2.12 a), the interaction potential for physisorption is shown which reflects the Van-der-Waals force between surface and gas molecules. The single contributions are:

$$\Phi = \underbrace{\Phi_{\mathrm{D}} + \Phi_{\mathrm{R}}}_{\text{activated charcoal}} + \underbrace{\Phi_{\mathrm{Ind}} + \Phi_{\mathrm{F}\mu} + \Phi_{\dot{\mathrm{F}}\mathrm{Q}}}_{\text{zeolite}} \tag{2.36}$$

with
Φ_{D} : dispersion energy
Φ_{R} : repulsion energy
Φ_{Ind} : interaction electric field (F) and induced dipole
$\Phi_{\mathrm{F}\mu}$: interaction between F and permanent dipole (μ)
$\Phi_{\dot{\mathrm{F}}\mathrm{Q}}$: interaction electric field gradient $\dot{F}$ quadrupole moment (Q)

The dispersion, or more accurate London-Dispersion, is the attraction force between non-polar molecules and atoms which occurs through spontaneous polarization and is not specific for a certain sorbent. Neither is the close-range repulsion term which results from the Pauli exclusion principle. The last three terms require charges on the surface of the adsorbent. For conventional adsorbents this is only the case for zeolite, which makes it an efficient material for separating gas species with permanent dipole or quadrupole moment from those without or strongly differing one. The interaction potential for gas species with activated charcoal mainly depends on the dispersion term, i.e. on the polarizability of the interacting materials.

For qualitative considerations, evaluating the interaction potential between different adsorbents and adsorbates is already helpful in choosing the right group of adsorbents for gas separation. For quantitative calculations, a different approach is taken by evaluating so called *adsorption isotherms* and calculating the isosteric heat ΔH.

Adsorption isotherms and isosteric heat

In many aspects, adsorption of gas to surfaces can be described as a phase transition similar from gas to liquid. Physisorption is reversible and represents a thermodynamic equilibrium between gas phase and adsorbed phase, depending on the temperature, the pressure of the gas phase and the specific properties of adsorbent and adsorbate. Adsorption can thus be described, in analogy to a two phase system in thermodynamic equilibrium, with the Clausius-Clapeyron equation. The equation can be approximated for low pressures and low temperatures to:

$$\left(\frac{\partial \ln(p)}{\partial T}\right)_{\mathrm{a}} = \frac{\Delta H}{R \cdot T^2} \overset{integration}{\rightarrow} \ln(p) = -\frac{\Delta H}{RT} + c \tag{2.37}$$

with
p : pressure
ΔH : isosteric heat
R : universal gas constant 8.3144 J mol^{-1} K^{-1}
a : equilibrium amount of adsorbed gas
c : constant

The isosteric heat, which is the change of enthalpy, can be understood as the heat of condensation. So the heat that is released when molecules get attached to a surface. It is the key measure for the strength of the interaction between adsorbent and adsorbate as well as an indicator to distinguish physisorption from chemisorption. For low amounts of adsorbed gas it can be related to the interaction potential by (Yang, 2003):

$$\Delta H = \Phi - RT + F(T) \tag{2.38}$$

with $F(T)$ standing for the vibrational and translational energies of the adsorbed molecule. The isosteric heat released during physisorption is in the order of 10 - 40 kJ/mol while for chemisorption it is typically between 80 - 500 kJ/mol (Figure 2.12a).

Another important property of an adsorbent is its adsorption capacity. The equilibrium amount a of gas adsorbed is a function of the pressure of the gas above the adsorbent p and the temperature T. To study the relation of two of these quantities while keeping the third constant is a revealing method to study the properties of adsorbent - adsorbate interactions:

$$
\begin{aligned}
I) \quad & a = f(p) \ \text{ with } \ T = \text{const.} \\
II) \quad & a = g(T) \ \text{ with } \ p = \text{const.} \\
III) \quad & p = h(T) \ \text{ with } \ a = \text{const.}
\end{aligned}
\tag{2.39}
$$

I) is called *adsorption isotherm*, describing the amount of gas adsorbed in equilibrium with varying gas pressure for a specific constant temperature. Adsorption isotherms can be subdivided into groups with characteristic trends, representing sets of similar properties of an adsorbent - adsorbate interaction, if the adsorbed gas builds a mono layer on the surface, or if the adsorption potential is homogeneously on the entire adsorbents surface and so forth.

A good description of the shape of adsorption isotherms of zeolites is given by the so called Langmuir equation (Langmuir, 1918). The equation itself will not be derived here as it is done in any literature concerning adsorption, especially on zeolites. In Figure 2.13 three adsorption isotherms for nitrogen, oxygen and argon at 25 °C are displayed, measured on the same type of zeolite that is used for argon and krypton separation in the context of this thesis.

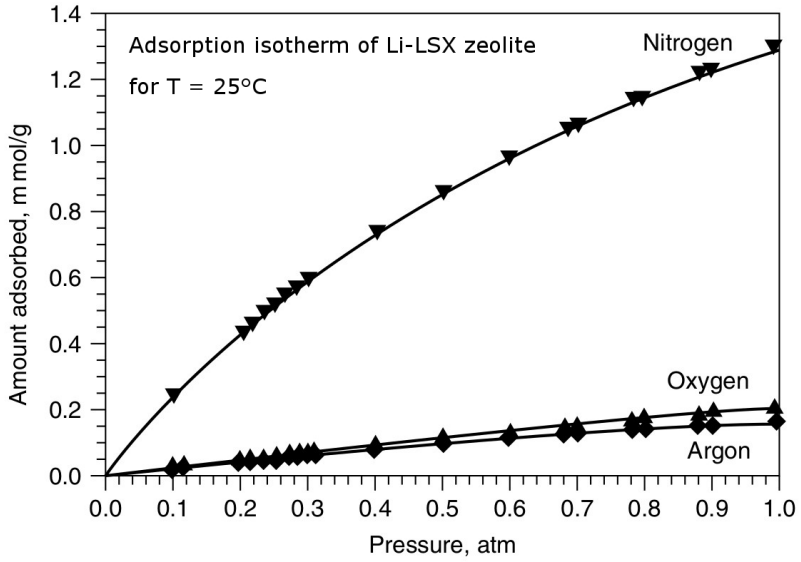

Figure 2.13.: Adsorption isotherms on zeolite Li-LSX for N_2, O_2 and Ar at 25 °C. The pressure of the desorbed gas species above the adsorbent is plotted against the adsorbed amount of gas on the adsorbent (Yang, 2003).

Adsorption isotherms for specific sorbents are typically obtained by a semi-empirical approach. For a fixed temperature known amounts of a gas species are introduced into a vacuum chamber with known volume containing the sorbent. Via pressure measurements the amount of adsorbed gas is calculated and plotted against the equilibrium pressure. This is done for a set of different pressures at different

temperatures and these data points are fitted with a theoretical isotherm after the Langmuir or other approaches, that describes the measured data best. With that, the adsorption isotherms extrapolate in pressure ranges that have not been measured. By knowing the behavior of a in relation to p for different T, the isosteric heat can be calculated from Equation 2.37.

Activated charcoal

Activated charcoal (AC) is used for many different applications in the context of this thesis: As a storage for gas, as a pump to transfer gas from one volume to another, as filter, to retain a specific gas species and as adsorbent for gas chromatography. It is pictured in Figure 2.12b. AC has the largest surface amongst all sorbents, with a specific surface area of up to $1000\,\mathrm{m^2/g}$. Such a large specific surface requires an extremely high porosity which is obtained through the carbonization and the following activation process of carbonaceous materials. Those materials are mostly of vegetable origin like wood, coal, fruit stones or shells. The carbonization is done by thermal decomposition of the material in an inert atmosphere or under vacuum conditions at moderate temperatures. For the activation process, the material is heated up to 1100 °C while either adding chemicals, or gases like carbon dioxide for the carbon to react on. (Smíšek et al., 1970)

When investigating the interaction between activated charcoal and gas molecules, the London Dispersion Force (Equation 2.36), which is the weak part of the Van-der-Waals force, is the important term to look at, as AC itself is non polar.

$$\Phi_\mathrm{D} \approx -\frac{3}{2} \cdot \frac{I_1 I_2}{I_1 + I_2} \cdot \frac{\alpha_1 \alpha_2}{r^6} \tag{2.40}$$

with $\mathrm{I_i}$: ionization energy of molecule i
α_i : polarizability of molecule i
r : distance between molecules

The relevant parameter in this equation is the polarizability as the potential for molecules to built instantaneous dipoles. In relation to the position in the periodic table, the polarizability increases with each new electron shell, and with less electrons on the outer shell as it allows for an easier charge displacement. In Table 2.3, the polarizability of gases treated in the context of this thesis are listed in atomic units.

Table 2.3.: Averaged polarizability of the molecules present in a gas mixture processed with sorbents in the course of this thesis. Values after Schwerdtfeger (2015)

	H_2	He	N_2	O_2	Ar	Kr	Xe	CH_4	CO_2
α [$e^2a_0^2/E_h$]	4.5	1.4	7.4	6	11.1	16.8	27	16.9	19

In Figure 2.14, desorption curves for argon on a stainless steel trap and on a activated charcoal trap are pictured. The graph shows the adsorption isostere which correspond to formula II) in Equation 2.39. AC is used typically at three different temperatures for the purification setups worked with in this thesis: AC at liquid nitrogen temperature of 77K, at room temperature, so 300 K and at 376 K. As seen for the adsorption isostere at 77 K, basically all argon is adsorbed while at 376 K it can be considered as fully desorbed.

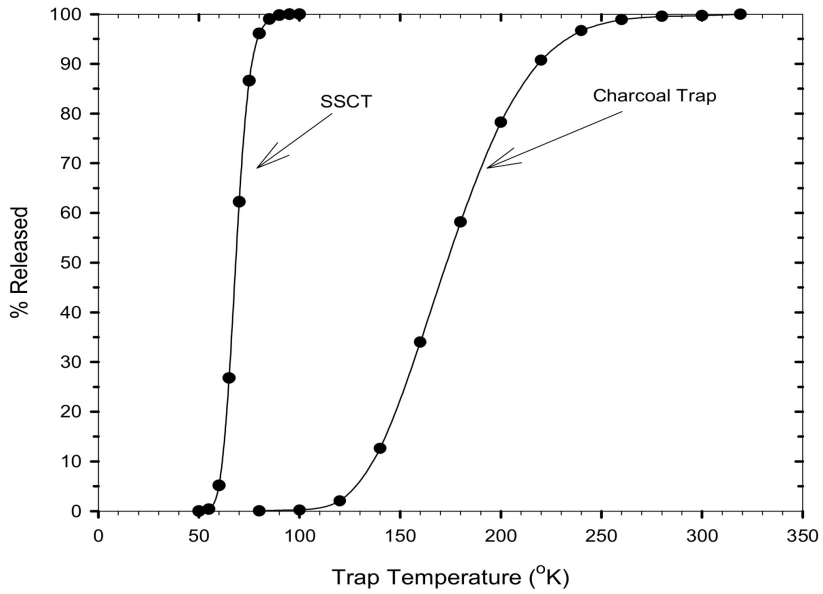

Figure 2.14.: Adsorption isosteres of argon on a stainless steel trap (SSCT) and on activated charcoal, according to Lott (2001).

Zeolite Li-LSX

The zeolite used for gas chromatography in this thesis is Li-LSX. It is pictured in Figure 2.12c). Zeolites in general are micro-porous aluminosilicate minerals that occur naturally as a reaction product of volcanic rocks or ashes with alkaline groundwater. They are as well produced industrially on a large scale as they are widely used in the industry as adsorbent and catalysts.

Their primary structure are the tetrahedra of silicon and aluminium, SiO_4 and AlO_4. They form secondary units as cubes, hexagonal prisms and octahedra which are then finally incorporated in a 3 dimensional crystalline framework. So far, more than 200 different structures have been synthetically produced by different arrangement of the aluminum and silicon tetrahedra. They are categorized into A, X and Y types according to their Si to Al ratio which is between 1 and 1.5 for the X-type. The ground structure is altered by extra framework cations, typically alkali metal cations which balance the -1 electric net charge of the AlO_2 molecule. The adsorption properties of the specific zeolite type

depends strongly on the type and amount of these extra alkali metal cations. The applied zeolite Li-LSX is a low-silica Type X (LSX) zeolite with lithium as extra framework cations.

A more detailed description of the chemical and crystalline structure of this and other types of zeolite is found in Yang (2003). The lithium cations on the zeolite surface cause an electric field that induces dipoles or interacts with existing permanent dipoles and quadrupole moments of adsorbates which then dominate the interaction potential explicated in Equation 2.36.

$$\begin{aligned} \Phi_{\text{Ind}} &= -\frac{1}{2}\alpha F^2 \\ \Phi_{\text{F}\mu} &= -F\,\mu\,cos\Theta \\ \Phi_{\text{Ind}} &= -\frac{1}{2}Q\,\dot{F} \end{aligned} \tag{2.41}$$

with F : electric Field
α : polarizability
μ : permanent dipole
Θ : angle between electric field and axis of the dipole
Q : quadrupole moment

None of the molecules listed in Table 2.3 has a permanent dipole and the induced dipole interaction again depends on the polarizability α of the adsorbate for the same adsorbent. An important factor causing differences in the total adsorbate-adsorbent interaction potential between the zeolite Li-LSX and the listed gas molecules is the quadrupole moment Q. Values for quadrupole moments of single isotopes vary in literature (Stone, 2005; Yang, 2003). On a qualitative level while for argon, krypton and methane the quadrupole moment is basically zero, CO_2 has a very high quadrupole moment of -4.3·10^{26} $\text{erg}^{1/2}\,\text{cm}^{5/2}$ followed by nitrogen with -1.5·10^{26} $\text{erg}^{1/2}\,\text{cm}^{5/2}$ and oxygen with -0.5·10^{26} $\text{erg}^{1/2}\,\text{cm}^{5/2}$.

Summing up these effects for the interaction potential between Li-LSX and the relevant gas components that are separated by the zeolite leads to:

$$\Phi_{\text{He}} << \Phi_{\text{Ar}} < \Phi_{\text{O}_2} < \Phi_{\text{Kr}} < \Phi_{\text{CH}_4} < \Phi_{\text{N}_2} < \Phi_{\text{CO}_2} \tag{2.42}$$

Adsorption chromatography

In adsorption chromatography, differences in the interaction potential between one adsorbent with different gas species are exploited to separate different gas species from each other, typically along a column. As stated in Equation 2.38, the interaction potential $\Phi \sim \Delta H$ (the isosteric heat) which again, according to the Clausius-Clayperon equation (Equation 2.37) is a measure for the ratio of gas molecules

in the adsorbed state to those in the desorbed state. The equilibrium between adsorbed and desorbed gases is a dynamic equilibrium, meaning the number of molecules leaving the surface is equal to the number of newly adsorbed ones, while the total number of molecules in the gaseous and adsorbed state remains constant.

The principle of adsorption chromatography is now, that all gases in the desorbed state get transported along a column filled with an adsorbent by a carrier gas, which is usually not adsorbed at all. The gas species which is less strongly adsorbed and thus, has a larger fraction of molecules in the desorbed state, is flushed faster through the column as a stronger adsorbed gas species.

The quality of a separation depends on several factors:

1. The adsorbent in the column must provide enough adsorption sites on its surface for the desorbed gases to adsorb again. Hence, a certain sorbate to sorbent ratio must not be exceeded.

2. The column must be long enough to guarantee a clean separation of the gas species.

3. A significant difference in the ratio of adsorbed to desorbed molecules for the different gas species must be given. Usually by optimizing the interaction potential difference of two gas species by regulating the temperature of adsorbate and adsorbent.

4. The flow of the carrier gas through the column must be in the right range. If the flow is too low, the ratio of advection to dispersion of the gas peaks traveling through the column is too high for a clean separation. If the flow is too high, adsorption sites are skipped and the separation is worsened.

Once the appropriate adsorbent for separating a gas mixture is found, the relevant parameter temperature, carrier gas flow, column dimensions and gas load onto the column must be optimized.

2.5.2. Chemisorption on getter material

In contrast to physisorption, the bonding between sorbent and sorbate (the isosteric heat) in chemisorption is much higher, usually by a factor of 10. In Figure 2.12a), the interaction potential for chemisorption is represented by the orange curve. While the potential for physisorption is usually always attractive up to a certain distance to the surface molecules (the so called Van-der-Waals radius), chemisorption often requires an activation energy to come close enough for the bonding. While in the process of physisorption, the participating molecules stay intact, in chemisorption the adsorbed gas molecule chemically reacts with the surface. The process of chemisorption is irreversible and once the sorption capacity of the sorbent is reached, it must be either replaced or often further heated, to allow the absorbed molecules to migrate in the interior of the sorbent.

Sorbents used for removing gas species via chemisorption are called getters or getter pumps, referring to their application in vacuum setups. A wide range of getter materials and getter pumps are commercially available. In the course of this thesis, titanium sponge and and a commercial getter pump based on alloy of different getter materials are used.

In Figure 2.12c), chunks of titanium sponge that are used as getter material are pictured. Titanium sponge is an excellent choice for removing reactive gases from a mixture due to its large absorption capacity, a high absorption speed and a low price. The only disadvantage is the high temperature that is required to start the gettering process. In his master thesis Schwefel (2011) investigated the absorption properties of titanium sponge for oxygen and nitrogen for different temperatures. According to his tests, oxygen requires temperatures of at least 400 °C and nitrogen 650 °C for any absorption to occur. The sorption speed increases significantly with the temperature and is in the order of 140 μL min^{-1} g$_{\mathrm{Ti}}^{-1}$ of oxygen and 70 μL min^{-1} g$_{\mathrm{Ti}}^{-1}$ at 800 °C with an average sorption capacity of ~60 mL gas per g titanium sponge.

According to Stout et al. (1955) the absorption properties for carbon dioxide are similar to those of nitrogen, while methane is absorbed already at temperatures below 600 °C. Hydrogen however shows a very different behavior. Here, titanium sponge works as adsorbent to which H_2 is attached for temperatures below 400 °C. This effect is important to keep in mind when gettering water vapor or methane, as the bonds of the molecules break for elevated temperatures and the oxygen and carbon are absorbed while the residual H_2 accumulates as desorbed gas in the getter until the temperature decreases below 400 °C again. Once the surface of the titanium sponge is saturated, it turns yellow brownish and must be replaced.

The other type of getter used in the context of this thesis is the *CapaciTorr HV200* from the *SAES group*. This commercial getter uses an alloy of titanium, zirconium, valadium and aluminum in form of highly porous sintered disks that are arranged to a replaceable cartridge in a stainless steel housing (Group, 2018). Before application, the getter must be activated at temperatures of ~550 °C under high vacuum conditions to clean the surface of the getter material. It is operated at moderate temperatures of ~200 °C and has excellent absorption properties for all relevant gases, excluding noble gases.

3. Methods

This chapter deals with all the methods and setups that were worked on and applied in order to date various environmental samples with noble gas radioisotopes ^{39}Ar, ^{81}Kr and ^{85}Kr. The chapter is subdivided into the 3 parts: sampling methods, sample purification methods and detection methods to analyze the purified samples. It represents the current capacities for taking and processing groundwater, seawater and ice samples for ^{39}Ar analysis at the Institute for Environmental Physics in Heidelberg, the sampling and sample preparation capabilities for ^{39}Ar, ^{81}Kr and ^{85}Kr analysis on groundwater samples and for atmospheric ^{85}Kr samples of the *Commonwealth Scientific and Industrial Research Organization (CSIRO)* in Adelaide, Australia, as well as the current ^{39}Ar detection method at the Kirchhoff-Institute for Physics in Heidelberg. The principles of gas proportional counters used in the Low-Level counting (LLC) laboratory at the University of Bern and at the *Bundesamt für Strahlenschutz (BfS)* in Freiburg will be presented in not too much detail, as not much work on those has been done in the context of this thesis.

3.1. Sampling methods

Due to their low isotopic abundance, comparably large amounts of pure argon and krypton are required for the analysis of ^{39}Ar, ^{81}Kr and ^{85}Kr. Table 3.1 lists the amount of argon and krypton required for analysis depending on the analytical method.

The large amounts of argon and krypton required for LLC hampers dating with ^{39}Ar and ^{85}Kr for ocean and ice samples. Hence, the only routine dating of environmental samples with ^{39}Ar is done on groundwater while dating with ^{81}Kr was practically impossible two decades ago. In that sense the development of the laser based atom counting method Atom Trap Trace Analysis (ATTA) is a game changer in the field of noble gas radioisotope dating (Lu et al., 2014).

Laboratories applying noble gas radioisotopes as dating tools have to adapt their sampling and purification routines to the analytical requirements for ATTA. Hence, the methods and setups described in the following represent the progress in this direction at the CSIRO and the Institute for Environmental Physics in Heidelberg.

Table 3.1.: Typical sample sizes required for ^{39}Ar, ^{81}Kr and ^{85}Kr analysis with Low-Level counting and current ATTA setups (Loosli, 1983; Jiang et al., 2012; Yang et al., 2013). The sample size for ice is estimated assuming an air content of 100 mL air/kg ice, which is approximately the case for polar ice, whereas for mid-latitude glaciers it may be substantially lower. Sample sizes for water are estimated for $T = 15$ °C and $S = 0$ ‰

	pure Ar or Kr	water sample	ice sample
For ^{39}Ar analysis:			
ATTA	2 mL	5 L	2 kg
LLC	400 mL	1000 L	400 kg
For ^{81}Kr analysis:			
ATTA	5-10 μL	100-200 L	40-80 kg
LLC	-	-	-
For ^{85}Kr analysis:			
ATTA	1 μL	20 L	8 kg
LLC	20μL	400 L	160 kg

3.1.1. Collecting ocean samples for ^{39}Ar

In the 1980s and 90s, hundreds of ocean samples were taken for ^{39}Ar analysis with LLC of which about 125 were measured. The effort for one sample was enormous. Up to six 250 L sampling containers, so called Gerard-Ewing bottles, which were used for ^{14}C sampling were needed to sample the required 1000 to 1500 L of ocean water for one ^{39}Ar data point. The containers were attached to a steel cable and were lowered to depth of up to 5000 meter where they were closed automatically and brought up to the research vessel. On board the water was degassed in a spray chamber and the gas was transported to Bern for further purification and measurement (Rodriguez, 1993).

Despite the valuable information gained from the data, the last ocean sample for ^{39}Ar was taken in the 1980s. With the advent of accelerator mass spectrometry (AMS) for ^{14}C analysis, the Gerard-Ewing bottles became obsolete and the extra effort for ^{39}Ar sampling was not considered worth doing. In May 2015, the first ocean samples for ^{39}Ar measurement after 3 decades were taken, this time for the analysis with the Argon Trap Trace Analysis (ArTTA) apparatus in Heidelberg, Germany. More detailed information about the scientific background of the ocean cruise and the ^{39}Ar data obtained from it is given in chapter 6. In the following the sampling procedure of sea water for ^{39}Ar analysis performed on the cruise is described.

As sampling containers, new and unfilled 27 L propane gas bottles were used. In preparation to the field campaign, the bottles' leak rate and with that the potential atmospheric contamination was investigated by helium leak testing and pressure build-up experiments and its impact on ^{39}Ar results was found to be below 1 pmAr when storing the samples for half a year (Beyersdorfer, 2016). 24 bottles were evacuated and filled with high purity nitrogen to a slight overpressure for shipment. On board the containers were evacuated again below 1 mBar through a three way valve connected to the inlet of the

bottle as pictured in Figure 3.1a.

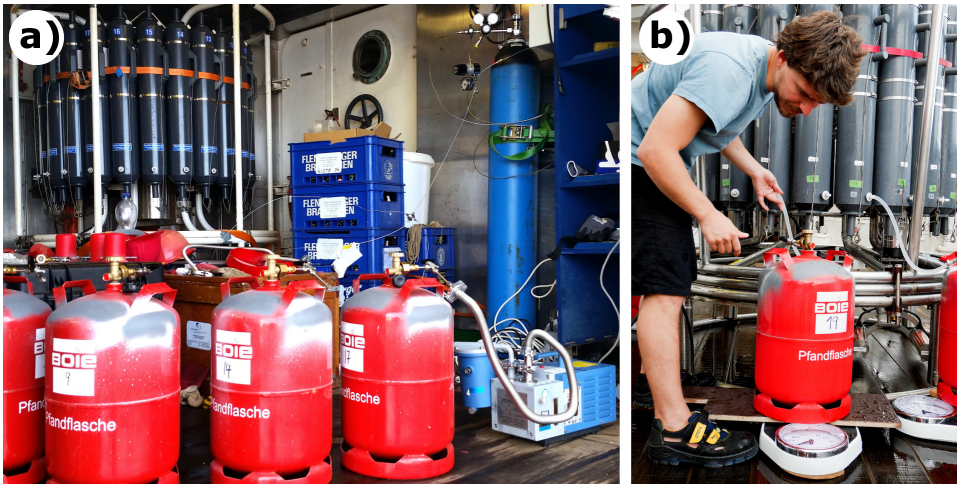

Figure 3.1.: a) Evacuating propane gas bottles on board. b) Sampling of sea water during the M116 ocean cruise

Along the cruise, three depth profiles were taken for ^{39}Ar analysis. For that, a so called CTD cast, which is a rosette with 24 Niskin bottles (each with 10L volume) and a CTD sensor is lowered to 4000m depth. On its way back to the surface, 3 Niskin bottles were closed at each target depth. CTD stands for conductivity, temperature and depth which are, amongst others, the main parameters that are constantly logged while taking a depth profile. The rosette with the Niskin bottles is pictured in Figure 3.1. A Niskin bottle is basically a plastic tube that has spring-loaded caps on each end and can be closed automatically when the rosette arrives at the target depth. The bottle has a valve on the bottom and an air screw on top for sampling of seawater later on deck.

The evacuated propane gas bottles were placed on a scale and ~7 L of each of the three Niskin bottles closed at the same depth were sampled (Figure 3.1b). The air screw was opened to allow for a water flow through the valve at the bottom. The first few hundred mL were used to flush the connections between Niskin bottle and propane gas bottle and the last 3 litres were discarded due to their contact with atmosphere.The 24 propane gas bottles (3 stations, 8 different depths) filled with ~20 L of seawater were closed by an additional brass lid and sent to the Heidelberg laboratory for degassing and purification of the dissolved argon.

3.1.2. Groundwater sampling for argon and krypton

Two different techniques for groundwater sampling for noble gas radioisotope analysis are currently used at the Institute for Environmental Physics in Heidelberg and were used in the scope of this thesis. For ^{39}Ar analysis with ATTA the same principle as for sampling seawater can be used. Evacuated propane gas bottles with a three-way valve connected to the inlet are simply filled with groundwater

extracted from a well with a submersible pump. Instead af a three way valve a T-piece can be screwed to the inlet of the bottle. In that configuration the pipes have to be flushed longer before opening the bottle in order to avoid any contamination from remaining atmosphere between the bottle inlet and the junction of the T-piece. The sampling process is again monitored by a scale to sample the right amount of water, i.e. sampling enough water to receive the required amount of argon while still having a large enough head space to allow for a good degassing efficiency in the lab.

When groundwater samples are taken for the analysis with LLC or for ^{81}Kr analysis, large amounts of groundwater are degassed in the field with a field gas extraction setup based on a membrane contactor. Two setups with a very similar design are used: one constructed by Thomas Reichel during his PhD which is designed for large sample sizes of more than 1000 L of water and a smaller one for several 100 L which was partly built in the context of this thesis. A detailed description of the first setup is found in the thesis of Reichel (2013) while in the following the setup for degassing hundreds of liters of water samples is described.

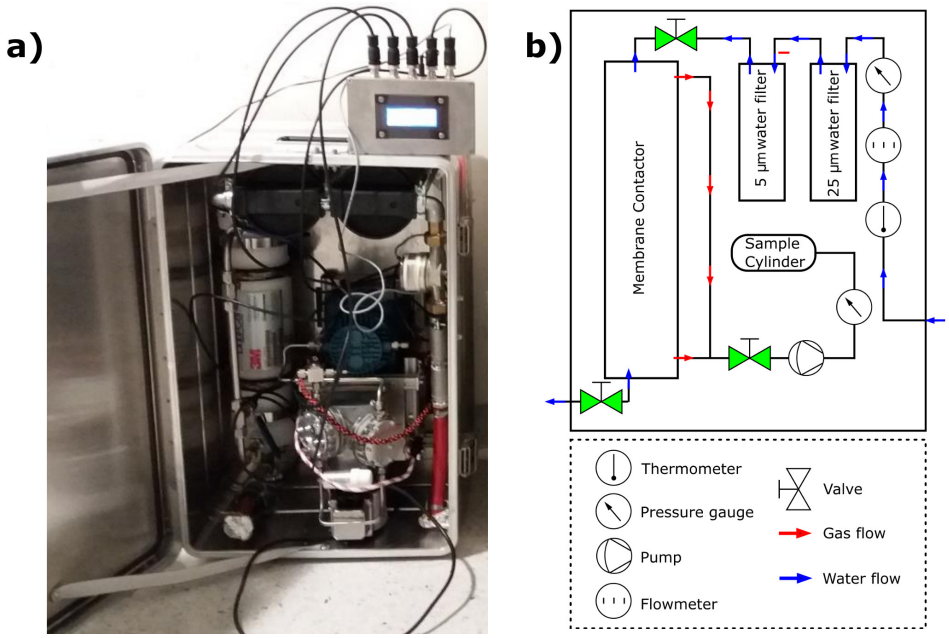

Figure 3.2.: A picture of the field gas extraction setup (a) and a sketch of the design (b).

The setup consists of a gas part and a water part. The extracted groundwater is first pumped through a 25 μm and a 5 μm water filter from *Infiltec*, enters a *LiquiCel* 4 x 13 membrane contactor and is finally flushed to the outlet. The membrane contactor is basically a polypropylen housing filled with hundreds of hollow fibers which build the gas side of the contactor. The water flows along the outside of the fibers and the dissolved gases diffuse through the fibre walls to the gas side of the contactor. The effective surface between water and gas side of the contactor is ~8 m^2. The gas part of the setup is further made of 1/2 inch stainless steel tubes attached to the vacuum side of the membrane contactor and is connected

to a vacuum pump setup. The pumps evacuate the gas side of the membrane contactor and compress the extracted gas into a sampling container.

The extraction process is monitored by *WIKA* pressure gauges on the water and on the gas side, by a thermometer and by a flow meter. The data acquisition is done with an *Arduino Mega* serving as A/D converter while the data is processed and stored with *LabView*.

Table 3.2.: Specifications of the field gas extraction setup.

Max water flow rate	57 L/min
Max water temperature	40 °C
Max water inlet pressure	5.2 Bar
Pressure on vacuum side	20 mBar
Max sample pressure	7 Bar
Power consumption	~600 W
Weight	40 kg
costs	~7300 €

In Table 3.2 the main specifications of the setup are listed. The setup tolerates high water flow rates, high pressures and comparably high water temperatures and with that, can be operated under most field conditions. As seen in Figure 3.2a, all parts are assembled and fixed in a reinforced aluminum *Zarges* box protecting the setup from dust and impacts in the field and during transport.

The power consumption is mainly due to the membrane pumps compressing the extracted gas in the sampling cylinder. Usually a submersible pump, like the MP1 from *Grundfos* is required to pump the water from a well through the setup. The power consumption of such a submersible pump is typically in the range of 1 kW so that a at least a 2 kW generator should be taken in the field when operating the field gas extraction unit. The maximum pump rate of the MP1 is ~30 L/min and in most cases a faster groundwater extraction is not needed. On the contrary, a higher pumping speed is often not recommended as the groundwater level might decrease too fast or an unwanted pressure gradient is produced, disturbing the natural groundwater flow.

The extraction efficiency of the setup depends on the water flow rate, the pressure gradient between water and gas phase in the contactor, the water temperature and the gas species. The manufacturer tested the extraction efficiency for O_2 in relation to the water flow through the contactor at 20 °C water temperature and for a pressure of ~40 mBar on the vacuum side of the contactor. With a water flow rate of 20 L/min the extraction efficiency is still 90 % and decreases to under 80 % for water flow rates above 38 L/min. As illustrated in Figure 2.11 the solubility of O_2 is comparable with that of argon and not too different of krypton, hence a similar extraction efficiency is expected.

This means, degassing 1200 L of water for 500 mL of argon, as needed for inter-comparison measurements between ATTA and LLC (Ritterbusch et al., 2014), takes about 70 min.

Reichel (2013) investigated if any isotopic fractionation occurs during extraction by comparing

$^{36}Ar/^{40}Ar$ ratios of a water sample with that of the extracted gas with mass spectrometry. No significant effect of fractionation could be found.

3.1.3. Atmospheric samples for ^{85}Kr analysis

In cooperation with the *Bundesamt für Strahlenschutz (BFS)* in Freiburg, Germany, a sampling station for atmospheric ^{85}Kr analysis on the southern hemisphere has been set up at the CSIRO in Adelaide. Since August 2015 weekly samples for ^{85}Kr have been taken and sent to the laboratories of the BFS in Freiburg. The evaluation of the by now more than two years of data is done in chapter 4.2. In this section the sampling procedure is described.

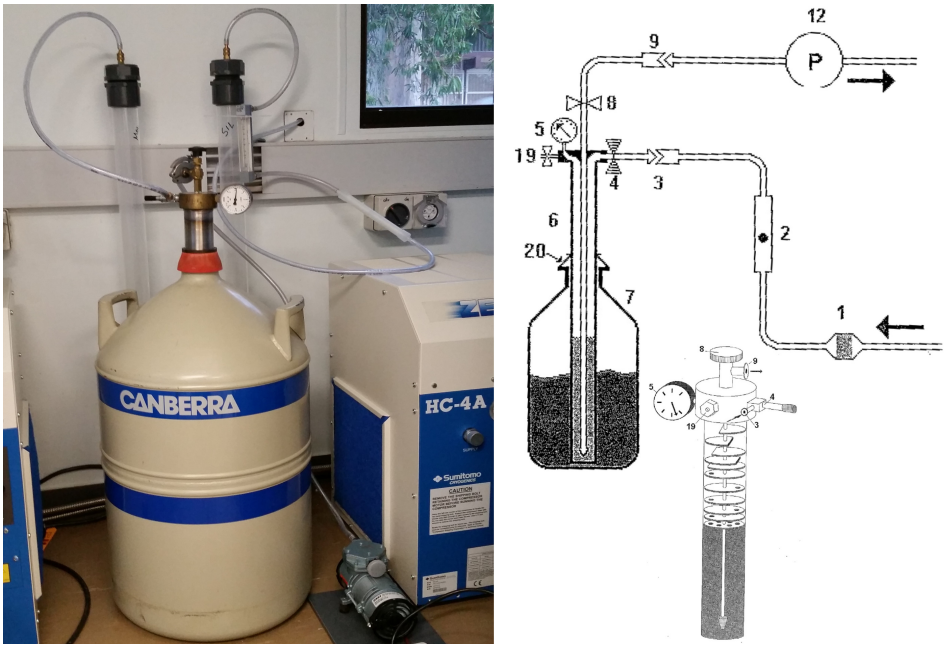

Figure 3.3.: Krypton sampling device for atmospheric ^{85}Kr measurement located at the CSIRO in Adelaide, Australia

The setup is displayed in Figure 3.3. It is basically a large stainless steel column filled with activated charcoal (AC) cooled down to 77 K by liquid nitrogen. Within one week ~10 m^3 of air are pumped through the column. A membrane pump at the outlet of the column generates the required pressure gradient and a dose valve at the inlet regulates the air flow to 60 L/h which is monitored by a flow meter. Two 1 m plastic tubes filled with zeolite can be connected in front of the inlet to remove most of the water vapor and prevent the columns to clog from frozen moisture.

As explained in section 2.5, heavier elements adsorb stronger on liquid nitrogen cooled activated charcoal, hence krypton and xenon are held back on the charcoal while nitrogen, oxygen and argon are flushed through the column. It is gas chromatography on activated charcoal over one week driven by the pressure gradient generated by the membrane pump.

Over one week 10 m^3 of air is flushed through the setup. With an atmospheric krypton concentration of 1.14 ppm this corresponds to around 11 mL of krypton trapped on the charcoal assuming no krypton was flushed off the column. Once the krypton sampling is done, a second trap is connected right away to guarantee a continuous collection of air. The trapped gas is now transferred to an evacuated 1 L *Minican* from *LindeGas* for shipment to Germany.

With an estimated adsorption capacity of 200 mL/g AC, several liters of nitrogen, oxygen and argon are captured on the cooled trap as well. So when the column is removed from the liquid nitrogen, the outlet valve (V8 in Figure 3.3) is kept open while letting the trap thaw for one hour such that the N_2,O_2 and Ar are released while Kr is still retained on the AC. Then all valves are closed and the column is turned upside down so that the water that passed the tubes filled with zeolite is collected at the outlet of the column. The setup remains like this during the night until the next day a slight overpressure of ~1 Bar has built up in the column.

The water is removed by carefully opening the inlet valve while keeping the column upside down and closing the valve as soon as gas starts leaving the column. Now the trap is heated to 300 °C in a specially designed oven, an evacuated *Minican* is connected to the outlet and a helium bottle is connected to the inlet of the trap (V4). Once the target temperature is reached, the desorbed gases are flushed into the *Minican* with a stream of helium up to a maximum pressure of 5 Bar (absolute pressure). The column is now regenerated by flushing it with helium for another hour while still being heated to 300 °C.The *Minican* is then sent to the BFS for measuring the ^{85}Kr concentration.

In Freiburg, typical krypton amounts of around 5 mL are finally filled into a gas proportional counter for analysis, meaning that more then 50 % from the initial krypton are lost, presumably mostly during the sampling routine at the CSIRO and partly during the purification of the sample at the BFS.

3.1.4. Ice samples from glaciers

According to Table 3.1 ~5 kg of ice are needed for analysis of ^{39}Ar with the ArTTA apparatus in Heidelberg. So far the required amount has been sampled by simply cutting out blocks of ice with a chain saw. Three settings are suitable for this method:

1. Sampling ice along different flow paths on a glacier surface
2. Sampling deeper ice layers at or close to the base of a glacier in ice caves
3. Sampling ice from a break-off edge of a glacier.

Ice blocks sampled under the first two settings have been purified during this thesis, while the sampling itself has been done on field trips conducted by Helene Hoffmann, Pascal Bohleber and Dietmar Wagenbach (Hoffmann, 2016).

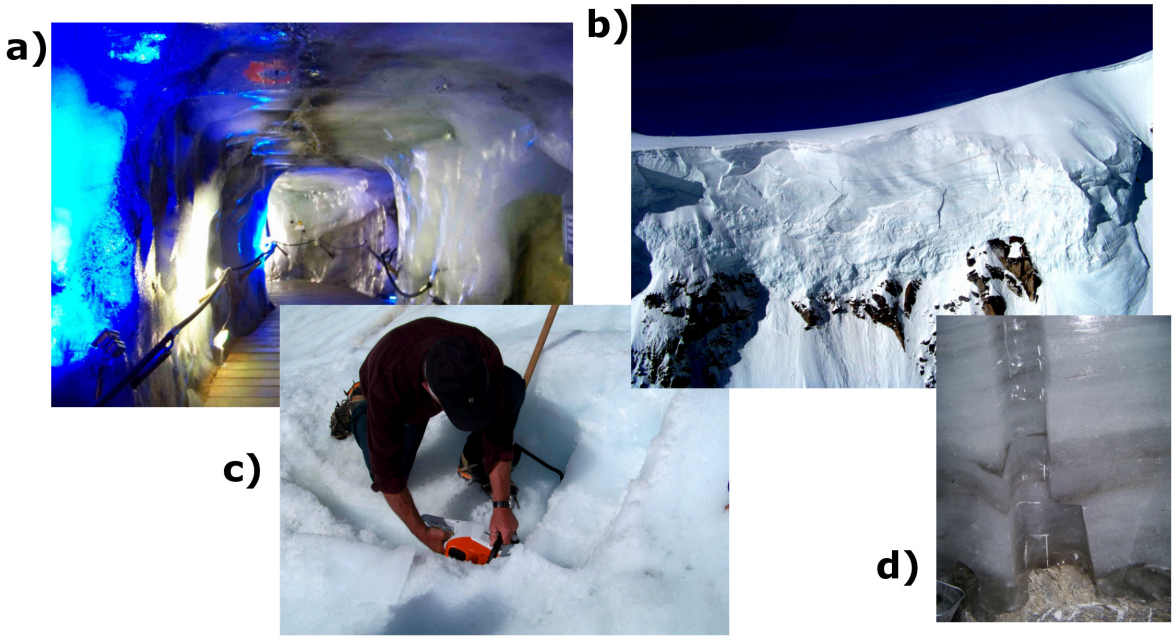

Figure 3.4.: A collection of photographs from different ice sampling campaigns (*Ice Group Data Base* 2017). a) The ice cave under the Chli Titlis, b) the 100 m deep ice cliff of the Colle Gnifetti, c) cutting out ice blocks on the gorner glacier and d) ice blocks taken out from the wall of the ice cave of the titlis glacier.

In July 2014, 27 large ice blocks have been sampled at the so called Gorner Glacier which originates at Colle Gnifetti, a summit on the border between Switzerland and Italy. At two locations, an upper and a lower site in the ablation zone of the glacier, ~10 kg ice blocks have been cut out with a chain saw and transported to Heidelberg, as seen in picture c) in Figure 3.4. According to flow models, the ice sampled on the lower site formed higher in the accumulation zone and traveled longer through the interior of the glacier, hence is expected to be older than the ice sampled at the upper sampling site (Wagenbach et al., 2014).

During several campaigns since 2014, ice samples were taken in ice caves beneath the so called Chli Titlis, a cold-based summit glacier in central Switzerland, and beneath the Stubai Glacier in western Austria. At both sites the ice caves penetrate the glaciers at the very bottom allowing sampling of the oldest ice at the base (picture a) and d) in Figure 3.4). The sampling is very convenient as the caves are tourist attractions with easy access via a ski lift and the ice blocks are again easily cut out with a chain saw.

An example for the third kind of sampling location is the east facing ice cliff at the Colle Gnifetti shown in Figure 3.4 b). Here the sampling procedure requires more skill and preparation as the ~100 m high exposed ice wall can only be reached with climbing gear by roping down over the edge. The advantage is, that samples can be taken from any layer and a whole record can be dated with ^{39}Ar.

For sampling in general it is aimed for 'white ice', which is ice with lots of entrapped air bubbles making the ice appear white. In contrast to that, sampling of the so called 'blue ice' should be avoided as it is usually formed when ice melts and refreezes again, hence contains almost no air and might lead to younger mean residence times as the frozen water could have been water in contact with the atmosphere that infiltrated deeper layers of the glacier.

During transport, the ice blocks often slightly melt on the outside and refreeze again in the ice room of the institute, so for a clean sample the topmost layers should be scraped off.

3.2. Sample purification methods

Two purification setups will be described in this section. The first is for separating argon and krypton from 5 to 80 L of gas. It was designed and constructed in Heidelberg and then shipped to the noble gas laboratory of the CSIRO in Adelaide. Reassembling, calibrating and applying this setup was a major project during the 14 month of employment at the CSIRO in the context of this thesis.

The second setup is for extraction and purification of argon out of ice, groundwater and seawater samples. The final version of this setup was mainly designed and built by the former master student Beyersdorfer (2016). Finalizing and calibrating the setup was done by the follow up master student Philip Hopkins while the data acquisition was done by the master student Viola Rädle. Supervision of that project and occasional hands-on work was done in the scope of this thesis.

3.2.1. Ar and Kr purification from 60 L gas samples

The setup is based on an existing argon separation setup located in Bern and constructed by Robin Riedmann during his PhD-Thesis (Riedmann, 2011). 2013, Reichel (2013) copied the setup for argon purification of groundwater samples for the first ^{39}Ar analysis with the ArTTA apparatus in Heidelberg. During his diploma thesis Kersting (2013) modified the Heidelberg setup to not only separate the argon but also the krypton fraction of a gas sample.

Based on the experience gathered during the diploma thesis, a third version of the original setup of Robin Riedmann was designed, including the steps for krypton purification. It was manufactured by the precision mechanic Norbert Winkler and the electrician Gerhard Zimmek.

The design of the setup

Figure 3.5 shows a sketch of the setup. The heart of the setup are 9 stainless steel columns of 4.20 m length and 1/2 inch in diameter, bent into a trumpet shape, connected in parallel and filled with Li-LSX zeolite. Here, the sample gas is separated via gas chromatography and the different gas fractions flushed off the columns are captured on liquid nitrogen cooled activated charcoal traps (ACT). Helium serves

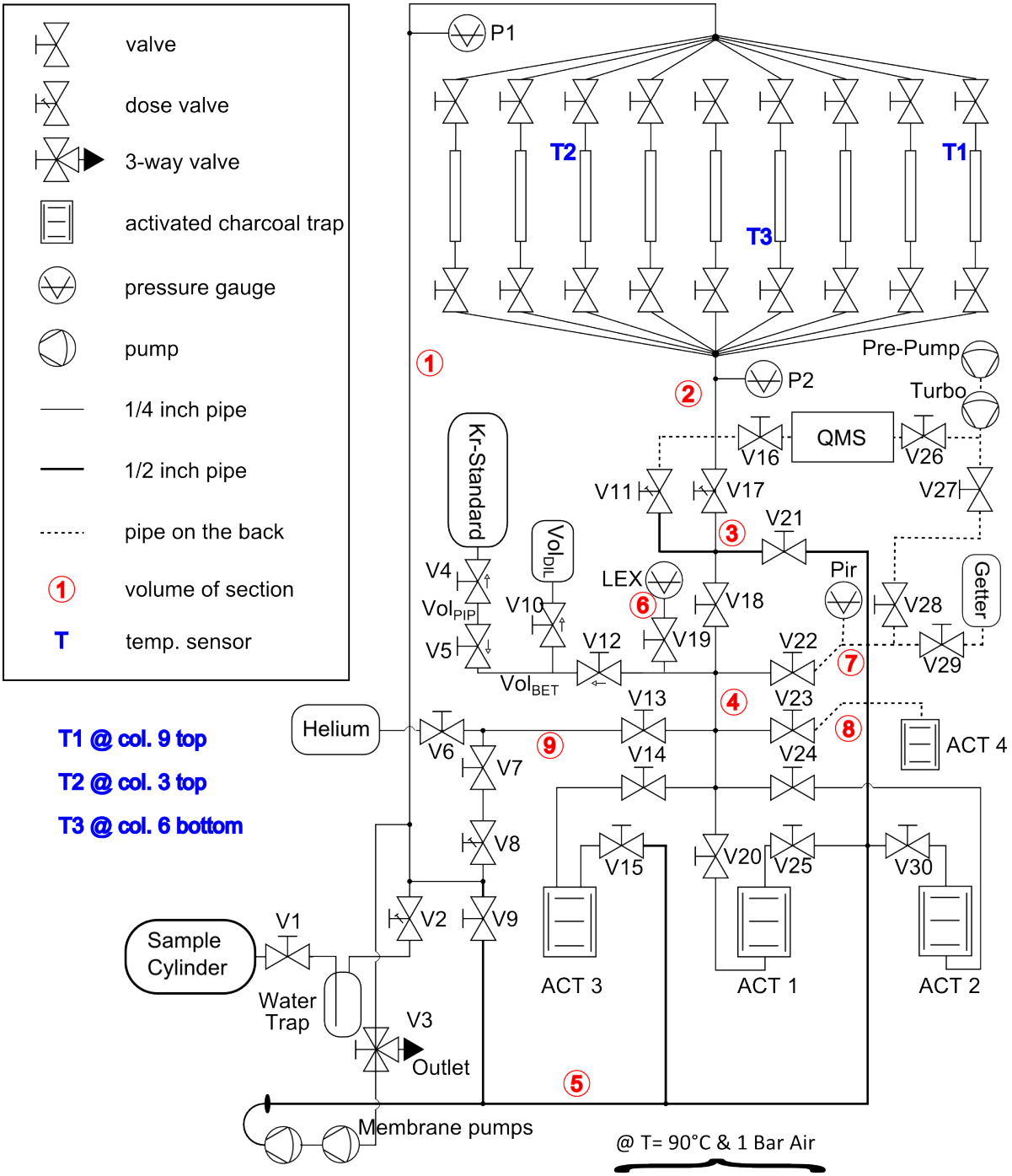

	S.C.	STD	PIP	BET	DIL	Getter	ACT 1	ACT 2	ACT 3	ACT 4	Err.
Vol [mL]	10000	6132	1.61	11.7	171.5	488	460	460	64	11	1%
	①	②	③	④	⑤	⑥	⑦	⑧	⑨		
Vol [mL]	189.2	165.1	29.8	15.7	280.1	2.4	15	3.9	7.5		

Figure 3.5.: Sketch of the separation setup located at the CSIRO in Adelaide, Australia.

as carrier gas and is circulated through the system by two membrane pumps. A RGA200 quadrupole mass spectrometer from *SRS*, in the following only called RGA (residual gas analyzer), is monitoring the gases leaving the columns.

Four pressure gauges operating in different pressure ranges are used to monitor the pressure regimes during different steps of the purification process. Two *WIKA* pressure transmitters for up to 10 Bar absolute pressure are located before (P1) and after the columns (P2). A LEX1 barotron pressure gauge from *Keller* is used to later calculate the amount of separated argon in a known volume via the ideal gas law (Equation 2.33). It has the highest precision with a measurement accuracy of ~1 % and goes up to 3 Bar absolute pressure. The 4th pressure gauge is a Pirani gauge operating in the range of -4·10^{-4} to 1 Bar. These models have a measurement accuracy of only 15 % and are highly sensitive to the present gas type. It is rather used for qualitative measurements under 1 mBar and to investigate how well evacuated parts of the setup are.

Three different types of pumps are used for different purposes in the setup. The membrane pump setup is used to circulate the carrier gas helium through the setup. It is a combination of a vacuum pump (N0150.3.AP.9E) and a compressor (N145.1.2AP.9E) both from *KNF Neuberger* which are connected in series. They were chosen because of their high pumping speed, and robust build. The vacuum pump evacuates down to 20 mBar while at the same time, the compressor can compress gas up to 7 Bar. The configuration was originally chosen for the field gas extraction setup build by Reichel (2013) but showed as well a very good performance for the argon separation setup. Both pumps require 3 phase power and in combination they have a power consumption of ~1.4 kW.

The second type of pumps used are two rotary vane pumps. The membrane pumps reach only pressures down to 20 mBar and with that, are not suitable to evacuate and clean the setup. This is done by a rotary vane pump which reaches pressures down to the 10^{-2} mBar range. The advantage of this pump type is, that it is comparably cheap, very reliable and easy to maintain. The big disadvantage is, that they require oil and potentially contaminate the entire system with a backstream of molecular oil when gas is sucked into the setup through the pumps when the operator is careless or as a result of a power outage. A second rotary vane pump is used as a pre-pump for a turbo pump to generate the required pre-vacuum of at least a few mBar.

This *Hi-Pace 80* turbo pump from *Pfeiffer Vaccum* is the third type of pump used in the setup. It has two purposes: First it generates the required pressure regime in the 10^{-8} mBar to 10^{-5} mBar range for the RGA that is mounted close to the pump. Secondly, it is used to evacuate parts of the setup that are crucial for the krypton purification, where too high pressure would otherwise lead to a significant contamination of the krypton sample.

The temperature of the columns is adjustable from -160 to +200 °C. To cool the column to a target temperature, a large Dewar is filled with ~40 L of liquid nitrogen and lifted up to immerse the columns into liquid nitrogen steam. A rotor whirls the steam to guarantee a homogenous cooling. The columns

are now heated via their ohmic resistance (R) to the required separation temperature by applying an electrical current (I):

$$P = U \cdot I = R \cdot I^2 \tag{3.1}$$

with: P : electrical power
U : voltage

The required electrical current and power is delivered by a power supply built by Gerhard Zimek. It is basically a transformator changing the 400V, 32A 3 phase input power to a maximum of 250A, 20V direct current. The power delivered can either be adjusted manually by a potentiometer or automatically by a PID controller. The design of the power supply for heating is similar to the one built for the Heidelberg argon separation and a more detailed description is found in Reichel (2013). The columns temperature is monitored by three PT100 temperature sensors attached to three different locations of the columns. Once the target temperature is reached, the required electrical power (P) equals the cooling power of the liquid nitrogen steam in order to stabilize the temperature. At -130 °C this corresponds to ~1 kW. To clean the columns after a separation, they are heated to 200 °C by removing the Dewar filled with liquid nitrogen and applying ~2.8 kW.

To apply this method of heating, a galvanic isolation between the columns and the rest of the setup is required. This is achieved by manufacturing adapters out of polyetheretherketon (PEEK) for connecting the columns with the rest of the system. It is a high temperature resistant plastic that can be machined with drills and mills.

For purifying the krypton fraction from remaining reactive gases, a *CapaciTorr HV 200* getter pump from *SAES* is used. It is optimized for removing large quantities of reactive gases in a high vacuum setting. Before operating it must be activated at 530 °C to 570 °C under high vacuum conditions. When operating the getter pump it has a working temperature of ~200 °C. According to the vendor, it has a capacity of 2 L for oxygen or 200 mL of nitrogen before it must be reactivated. The getter can be reactivated up to 100 times before the cartridge has to be replaced. During the krypton purification of one sample ~2 mL of reactive gases, mainly oxygen and nitrogen, are absorbed by the getter, hence about 100 samples can be purified before having to reactivate the getter.

Basically any kind of gas sample container can be connected to the setup. At the CSIRO, former commercial gas bottles for nitrogen or carbon dioxide with a volume of 10 L are used.

When the sample gas is loaded on the columns for separation, it is important that all moisture is removed to prevent a clogging of the columns. This is done by a stainless steel water trap, cooled by immersing it into a mixture of dry ice and isopropanol.

To determine the final krypton amount of the purified sample it is compared to a krypton standard. This is necessary as pressure measurements with the Pirani are not precise enough, especially when

traces of helium are present. The standard is a 6132 mL stainless steel container filled with 190 mBar of ultra-pure krypton. With a pipette ~300 μL of krypton are taken from the standard, which can be further split down by using a dilution volume. With this, different sizes of krypton standards can be used between 30 μL and 200 μL.

Chromatographic separation of argon and krypton

The purification of argon and krypton from gas samples can be subdivided into two steps. The gas chromatographical separation on the zeolite and the post-processing to further purify the separated gas fraction. To clarify the terminology, the first process will be referred to as argon and krypton separation, while the second process will be called the purification of the desired gas fraction.

A typical gas sample contains about 1 % argon but ~10^4 times less krypton. The separated argon fraction is usually already pure enough for analysis with ArTTA or LLC and doesn't need further purification. For krypton however, this does not hold true. This section will focus on the requirements for a clean separation while afterwards the further purification of the krypton fraction is described.

As written in section 2.5 the properties of zeolite lead to the following order of interaction potentials and with that to the order in which the gas fractions are flushed from the columns:

$$\Phi_{\mathrm{Ar}} \leq \Phi_{\mathrm{O_2}} \leq \Phi_{\mathrm{Kr}} \leq \Phi_{\mathrm{CH_4}} \leq \Phi_{\mathrm{CO_2}} \tag{3.2}$$

For a clean argon and krypton purification and a high recovery, the separation parameters have to be optimized to avoid an overlap of the different gas species leaving the columns and to improve the peak shape visible in the chromatogram of the RGA.

While the column length of 4.2 m and the zeolite as adsorbent are fixed parameters, the main adjustable parameter to improve the chromatographical separation are:

1. the temperature of the columns
2. the helium flow through the columns
3. the gas load on each column.

1. For a clean separation of the argon fraction, which is the first gas species leaving the columns, it must be separated from the second gas species (oxygen) being flushed off the columns. A separation temperature of -130 °C was found to be a good compromise between distance of the single gas peaks and the time required for the separation.

To separate the krypton, the third gas component being flushed from the columns, a clean separation from the oxygen and the methane or nitrogen peak is wanted. Therefore, the columns' temperature is raised to -80 °C for the krypton separation.

The initial cool down to -130 °C takes around 20 min while heating up the columns by 50 °C to -80 °C is done within 2 min.

2. Another factor influencing the chromatographical separation of the gas components is the flowrate of the carrier gas through a single column. An absolute flow rate can not be determined as the flow resistance of the single components are unknown and no flow meter is included in the setup. A relative measure is the pressure difference between inlet (P1) and outlet (P2) gas pressure of the columns. This can be regulated either by adding helium to or removing it from the system, or by regulating the flow resistance after the columns with valve 17. It was found, that a higher pressure gradient increases the separation performance so that the helium pressure before the column was regulated to 2 Bar and the flow resistance after the columns was decreased as far as possible. These findings are in agreement with those of Riedmann et al. (2016).

The pressure gradient changes after the argon fraction is separated, as the gas flow behind the columns is now directed through ACT2 and for the krypton separation through ACT3 which both have different flow resistances. The temperature is increased from -130 °C to -80 °C after the argon separation, which changes the adsorption properties of the zeolite and with that, influences the pressure gradient through the columns. Finally, the more columns are used for the separation, the lower the pressure gradient along each column as more gas adds up in front of the activated charcoal traps and behind the columns respectively.

3. The final parameter that can be adjusted is the number of columns used for the argon and krypton separation of a sample. A separation on only a few columns leads to a higher pressure gradient and with that to a better separation between the gas species. However, the zeolite in the columns has only a limited adsorption capacity and too much gas per column makes a clear separation of the peaks impossible. It was found that a sample load of 6 to 9 L per column is a good compromise. Hence, for a typical 60 L gas sample, 7 columns are used resulting in 8.6 L gas per column.

The calibrations of the setup was done with laboratory air. Hence, the composition is not very representative for real gas samples, which in most cases are extracted from groundwater. Figure 3.6 shows how the composition of the dissolved gases in groundwater can change due to subsurface processes. For the argon separation, this does not make a huge difference as a depletion of oxygen and a slightly higher relative argon concentration due to a higher solubility than nitrogen simplifies the separation. For krypton however this is different. On the one hand, because the relative krypton concentration in a groundwater sample is higher than in atmospheric air due to a higher solubility than nitrogen, oxygen and argon, making the separation of krypton easier. On the other hand, methane might be present which has very similar adsorption properties on zeolite as krypton and therefore, is flushed from the columns only slightly after krypton.

An important improvement of the separation efficiency that made a separation of the krypton and the methane possible in the first place was achieved by tuning the performance of the single columns.

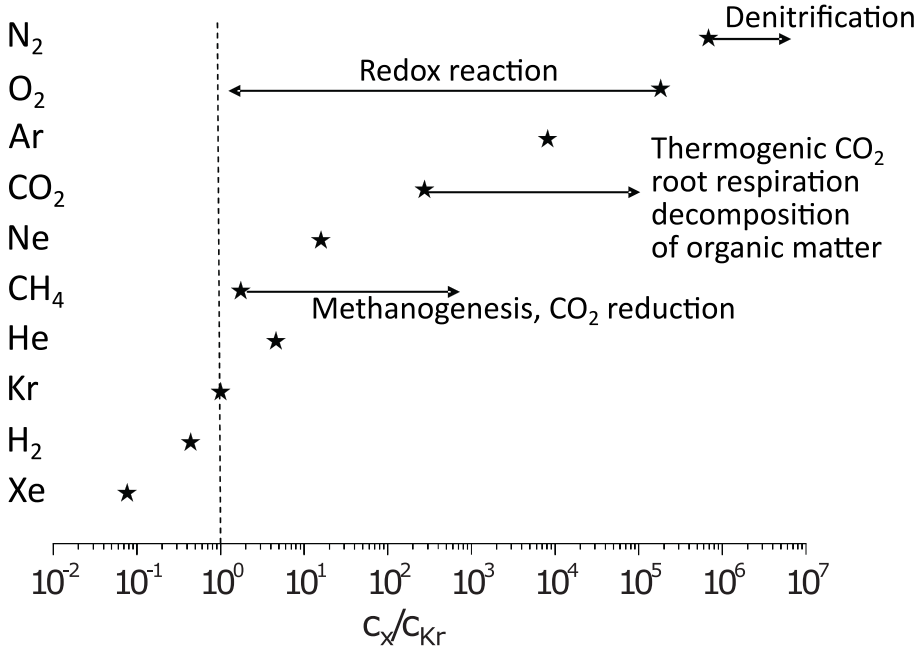

Figure 3.6.: Composition of atmospheric air relative to the Kr concentration in air and subsurface processes (arrows) affecting the composition of dissolved gases in groundwater (Purtschert et al., 2013)

Although all columns were filled with the same amount of zeolite, and the columns are bent and mounted in the same manner, slight differences are unavoidable resulting in a slightly different separation performance. This was tested by loading 63 L of laboratory air on all 9 columns and doing an argon separation under equal conditions for each column separately. The result showed that all columns had a varying chromatographic performance with column no. 1 being the 'fastest' meaning that the argon peak started about 3 minutes sooner and column no. 5 being the 'slowest', with the argon peak starting 5 minutes later than for the other columns on average. This meant for the separation of the krypton and the methane peak, that methane was flushed already from column no. 1 while most of the krypton was still on column no. 5, leading to an overlap of the krypton and the methane peak.

The flow resistance of the faster columns was now increased by squeezing the tubes at the outlet of the single columns with clamps. With this the peaks of all columns but column 5 could be shifted on top of each other. The chromatograms of these separations to tune the columns are plotted in Figure A.3 in the Appendix. As usually not more than 60 L of sample gas are separated, not all 9 columns are used and column 5 was left out for the routine sample preparation.

To illustrate the process and efficiency of the setup, the separation of the argon and krypton fraction of the sample 'Rottnest Island 3-93' is illustrated. In Figure 3.7 the chromatogram of the separation is shown.

The RGA is the main instrument to monitor the separation. The chromatogram shows the composition

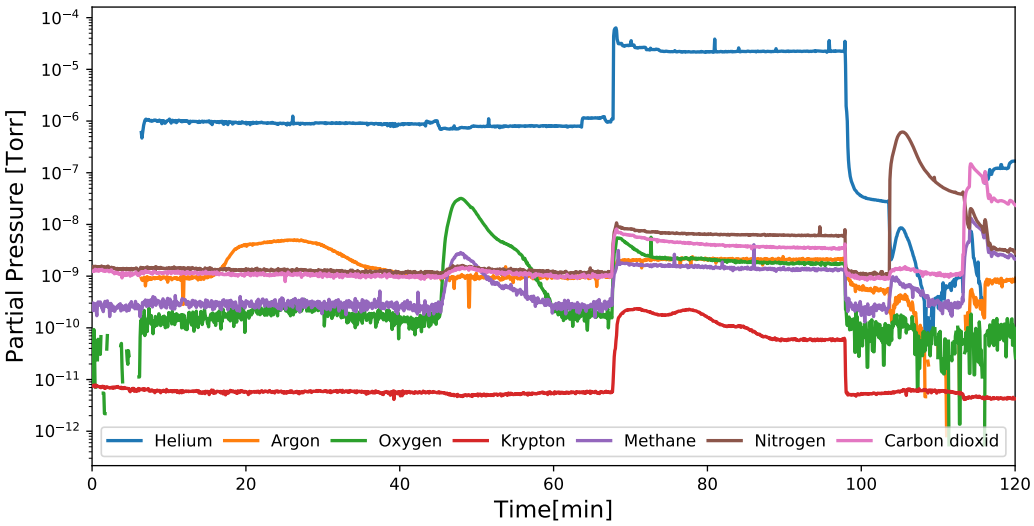

Figure 3.7.: Chromatogram of the argon and krypton separation of the Rottnest Island sample 3-93.

of the gases leaving the columns and is required to decide when to close and to open which activated charcoal trap and when to heat the columns from -120 °C to -80 °C. The helium signal is by far the strongest as it is the carrier gas. The first argon concentrations are measured 15 min after the start of the separation. Till minute 40 most of the argon is flushed from the columns and stored on ACT1. Now ACT2 is opened and the columns are heated first to -90 °C. Between min 45 and 63 the oxygen is trapped on ACT2. Although it is not required for the separation it is important to store the oxygen on a trap so that the helium can be circulated through the system by the membrane pumps and no oxygen reenters the columns.

Judging from the chromatogram one could assume that methane is flushed off the columns simultaneously to oxygen. However, it is not methane, but double ionized oxygen that is detected on mass 16 by the RGA as well. As a mass spectrometer distinguishes by the mass to charge ratio, $^{+}O_2$ is detected on mass 32 while $^{2+}O_2$ is detected on mass 16 as well as $^{+}CH_4$. After minute 100 an easy to identify methane signal is detected. It can't be $^{2+}O_2$ as nothing is detected on mass 32 (oxygen).

From minute 70 on ACT3 is opened, the temperature is set to -80 °C and the dose valve (V11) is opened further. The latter is the reason why the signal of all gases jumps up at the RGA and it is necessary so that the krypton signal can be detected at all by the electron multiplier of the RGA. The wiggles in the krypton signal from minute 70 on are a result of the fact, that the temperature is gradually risen to -80 °C as the heating tends to override. Each increase of a few degrees results in more desorbed krypton that is flushed from the columns. At minute 98 ACT3 is closed and all gas is pumped in the outlet while the columns are heated to 200 °C. From minute 100 on the remaining gases (mainly

nitrogen) are pumped from the column. This process was still monitored with the RGA, leading to high N_2 and CO_2 signals.

The separation of the argon fraction of this sample yields in a purity of more than 98 % with a recovery of more than 96 %. This is clean enough for analysis with ATTA or LLC, hence the argon is transferred from ACT1 to the activated charcoal trap ($ACT4_{Ar}$) for transportation of the argon to the analysis laboratory. ~95 % of the gas trapped on ACT3 consists of oxygen and nitrogen while the remaining 5 % is typically half krypton and half argon. This gas fraction has to be further purified for analysis of ^{81}Kr or ^{85}Kr.

Purification of the krypton fraction

Usually ~90 % of the initial krypton gets trapped on ACT3. Taking a 60 L atmospheric air sample as an example, about 2 mL of gas is trapped on ACT3 after the separation of which around 3 % are krypton. Summarizing this, the gas chromatographical separation of 60 L of gas containing 68.4 μL krypton yields in 2 mL of gas containing 61.6 μL of krypton.

Kersting (2013) gettered the remaining 2 mL on hot titanium sponge leaving only the argon and krypton fraction and yielding in a krypton purity of between 60 and 80 %. The setup in Adelaide uses an commercial getter, HV200 from SAES to remove the reactive gases. But before that, an additional step of cryogenic distillation on activated charcoal is added to further remove the argon. This is done by pumping ACT3 with a turbo pump while still cooling the trap with liquid nitrogen. Then the Dewar of ACT3 is removed and the trap thaws for 5 minutes while still being pumped. This process is monitored with the RGA and stopped as soon as krypton is released from the trap as well. As krypton adsorbs stronger on activated charcoal than argon (section 2.5) this separation process reduces the argon fraction by a factor of 10 without significant loss of krypton. The remaining gas is gettered and finally stored on $ACT4_{Kr}$. In Figure A.1 in the Appendix, the RGA scan of the cryogenic distillation and gettering process is displayed.

The purity of the final krypton fraction is determined by the RGA to be typically larger than 90 % while the remaining gases are argon, helium and hydrogen. To determine the final amount of krypton, the krypton standard described earlier is used. Pipettes with different krypton amounts are taken and compared to the purified sample by measuring both with the RGA and comparing the krypton signal under the same conditions (Figure A.2).

The steps for the entire argon and krypton purification are listed in table 3.3. A detailed description of each purification step can be found in the manual of the setup (Kersting, 2016).

The entire process takes about 6 h and 10 min and yields in an argon purity of 99.6 % with a recovery of > 95 % and a krypton purity and recovery of approx. 90 %.

Table 3.3.: Procedure of the argon and krypton purification of 60 Liters of sampling gas from a groundwater sample.

Timeline	What to do
30 min	cooling columns to -130 °C
15 min	loading the sample gas onto the columns
100 min	separating and storing the argon and krypton fraction
45 min	heating and cleaning the columns
30 min	processing and transferring the argon fraction
15 min	reducing the argon in ACT3 by thawing and pumping
45 min	gettering the krypton fraction
30 min	determining the krypton amount and purity
15 min	transferring the krypton fraction
45 min	cleaning the complete setup and preparing for the next sample
370 min	required time for the complete sequence

3.2.2. Ar purification for small samples

Since the required sample size for ArTTA has reduced to a few mL of argon, a new purification setup for water samples between 5 and 25 L or ice blocks of 2 to 10 kg has been built. Stefan Beyersdorfer designed it based on the purification setup that he developed in his master thesis (Beyersdorfer, 2016).

The idea of the setup is, that the argon of gas samples of < 1 L can be purified by simply removing all reactive gases with getter pumps. As discussed in section 2.5, the best suited getter material for this purpose is titanium sponge, as it is the best compromise found between large capacity and a low prize.

Unfortunately titanium sponge has to be heated to at least 650 °C to overcome the activation energy for nitrogen and even higher for methane. This is why the components most sticking out in Figure 3.8 are two big ovens from the company *Horst*, each surrounding a 25 cm long steel tubes with a diameter of 4 cm, filled with titanium sponge, which are the getters. For purification, two getters are used. First a hot one to remove all reactive gases and then a getter at room temperature to adsorb hydrogen. The ovens can be heated in steps of 1 °C up to 1000 °C, while the getters are made out of high-temperature-steel enduring temperatures of up to 950 °C. The ovens are mounted on slides to move them on and off the getters when they need to cool down or the titanium sponge need to be renewed.

A RGA100 from *SRS* is used to monitor the gas composition at two locations of the setup. In the inlet part it analyzes the gas extracted from the sample and in the volume behind the getters, it analyzes the purity of the gettered argon fraction. At both locations a dose valve is used to regulate the gas amount entering the RGA chamber.

The RGA is mounted on top of an *Hi-pace 80* turbo pumps from *Pfeiffer Vakuum* that generates the required high vacuum for operating the RGA. A *Vario SP1* membrane pump from *Vacuubrand* is used as pre-pump for the turbo pump. A very similar pump setup is used for evacuating the entire setup. Here the membrane pump operates both, as pre-pump for another turbo pump and with a different valve

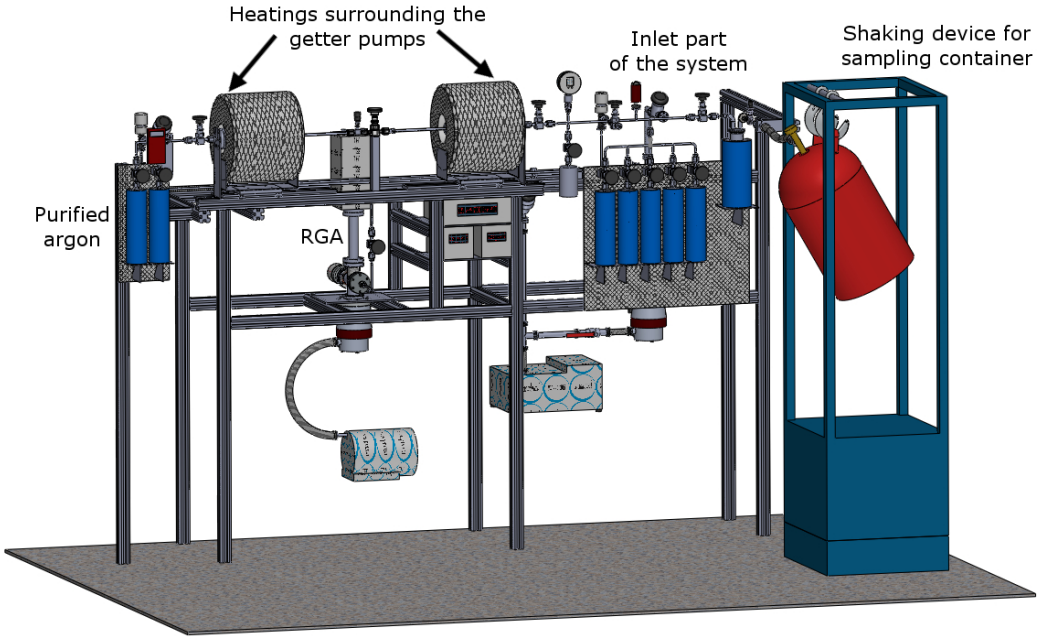

Figure 3.8.: Sketch of the argon purification setup for small samples

configuration, as a pump to evacuate the entire system down to 1 mBar. Once that pressure is reached, the turbo pump is turned on to evacuate the system to < 10^{-3} mBar.

Four different types of pressure gauges are used to either monitor the purification process or the pressures in specific volumes. Two Pirani gauges are used to ensure that the pressure between pre-pumps and turbo pumps does not exceed 10 mBar as it would harm the turbo pump. Two cold cathode ionization gauges monitor the pressure in front of the turbo pumps for pressures under 10^{-3} mBar. Another Pirani gauge and an absolute pressure gauge monitor the pressure in the inlet part and cover a range of 10^{-3} mBar to 3 Bar. Finally a Piezo/Pirani pressure gauge is used to monitor the pressure behind the getters. It covers a broad pressure range from 10^{-3} mBar to 1200 mBar and with a measurement accuracy of ~0.3 % for a pressure above 10 mBar it is well suited to determine the final purified argon amount.

Seven activated charcoal traps (ACTs) are included in the setup, five in the inlet part and two connected to the volume after the getters. This should allow for processing samples in parallel while up to five samples can be degassed before gettering them. The first ACT behind the getters is used as a pump to suck the argon through the getter and store it, while the second ACT behind the getters is the trap for transporting the final argon fraction to the ArTTA setup for analysis.

For the last field campaigns, mainly new and empty propane gas bottles were used as sampling containers for water. Beyersdorfer (2016) found an elegant solution to connect them to the system while being able to shake them for degassing. He constructed a metal frame with hooks to hang in the bottles

and built an arm attached to a motor of a wind screen wiper to generate the required shaking motion.

Two times during the purification, gas amounts are determined by measuring the pressure in a known volume. In order to apply the ideal gas law (Equation 2.33) the temperature of the gas must be known as well. An average gas temperature is hard to estimate, as the gas is released from ACTs that are heated to 100 °C. So the two relevant volumes have been calibrated with known air and argon amounts. With that a calibration function is determined giving the gas and argon amount for a specific pressure in that specific volume under the same temperature conditions as during a real separation.

After describing the setup and its single components, the purification steps for water or ice samples will now be introduced. The sample processing can be subdivided into two steps:

1. Degassing of the sample

2. Purifying the extracted gas

1. A water sample, typically sampled in a propane gas bottle is mounted in a shaking device and connected to the inlet of the setup. The degassing is simply done by freezing all gases onto one of the 5 ACTs cooled with liquid nitrogen. The stream of gas flows through a water trap cooled with a mixture of isopropanol and dry ice to prevent moisture from entering the vacuum system. Depending on the headspace in the propane gas bottle, it is shaken to speed up the degassing. Beyersdorfer (2016) found that if the ratio of the headspace to total volume of the propane gas bottle is only 8 %, still 98 % of the argon is extracted after 2 consecutive cycles of extracting the gas in the headspace and shaking.

For ice samples, the ice block is first prepared in a -20 °C cold chamber. Here, all layers of blue ice are cut off and the block is cut to the right size to fit in the ice container. The container of ~14.2 L volume is then attached to the purification setup and evacuated to the 10^{-2} mBar range. Then the ice is melted by either heating the container or by letting the ice thaw over night at room temperature. Shaking during degassing is not necessary, as usually after melting the volume of the headspace is in the same order as the water volume and with that >95 % of the argon is already in the headspace. Once the ice block melted, the air, formerly trapped in the ice, is again frozen onto an ACT.

2. The purification of the argon in the gas is done on two getters filled with titanium sponge. The first one is heated to 900 °C while the second one is kept at room temperature. First the gas amount and composition is determined by heating the ACT and expanding the gas into the volume which was calibrated with air as described above. An RGA is used to measure the gas composition. Now the first getter is opened and the reactive gases are absorbed on the 900 °C hot titanium sponge. The pressure drop is monitored with a LabView programm that reads out all pressure gauges. Once the pressure stays constant, the second cold getter is opened to adsorb all the hydrogen that was produced and desorbed in the first getter. The outlet of the second getter is opened and the pure argon is stored on another liquid nitrogen cooled ACT. The final argon amount is again determined via a pressure measurement

in a volume calibrated with known argon amounts and the purity is determined by the RGA. Then the argon fraction is frozen on an ACT to transport the purified sample to the ArTTA setup.

The entire procedure takes ~2 hours for a water sample and up to one day for an ice sample, depending on how big the ice block was and with that, how long it takes to melt it. With a purity of >98 % and a yield of >95 % the efficiency is similar to the argon separation setup.

The remaining argon fraction contains all noble gases as they do not interact with the titanium sponge. In the near future additional steps are planned to further separate the krypton out of the final noble gas fraction to measure ^{81}Kr and ^{85}Kr with an ATTA setup.

3.3. Detection Methods

Three detection methods have been used so far to detect ^{39}Ar, ^{81}Kr and ^{85}Kr, accelerator mass spectrometry (AMS), Low-Level counting (LLC) and atom trap trace analysis (ATTA). The analysis with AMS is not further described here, as there are no measuring facilities for neither ^{39}Ar nor ^{81}Kr/^{85}Kr available. For information on noble gas radioisotope analysis with AMS, Collon et al. (2004) is recommended.

3.3.1. Atom Trap Trace Analysis

Atom Trap Trace Analysis (ATTA) was developed for ^{81}Kr and ^{85}Kr by the group of Zheng-Tian Lu at the Argonne National Lab in Chicago (Chen et al., 1999). In 2008, the group of Markus Oberthaler started building an ATTA system for ^{39}Ar at the Kirchhoff-Institute for Physics in Heidelberg (Welte, 2011). The Heidelberg apparatus is currently the only ATTA setup capable of measuring ^{39}Ar on environmental samples. In the following the Heidelberg system, referred to as Argon Trap Trace Analysis (ArTTA) will be introduced. Further literature on ATTA setups for krypton can be found in Jiang et al. (2012) and Tu et al. (2014).

In ATTA, single ^{39}Ar atoms are slowed down by laser cooling, trapped in a magneto-optical trap (MOT) and detected via their photon emissions. The key feature of this method lies in its high selectivity to only trap the desired ^{39}Ar atoms and not the 10^{15} times more abundant ^{40}Ar atoms (or any other element). This is achieved by millions of resonant photon scattering processes. So the decisive advantage of the ATTA method is based on the two principles, resonance and repetition. In Figure 3.9, the physical processes behind these principles are illustrated. In order to manipulate the ^{39}Ar atoms, a suitable closed electronic transition in the energy spectrum of the atom is required that can be addressed with a laser. It would be the most efficient way to excite it from the ground state, unfortunately the desired transitions lie in the deep UV spectrum and so far, no available laser exists for this wavelength range. As seen in the energy spectrum of ^{40}Ar in the left plot, a cooling transition is found for a meta-stable state at 812 nm, exciting the valence electron from the $1s_5$ to the $2p_9$ state.

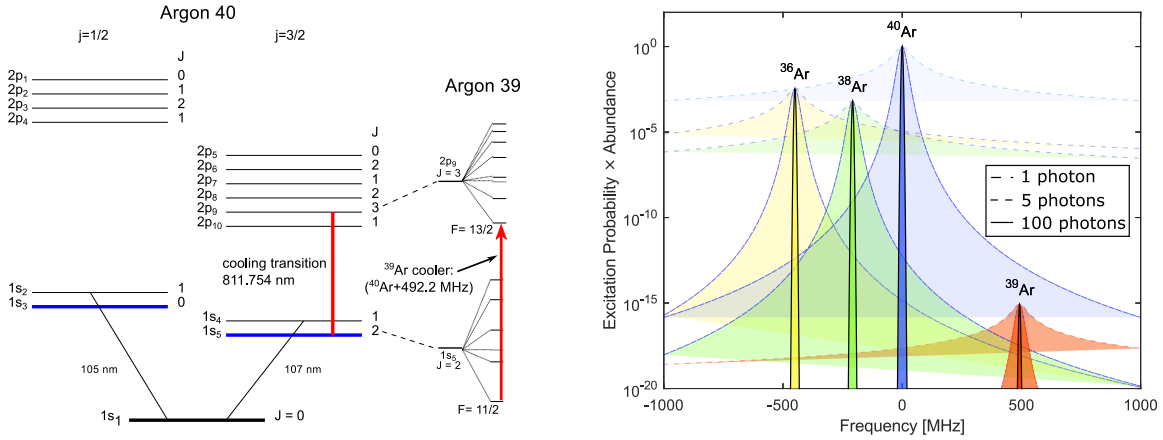

Figure 3.9.: The left plot displays the energy spectrum of ^{40}Ar an the desired cooling transition of ^{39}Ar (Ritterbusch, 2014). On the right, the probability for photon scattering events by the relevant argon isotopes is plotted against the cooling laser frequency.

Due to its odd nucleus number, ^{39}Ar possesses a nuclear spin of 7/2 leading to a hyperfine structure splitting. Furthermore, the energy spectrum differs slightly compared to ^{40}Ar because of the isotopic shift caused by the lower mass of the ^{39}Ar atom and the nuclear spin. Shifting the cooling laser frequency by ~500 MHz from the ^{40}Ar transition frequency, the desired ^{39}Ar transition is found.

In the right panel in Figure 3.9, the excitation probability for the relevant argon isotopes is plotted against the cooling laser frequency around the ^{40}Ar cooling transition. The plot illustrates the following considerations, which are explicated based on Ritterbusch (2014). The probability for one photon in resonance with the desired ^{39}Ar cooling transition to excite an ^{40}Ar atom can be estimated by:

$$\frac{\Gamma^2}{4\Delta f^2} \approx \frac{1}{3000} \tag{3.3}$$

with Γ : natural line width of atomic transition of ^{39}Ar (5.87 MHz)
Δf : frequency difference of ^{40}Ar resonant transition (492.2 MHz)

Multiplying this probability with the isotopic ratio, results in the relative scattering probability for one photon by ^{40}Ar:

$$\frac{\Gamma^2}{4\Delta f^2} \cdot \frac{^{40}\mathrm{Ar}}{^{39}\mathrm{Ar}} \approx 4 \cdot 10^{10} \tag{3.4}$$

Hence, the probability for one photon to excite an ^{40}Ar atom is by 10 orders of magnitude higher than to excite an ^{39}Ar atom. The relative probability that N photons are scattered by ^{40}Ar is then given by:

$$\left(\frac{\Gamma^2}{4\Delta f^2}\right)^N \cdot \frac{^{40}\mathrm{Ar}}{^{39}\mathrm{Ar}} \tag{3.5}$$

The relative probability that 10 photons are scattered by ^{40}Ar lies already under 1 %. In order to slow down ^{39}Ar atoms sufficiently for trapping them in the MOT, ~10^6 photon scattering events are necessary. Thus, the probability to accidentally trap an ^{40}Ar atom is virtually zero.

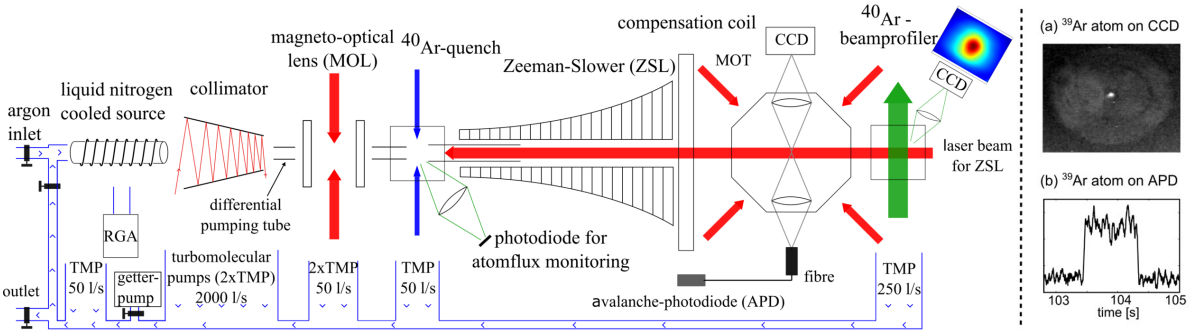

Figure 3.10.: Sketch of the ArTTA setup at the Kirchhoff-Institute in Heidelberg. The pictures on the right show the detection of an ^{39}Ar atom in the magneto optical trap (Ritterbusch et al., 2014).

Figure 3.10 displays a sketch of the ArTTA apparatus at the Kirchhoff-Institute in Heidelberg. When the argon of a purified sample is introduced into the liquid nitrogen cooled source of the ArTTA apparatus, the atoms are excited to the metastable state in a radio frequency plasma. The following steps are mainly to collimate and slow down the atom beam longitudinal from initially ~280 m s^{-1} to finally ~10 m s^{-1} which is the trapping velocity of the MOT. Transversal laser cooling is achieved in a tilted mirror setup, the collimator. The atom beam is focused by a magneto-optical lens and then, enters the Zeeman slower. Here, an external magnetic field compensates the Doppler shift that occurs when the atoms slow down and by that, would get out of resonance with the cooling laser. Finally, the ^{39}Ar atoms get trapped in the MOT for about half a second during which they scatter about 10^6 photons. This event is detected by a CCD camera as well as an avalanche photo diode, pictured in Figure 3.10.

When the setup was first operated, argon highly enriched in ^{39}Ar was measured in order to optimize the ArTTA system. This procedure introduced a strong contamination in the system. Even many years later, significant amounts of ^{39}Ar are still outgassing from the vacuum parts. This hindered to use the setup in recycling mode for a long time, hence argon samples of more than 600 mL were needed for the first groundwater study with ArTTA (Ritterbusch et al., 2014). Since relevant parts of the vacuum chamber have been replaced, reducing the contamination significantly, the setup runs in recycling mode, with typical sample size of 2 mL of pure argon (Ebser, 2018).

The count rate and the stability of the apparatus are the key parameters that are optimized. Currently the biggest loss in efficiency is in the source. Only ~10^{-4} of ^{39}Ar atoms present in the source are excited to the metastable state. The count rate of the apparatus for a modern atmospheric argon sample has increased over the last 4 years from 3.6 atoms/h (Ritterbusch et al., 2014) to 6.5 atoms/h (Ebser, 2018). Only considering the statistical error of the atom counting with a total number of n atoms and

the standard deviation of $\sigma \propto \sqrt{n}$ leads to 15.4 h of measuring time for a modern sample to have an error on the atmospheric count rate of 10 %.

The ^{39}Ar concentration C of a sample is determined directly from the count rate by comparing it to an enriched sample with known ^{39}Ar concentration of about 10 times the atmospheric ^{39}Ar concentration. The ^{39}Ar concentration in a sample is then given in percent modern argon (pmAr) by simply dividing the count rate (R) of a sample by the count rate of the reference sample.

$$C^{^{39}\mathrm{Ar}}_{\mathrm{sample}} = \left(\frac{R^{^{39}\mathrm{Ar}}_{\mathrm{sample}}}{0.1 \cdot R^{^{39}\mathrm{Ar}}_{\mathrm{ref}}} \right) \quad [\mathrm{pmAr}] \tag{3.6}$$

The difficulty is to correct for the contamination and the instability of the setup. A detailed explanation of the current measurement evaluation is found in Ebser (2018).

3.3.2. Gas Proportional Counter

In the first part of this section, the counter setup that was worked on during the stay at the CSIRO in Adelaide is described. Originally, the setup was located at the *Leipniz Institute for Applied Geophysics* in Hannover, Germany, several years ago and was used for measuring ^{14}C. When it was taken out of service, it was dismounted and shipped to Australia. Six tons of lead and electronics from the 1980s packed in boxes were waiting at the CSIRO to get reassembled for ^{85}Kr analysis. In the second part, the counting setup used at the Bundsamt für Strahlenschutz in Freiburg, Germany is presented. Here, the atmospheric ^{85}Kr samples collected in Adelaide were analyzed, as the ^{85}Kr counting system at the CSIRO was not yet operational. In the third part of this section, the Low-Level counting laboratory in Bern is described, as samples for ^{39}Ar and ^{85}Kr taken during the Rottnest Island field campaign have been measured there. The precision and required time for decay counting mainly depends on the activity of the specific sample.

Table 3.4.: Specific activity of modern ^{39}Ar, ^{81}Kr and ^{85}Kr in decay per minute in 400 mL of pure argon and 50 μL krypton respectively, calculated from their atmospheric concentrations and half-lives.

	^{39}Ar	^{81}Kr	^{85}Kr
sample size	400 mL	50 μL	50 μL
specific activity	$(4.4{\cdot}10^{-2} \pm 4.8{\cdot}10^{-3})$ cpm	$3.4{\cdot}10^{-6}$ cpm	0.85 cpm

Table 3.4 gives the specific activities for the three noble gas radioisotopes in 400 mL argon and 50 μL krypton respectively, which corresponds to argon and krypton extracted out of ~1000 L water. Assuming an idealized decay counting device with zero background, a counting efficiency of 100 %, a modern argon and krypton fraction and an aimed measurement accuracy of 5 %, then it would still take a measurement time of 7.8 h for ^{85}Kr, 6 d 8 h for ^{39}Ar and ~224 yr for ^{81}Kr to detect the required 400

decays for the desired precision of 5 %.

Gasproportional counter for ^{85}Kr in Adelaide

Setting up the counting system for ^{85}Kr analysis was the second main task during employment at the CSIRO in the context of this thesis. Unfortunately the setup could not be brought to the state to actually measure ^{85}Kr within this time frame. But working on the setup was a valuable experience in deepening the understand for the method of decay counting with gas proportional counters.

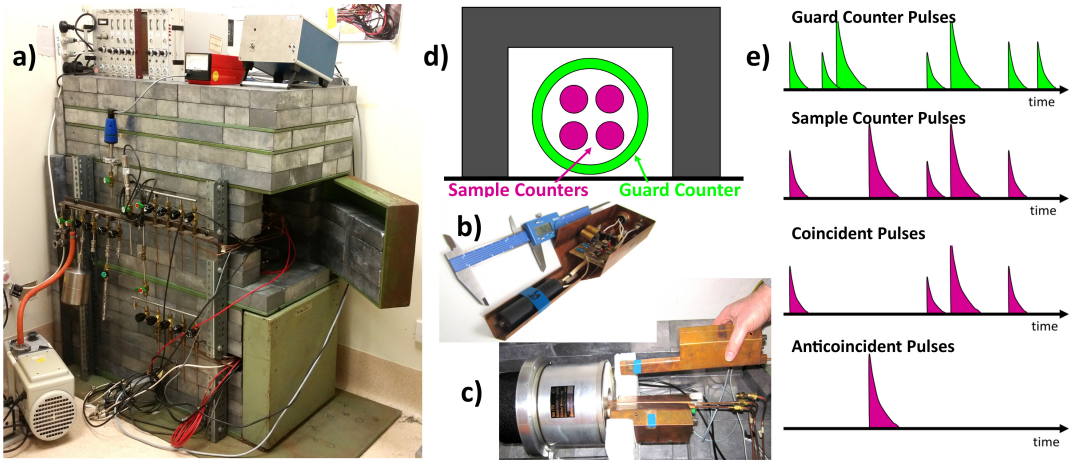

Figure 3.11.: a) Two chambers each containing one guard counter and four gas proportional counters (GPs). Six tons of lead are shielding the counters from background radiation and cosmic rays. An inlet vacuum system is mounted to the front and a high voltage supply stands on top of the setup. b) A GP consisting of a copper tube filled with the sample gas and a pre-amplifier connected behind the tube. c) The guard counter surrounding the GPs. d) A sketch of the guard and gas proportional counters. The colors refer to the peaks in sketch e). e) The principle of anti coincidence counting: An event that occurs simultaneously in the guard and the GP counter is discarded.

The vacuum system and lead housing was rebuilt mainly in its old design as it was used for ^{14}C analysis in Hannover. The old electronic readout and the *BASIC* based software written for MS-DOS was replaced by an up-to-date high resolution analog to digital converter from *National Instruments* and a new software written in *Lab-View*.

The setup consists of two lead chambers, a lower one and an upper one. Each chamber contains a guard counter that surrounds 4 gas proportional counters (GPs) (Figure 3.11c). The guard counter is a thallium-doped sodium iodide scintillation counter (NaI(Tl)), one of the most widely used scintillators as it has a high performance while still being comparably inexpensive. The GP counters are basically just copper tubes, 7 cm long, 2 cm in diameter with an inner volume of ~20 mL, with a fine wire in the center, being the anode while the copper wall works as cathode. When an ionizing particle enters a GP filled with counting gas, electron and positive ion pairs are formed and are attracted by the anode and

cathode respectively. Such an event results in a short voltage drop which is amplified by an electric circuit connected directly to the GP counter. As the signal will be amplified again later, this electronic component acts as a pre-amplifier.

The counters are evacuated and then filled with the sample gas and counting gas via an inlet system mounted to the front of the setup. The old system for ^{14}C used CO_2 as counting gas. The counters were filled by simply freezing the sample together with the counting gas onto a copper finger and letting it expand into the GP. This however, is not possible for krypton as its vapor pressure is still ~3 mBar at liquid nitrogen temperature. A new method for filling the counters was tested by freezing the krypton onto activated charcoal in a U-shaped trap and flushing it into the counters with CO_2 (serving as counting gas) while heating the charcoal trap. The efficiency of this method could not be evaluated as first, more work had to be done on the signal processing of the electronic readout.

As written in chapter 2.2, ^{85}Kr β^--decays with a 99.57 % probability to ^{85}Rb with a maximum kinetic energy of the β-particle of 687 keV and an average kinetic energy of 251 keV. Whether all of the kinetic energy of the electron is deposited into the counting gas highly depends on the geometry of the counter, the pressure and type of counting gas used and the location a ^{85}Kr atom has decayed at within the counter. Still, the voltage drop between anode and cathode as consequence of a decay event is proportional to the energy of the created particles or photons. Hence, a specific voltage window can be given outside which an event could not have been caused by a β-particle of a ^{85}Kr decay.

The principle of anti-coincidence counting is illustrated in Figure 3.11 d) and e). The main idea is, that all events caused by the decay of ^{85}Kr in the GP counter only result in a signal of the GP counter, as the β-particle deposits all its energy either in the counting gas or in the copper wall of the GP counter. Hence, when both, the guard counter and the GP counter detect an event simultaneously, it was not caused by a ^{85}Kr decay, but by an external particle, like cosmic rays or background radiation of the laboratory. By this method, the background in the GP counter is decreased drastically as all external events must have triggered a signal in the guard counter as well and these signals are then discarded. So the anti-coincident counts are the relevant events to count and to subtract background measurements from.

The old setup had an analog readout, where all pulses exceeding a certain trigger voltage were defined as an event. Events occurring simultaneously in the guard counter and one GP counter were stored as coincident events and those only occurring in a GP counter as anti-coincident events. The software copied these two numbers every 5 minute and deleted the storage of the counting box. A ^{14}C activity of a sample was then derived by simply subtracting the anti-coincidence counts of a ^{14}C free counting gas from those of a sample.

While the old counting software only registered events, the idea for the new electronics is to monitor the shape of all signals with very high resolution of up to 10 MS s^{-1} (mega samples per second, so a time resolution of 100 ns) and to evaluate coincident and anti-coincident counts on the PC. The main

advantages of this development is, that an individual trigger level can be set for each counter, increasing its efficiency. Furthermore, by monitoring the peak height and shapes of anti-coincident counts, more sophisticated evaluation methods can be used to discard events not coming from ^{85}Kr decay, such as a rise-time analysis of the peaks or analyzing the β-spectrum of the ^{85}Kr decay.

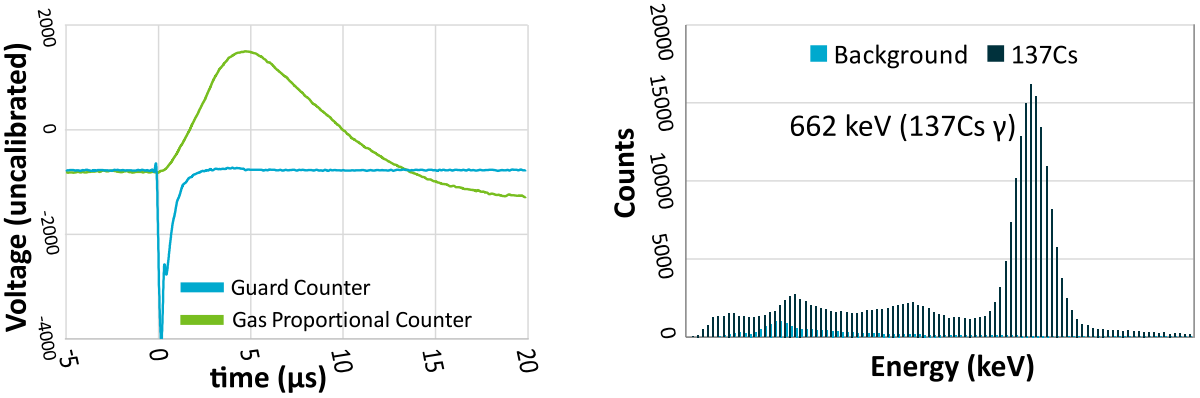

Figure 3.12.: Left: A coincidence peak detected with the newly written LabView software. The GP signal is about 15 μs long while the guard counter time resolution is much better with only 2 μs. Right: The energy spectrum of the 1 MBq ^{137}CS source with its destinct γ line after 5 minutes of counting.

The first tests of the counters and of a first version of the software (mainly written by a colleague Alec Deslandes) were performed by filling one counter with 3 Bar of pure CO_2 and placing a 1 MBq ^{137}Cs source into one lead chamber. Due to the high activity of the caesium source, 5 minutes of measurement is enough to receive the energy spectrum of ^{137}Cs, seen in Figure 3.12.

^{137}Cs has a half-life of 30.17 years and decays by beta emission mainly to ^{137m}Ba, which is barium-137 in a metastable state. It then decays with a half-life of 153s to the ground state (^{137}Ba) by emitting a gamma ray with an energy of 662 keV. This distinct γ-spike in the energy spectrum of ^{137}Cs makes it a useful element for calibrating radiation-detection equipment. The expected energy spectrum could nicely be measured with the counting setup.

The next steps would have been the testing of the counters with a well known amount of modern krypton, but the 14 month in Australia came to an end this could not be done anymore in the course of this work.

^{85}Kr counters at the BfS in Freiburg

Amongst other analytical methods, the laboratories of the German Federal Office for Radiation Protection (Bundesamt für Strahlenschutz, BfS) operates a decay counting setup for ^{85}Kr and ^{133}Xe analysis (Schlosser et al., 2016). As described in subsection 3.1.3, the atmospheric samples taken at the CSIRO for a ^{85}Kr data set of the southern hemisphere were measured at the BfS.

Once the 5 L samples, containing around 2 to 6 mL krypton arrive at the BFS, the gas is further purified by a combination of cryogenic distillation on activated charcoal and by gas chromatographical separation of krypton and xenon. The purified krypton is then filled into one of seven gas proportional counters (GPs), each with an inner volume of 230 mL. Methane is used as carrier gas during the purification and as counting gas for the GPs. For anti-coincidence measurement, NaI szintillators are used and the entire setup is shielded with 10 cm of lead to lower background radiation, which is about 2 to 3 cpm (counts per minute). With a typical sample size of 1-4 mL of krypton, 25-100 cpm are expected in a modern sample and the sample has to be counted < 1 h for a statistical error of < 2 %. The detection limit is 8 mBq/m^3 which is less than 1 % of the current atmospheric activity concentration of ^{85}Kr.

To determine the ^{85}Kr activity of the sample, it is crucial to know the amount of krypton filled in a GP. This is done by analyzing the gas composition after decay counting with a gas chromatograph and comparing it to a known standard with similar gas composition.

The Low-Level counting laboratory in Bern

As the technique of decay counting with proportional counters is now sufficiently described, it will only be focused on the distinctive features of the Low-Level counting (LLC) laboratory at the department of *Climate and Environmental Physics* at the University of Bern.

As the name states, the key property of LLC is to minimize the radiation background during decay counting. According to Table 3.4, 0.1 cpm can be expected in a modern 1 L argon sample. With a background activity of several cpm, as it is the case for the counting setup at the BfS, the ^{39}Ar signal could not be distinguished from the background at all. In Bern, the goal to maximize the signal to noise ratio was approached by a multitude of measures (Loosli et al., 1980):

- the lab is located 35 m below ground level
- the walls of the laboratory are made out of specially selected low activity concrete
- the used lead comes from old shipwrecks depleted in ^{210}Pb
- the counters are built of radioactively pure materials
- the GPs are filled with high pressures for a better gas amount to surface ratio

With that, the background in the counters could be reduced to 0.03 to 0.12 cpm depending on the size of the counter.

For ^{39}Ar analysis with an measurement accuracy of ~7 %, samples have to be measured for up to 8 weeks depending on the argon amount and tracer age of the sample. For ^{81}Kr however, analysis with LLC is practically impossible, due to its long half-life and low isotopic abundance as calculated at the

beginning of this section. ^{85}Kr however, is easily measured within 3 to 6 days in krypton extracted from 100 to 200 L of water (Collon et al., 2004).

^{39}Ar analysis with LLC has been done for ocean and even ice samples in the 1970s and 80s (Rodriguez, 1993; Loosli, 1983). However, since that required a tremendous effort, thereafter it has mainly been applied to groundwater.

4. Groundwater study on Rottnest Island

In May 2016, a groundwater field campaign was conducted on Rottnest Island, 20 km off the coast of Perth, in Western Australia. The study was a collaboration between the CSIRO and the *Australian Nuclear Science and Technology Organization* (ANSTO). Eliza Bryan, a former PhD student at ANSTO, investigated the islands groundwater regime already during two campaigns in 2014 and 2015 (Bryan, Meredith, Baker, Post, et al., 2016). The main goal of this field campaign was to close gaps in the knowledge of the groundwater dynamics on Rottnest Island by applying the tracers ^{39}Ar and ^{85}Kr.

4.1. Environmental setting and former studies

The following information is mainly a summary of Bryan, Meredith, Baker, Post, et al. (2016). The paper is highly recommended for more detailed information on the geological and hydrological setting of the island.

Rottnest Island is a small, sandy and beautiful island in the south west of Australia. It is a famous holiday destination and during peak season, the 300 inhabitants are overrun by daily up to 15,000 tourists, which increases the demand for freshwater drastically.

The island is 19 km^2 in area, has a maximum elevation of 46 m and is built from aeolianite limestone. Its groundwater system is a fresh water lens in the western part of the island, that is floating on top of seawater as illustrated in Figure 4.1. An intermediate water body is between the fresh water and the seawater, which will be called the mixing zone. It can be characterized by total dissolved salt (TDS) values between 1000 mg/L and 35,000 mg/L (Barlow, 2003).

From 1977 on, production wells have been installed in the center of the freshwater lens, to fulfill the freshwater demand of the inhabitants and visitors. In 1995, a desalination plant has been constructed, which today supplies 75 % of the demand for fresh water. Currently, the groundwater abstraction from the lens has been limited to a maximum of 120,000 m^3 per year.

The area of the freshwater lens shrunk drastically during the past decades. Playford et al. (1977) estimated the spacial extension of the lens to be 2.6 km^2 in 1977, while Bryan, Meredith, Baker, Post, et al. (2016) determined the area to be ~1.6 km^2 in 2014. Despite the obvious assumption that the fresh water abstraction is to blame for the reduction, Bryan, Meredith, Baker, Post, et al. (2016) analyzed rain records of the past century and identified a strong decline in rainfall as the main reason for the

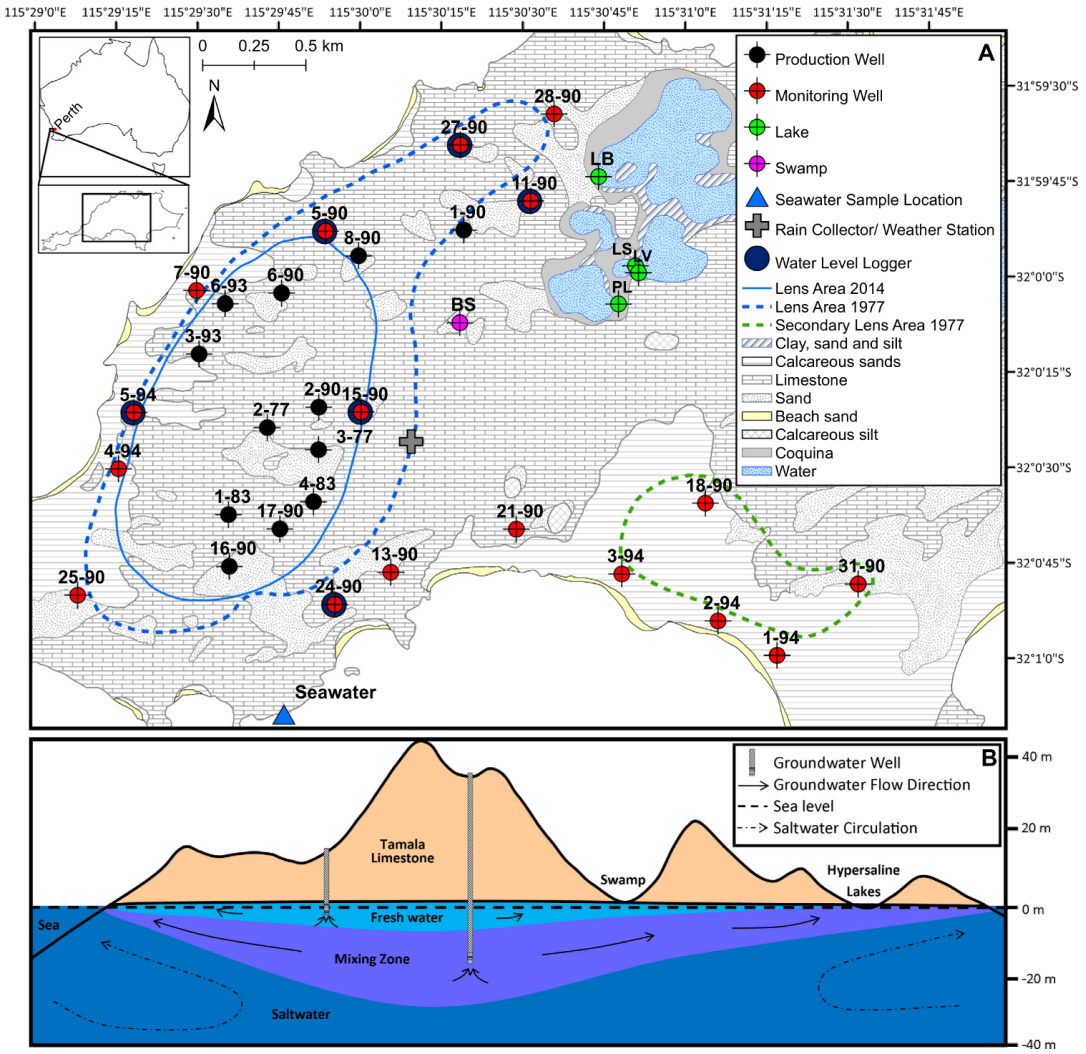

Figure 4.1.: A: The map of the study area in the western part of Rottnest Island. Production wells are marked in red and monitoring wells in black. The blue dashed line indicates the dimensions of the major fresh water lens in 1977, while the solid line represents the size of that lense in 2014. B: A schematic cross-section through the island, illustrating the division in saline, brackish and fresh water (Bryan, Meredith, Baker, Post, et al., 2016).

shrinking of the lens. Estimates of the current annual recharge to the lens vary between 235,000 m^3 and 428,160 m^3 for the very dry year 2014, while the average fresh water abstraction from the lens was on average 33,000 m^3/yr since 2005. Hence, the abstraction is less than 10 % of the annual recharge.

In the early 90s, monitoring wells have been installed, surrounding the center of the lens with its field of production wells, to monitor the further shrinking of the lens by measuring the increase in TDS.

Various tracers have been used during the two former field trips in 2014 and 2015. All 29 wells drawn in Figure 4.1 were sampled, as well as one swamp, four lake and one ocean sample. In the field, the groundwater levels have been measured as well as pH, temperature, electronic conductivity and

dissolved oxygen. Samples have been taken for tritium dating, stable water isotopes analysis (^{18}O and ^{2}H) and for the chemical analysis of the mineral composition of the water.

Several conclusions were derived from the evaluation of the sampled data. The annual recharge was estimated by three different approaches: Via the water balance, a chloride mass balance approach and with the tritium data.

The water balance calculates the recharge rate (R) by simply subtracting the evapotranspiration rate (ET) and a potential runoff rate (Ro) from the precipitation (P):

$$R = P - ET - Ro \qquad \left[\frac{\text{mm}}{\text{year}}\right] \tag{4.1}$$

Runoff is neglected due to the absence of water courses on the island and the evapotranspiration rate for that region was provided by the Bureau of Meteorology (Rottnest Island Station Number 9193).

The assumption for the chloride mass balance is, that all chloride in the aquifer originates from the rain. The chloride dissolved in the precipitation that evaporated again, remains on the ground and is flushed into the aquifer with the infiltrating rain. Hence, the recharge can be calculated by (Appelo et al., 2004):

$$R = P \cdot \frac{Cl^-_{\text{P}}}{Cl^-_{\text{Gw}}} \tag{4.2}$$

with: Cl^-_{P} : Chloride concentration in precipitation
Cl^-_{Gw} : Chloride concentration in the groundwater

The concentration difference is due to evapotranspiration and with that, it is equivalent to Equation 4.1, but without requiring an estimate of the actual value for the ET. The problems with this approach are, that all other sources and sinks for chloride are neglected and that chloride must not accumulate in the groundwater or be filtered out by the vegetation.

The third approach to estimate a recharge rate is based on the tritium concentration measured in the freshwater lens. Assuming the current tritium concentration of the lens is a result of a fixed amount of rainwater that is yearly added, the rate of freshly added rainwater can be derived from the tritium concentrations of past rainwater assuming a well mixed reservoir. It basically assumes an exponential model for the lens. The renewal rate is directly proportional to the recharge as long as the freshwater volume is known. This is simply the thickness and area of the freshwater lens, multiplied by the porosity.

These three methods lead to an estimated annual recharge rate of between 32 % to 59 % of the annual precipitation, which was for the year 2014, between 235,000 m^3 and 428,160 m^3. The ^{18}O and ^{2}H measurements were all in good agreement with the local meteoric waterline of Perth, indicating that rainwater is the sole origin of the freshwater on Rottnest island. The size of the lens was derived from the TDS values of the samples taken from the monitoring wells and was determined to 1.6 km^2, with

an average thickness of ~10 m.

Tritium was the only age tracer applied in this study and was measured only for half of the wells. In addition to that, the tritium values were close or below the detection limit for many samples, especially for the deeper ones lying further away from the center of the lens. The TDS values clearly indicate salt water intrusions into formerly fresh water regions. Still, the origin and history of these saltier waters is not yet understood. They possibly originate from modern seawater, older seawater or the hyper saline lakes. The further investigation of possible end-members of these waters, requires a tracer that can resolve time-scales past the 60 years limit of tritium. Furthermore, additional young tracers can be applied to cross-check the tritium data.

Therefore, a set of additional tracers was used in the field campaign in 2016, that was conducted in the context of this thesis and will be presented in the following. The study was mainly focusing on ^{39}Ar and ^{85}Kr, while samples for ^{14}C, CFCs, Halon-1301, tritium, SF_6 and stable noble gases were taken as well.

4.2. The sampling

The initial goal was, to sample 10 wells, 5 production wells tapping the freshwater lens and 5 monitoring wells, to analyze the salt water intrusion. Both, ^{39}Ar and ^{85}Kr should be measured in Bern via Low-Level counting, which means, that for one sample about 1000 L of water had to be degassed in the field. As no field gas extraction setup was available in Adelaide, the setup built by Reichel (2013) was shipped from Heidelberg to Adelaide especially for this field trip. In addition to that, a 4 kW three phase generator was bought, to power the membrane pump setup used for the argon and krypton separation setup. Ten gas bottles, each with 10 L of volume, were evacuated and filled with nitrogen as sampling cylinder for the extracted gas.

Compared to that, the sampling effort for the other tracers was marginal, as simple glass bottles (between 155 mL for CFCs and 1 L for SF_6, ^{14}C and tritium) were taken, as well as copper tubes combined with a clamping system, to sample 30 mL of water for the stable noble gas measurement. All equipment was fixed on wooden pallets and shipped to Rottnest Island.

The two type of wells that were sampled are shown in Figure 4.2. The production wells (Figure 4.2d) tapping the fresh water lens had all very shallow screens of maximum 1.7 m beneath the groundwater level. Most of them were set up in the 90s, consisting of submersible pumps permanently installed in concrete bore holes and a pipe setup with a tap for sampling the water. None of the pumps were running in the beginning of the field campaign and they had to be turned on at a control panel next to the pump. The borehole itself was not accessible, only the water tab and the control panel.

The monitoring wells (Figure 4.2a) were just steel tubes, 20 cm in diameter stabilizing the borehole, while the actual well was a plastic tube 4 cm in diameter, with a screen of between 5 m to 15 m below

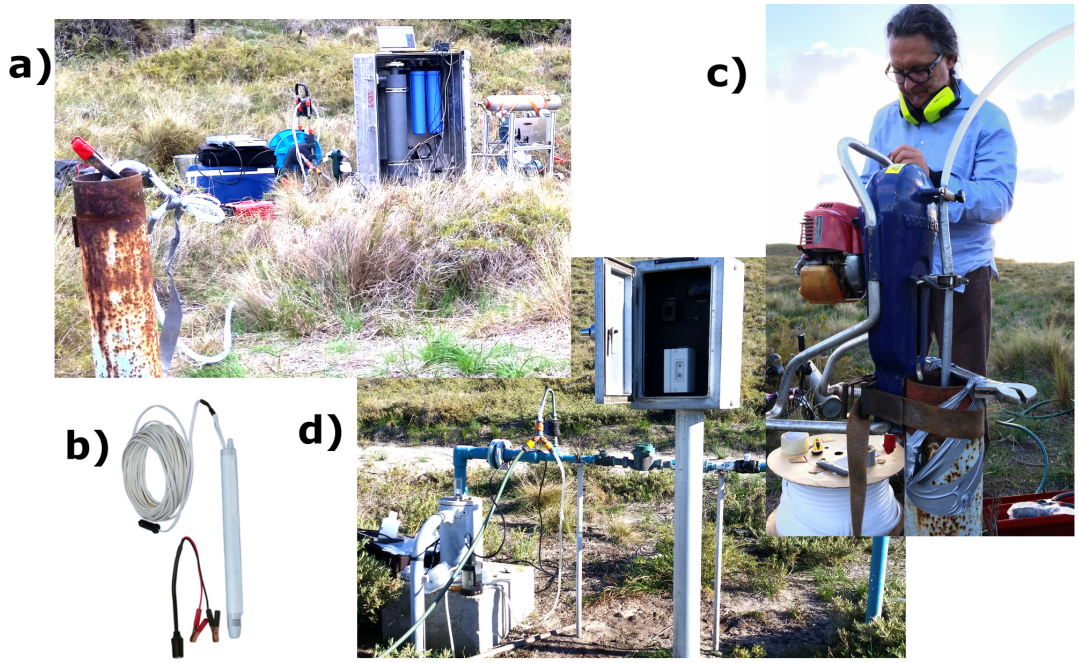

Figure 4.2.: Pictures taken during the sampling. a) A monitoring well is seen in the front and the field gas extraction system and the membrane pumps with the gas sample container on top in seen is the background. b) The *supernova 120* submersible pump used for water abstraction from the monitoring wells. All 9 of these pumps broke during sampling. c) Mounting the footvalve pump shortly before it broke down as well. d) The permanently installed production wells.

the groundwater level. As no pumps were pre-installed in this type of well, the only commercially available submersible pump that fit into the thin hoses was a *supernova 120* pump which is pictured in Figure 4.2b). These pumps have a maximum flow rate of 4 L/min and are powered by a 12 V car battery.

500 mL of argon are required for LLC. Assuming a degassing efficiency of 90 %, an argon purification efficiency of 95 % and an Ostwald solubility of $L = 0.03$ for $T = 20$ °C and $S = 35$ ‰ (Table 2.2) (as a conservative calculation with rather high salinity), yields in a water amount of 1950 L in which ~585 mL argon are dissolved. That means, that the sampling of one sample for ^{39}Ar with a water flow rate of 4 L/min takes about 8 h.

Unfortunately, the submersible pumps were not constructed to run for such long times and one by one they broke down. As soon as the water pump stopped, the water flew backwards through the entire system and atmospheric air got sucked into the membrane contactor and with that, into the sampling container. By the time the ninth pump gave in, only one sample for ^{39}Ar and ^{85}Kr from a monitoring had successfully been taken.

When it became obvious that the submersible pumps won't endure the field campaign, a second type of pump could be organized from Perth, a foot valve pump pictured in Table 2.2c. It is a hose with a

valve at the very bottom, which opens to the inside of the hose when water pushes against it, but closes to the outside so that no water flows back out. This hose is connected to a motor mounted at the top of the well, that moves the hose up and down with ~4 cycles per second and an amplitude of about 15 cm. This way, water is stepwise pushed up due to its inertia of mass.

On day 5 of the 8 days field campaign, the pump arrived and was delivering ~7 L/min water for about two hours, until sparks and metal pieces were flying out of the motor and the pump stopped with a horrible sound. As it was the only pump of this type available in and around Perth and since it was the fifth day of frustrating pump failures, the decision was made to focus on the production wells.

Of the 12 accessible production wells, 2 weren't working 2 were completely dry and 3 wells were only dripping. From the remaining 5 wells, enough gas for ^{85}Kr and ^{39}Ar analysis could be extracted.

The sampling for the other tracers worked without any complications. The bottles for tritium, CFCs and SF_6 were filled by submerging them in a bucket and closing them under water, after three complete bucket volumes have been flushed trough the bottles. The copper tubes were flushed until all air bubbles were gone. Then they were sealed off by closing the clamps at the outlet and the inlet of the tubes.

In terms of sampling for ^{39}Ar, the field campaign failed, as it was not possible to extract enough water with the available pumps. The bore holes were just too thin for a regular MP1 or other well-proven pump types. The 10 L of water that are now sufficient for ^{39}Ar dating with ATTA would have been very easy to extract and 10 monitoring wells could have been sampled easily within 3 days.

4.2.1. Sample preparation

Six wells have been sampled for dating with ^{39}Ar and ^{85}Kr, 5 production wells and 1 monitoring well. The extracted gas amounts varied between 16.5 L and 60 L, depending on the water flow rate of the well, as not more than 3 hours could be spent on a well, in order to finish the field campaign in time. For analysis with LLC, the argon and krypton fraction must be separated and purified with the setup described in subsection 3.2.1. The final purification results are listed in Table 4.1.

The well number refers to the map in Figure 4.3 with a M for monitoring well and a P for production well. 50 μL of krypton are sufficient for ^{85}Kr analysis with LLC, so the purified krypton was split into A and B sample. Four of the six samples have been purified by Alec Deslandes, a colleague at the CSIRO who also did the splitting of the krypton fractions. The chromatogram to the separation of the sample P3-93 is plotted in Figure 3.7 as an example of the separation procedure in subsection 3.2.1.

Except sample P1-83, all final argon purities are above 99 %, yielded argon amounts are higher than 500 mL and with that, are comfortable to measure with LLC. The results for the krypton purification are overall satisfying as well. The total krypton amount is above 100 μL for every sample whereas the purity is lower than hoped for, especially for fraction Kr_1, while fraction Kr_2 is by far purer. This is due to the splitting procedure that worked a bit different for the single gas species, due to their different

Table 4.1.: Results of the purification of the argon and krypton samples for ^{39}Ar and ^{85}Kr analysis with LLC

Sample #	**Extracted gas** [L]	**Ar amount** [mL STP]	**Ar purity** [%]	**Kr_1 amount** [μL STP]	**Kr_1 purity** [%]
M18-90	30.5	669.5	99.5	65.72	89.08
P1-83	16.5	355	98.4	58.23	75.69
P2-77	31.64	590	99.4	69.70	73.90
P2-90	32.33	583	99.6	94.30	69.40
P16-90	60.04	924	99.6	58.03	75.64
P3-93	36.6	694	99.6	80.90	95.10

Sample #	**Kr_2 amount** [μL STP]	**Kr_2 purity** [%]	**Kr_{tot} amount** [μL STP]	**Ar conc.** [%]	**Kr_{tot} conc.** [μL Kr/L gas]
M18-90	91.03	97.22	156.75	2.15	5.14
P1-83	53.58	93.48	111.82	1.86	6.78
P2-77	83.40	70.20	153.10	1.8	4.84
P2-90	71.10	93.70	165.40	1.54	5.12
P16-90	53.86	93.42	111.90	2.2	1.83
P3-93	82.30	97.40	163.20	1.9	4.46

adsorption speed on the activated charcoal.

Astonishing is the very high krypton yield. The samples contained on average about 5 μL of krypton per liter of extracted gas. Taking the Ostwald solubility of Figure 2.11 and calculating the expected krypton concentration for 20 °C and $S = 0$ ‰ yields in 3.74 μL Kr/L gas. When analyzing the gas composition before the separation, it becomes obvious why krypton and as well argon are slightly enriched. Taking sample P3-93 as an example, the gas contains no oxygen anymore, but 2.7 % argon, 1.1 % methane, 11.8 % carbon dioxide and 84.4 % nitrogen. The gas dissolved in air equilibrated water at 20 °C would contain 34.3 % oxygen. All dissolved oxygen was apparently consumed by biological activity and CO_2 or methane, the typical product of this process, were either interacting with the rock matrix and got partly removed, or were not as efficiently degassed by the membrane contactor as the other gases. Hence, all other gases are relatively enriched in the gas sample. Correcting this effect yields in an expected krypton amount of 4.55 μL Kr/L gas, which is very close to the extracted amount of 4.46 μL Kr/L gas of sample P3-93 and results in a recovery rate of 98 % of krypton for that particular sample.

Sample P16-90 however, sticks out as it has a significantly lower krypton and argon yield. The water of that well contained many bubbles during sampling, this is why the 60 L gas could be extracted within less then two hours with an average water flow rate of ~16.6 L/min. The pump might have sucked air and in the further data evaluation it is important to pay attention to a possible contamination of that sample.

The noble gas samples were analyzed with the new noble gas mass spectrometer at the CSIRO in Adelaide. The CFC samples were measured with a commercial gas chromatograph in the laboratories of the CSIRO as well. Tritium and ^{14}C were analyzed at the ANSTO and SF_6 and Halon-1301 were measured at the laboratories of the Department of Hydrogeology in Wellington, New Zealand.

4.3. Data evaluation

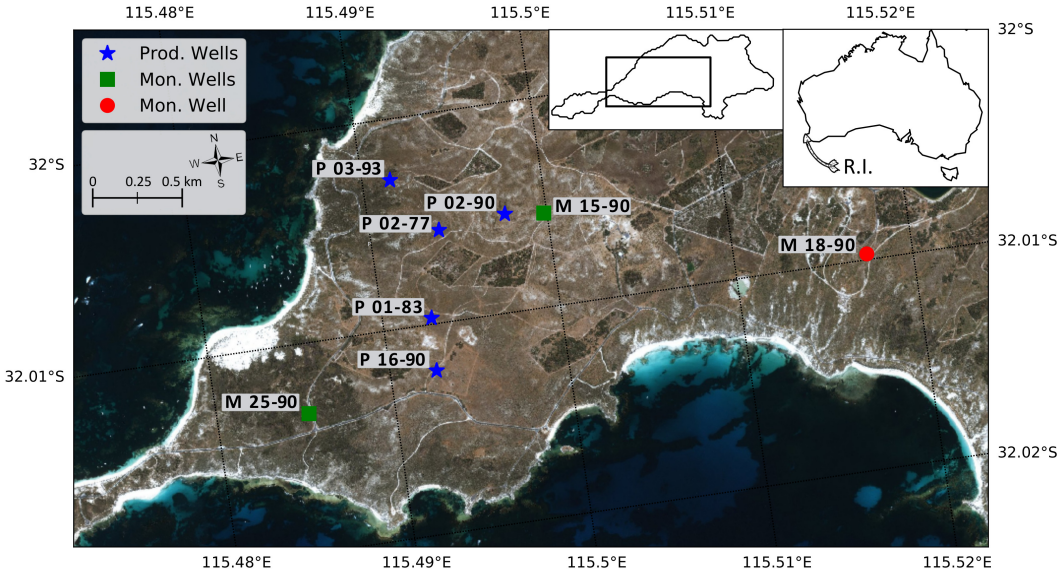

Figure 4.3.: All wells that were sampled during the field campaign. Production wells are indicated with blue stars and the one monitoring well successfully sampled for ^{39}Ar is indicated in red. The sampling for ^{39}Ar and ^{85}Kr failed at the two monitoring wells indicated with a green square. Here only samples for tritium and stable noble gases were taken.

In the end, eight wells were sampled, which are shown in Figure 4.3. Unfortunately, well M18-90, labeled in red, was the only monitoring well of which samples for ^{39}Ar and ^{85}Kr could be extracted. At the two monitoring wells marked in green, all pumps died one after the other as reported earlier. Here, only samples for tritium and for stable noble gases exist. For the one monitoring well and the 5 production wells, which are marked in blue, a complete set of samples for ^{39}Ar, ^{85}Kr, tritium, CFC-11, CFC-12, Halon-1301, stable noble gases, ^{14}C and $\delta^{13}C$ was taken. Of the SF_6 and Halon-1301 samples, the results for only three wells were obtained, as the rest could not be measured. The ^{85}Kr results were delivered within a year, the result of the ^{39}Ar samples have still not been received from the LLC laboratory in Bern. This is on the one hand very unfortunate, as ^{39}Ar was a main reason to do the campaign in the first place. On the other hand, the production wells are expected to be modern in ^{39}Ar and from this one result for the one monitoring well furthest away from the main freshwater lens, not much new insight in the saltwater intrusions is expected. All obtained results are listed in Table A.1 in

the Appendix.

4.3.1. The lumped parameter modeling software

The results of the different tracers are analyzed with a lumped parameter modeling software called *Lumpy*, which was written by Axel Suckow, who is currently working at the Land & Water department of the CSIRO and was the supervisor of this thesis during the stay in Australia. Before applying the software to the Rottnest Island data set, a quick introduction in the programm will be given. A detailed explanation is found in the manual (Suckow, 2014a).

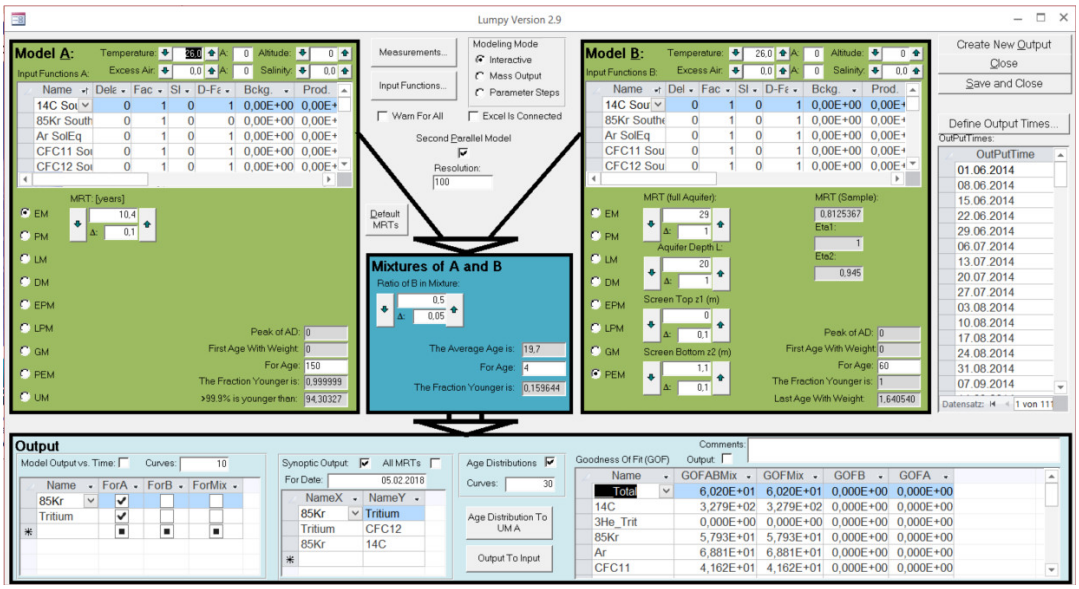

Figure 4.4.: A screenshot of *Lumpy*, the lumped parameter model used for the evaluation of the sample results.

In Figure 4.4 the graphical user interface of Lumpy is displayed. Most functions are relatively self explanatory, as long as the general idea behind the models is clear, which are explained in section 2.3. As a quick reminder, the basic equation lumped parameter models are based on is the convolution integral in Equation 2.19. The overall modeling aim is, to constrain the parameter of a well chosen age distribution G(t') at the location where a water sample is taken. When the atmospheric history ($c_0(t-t')$) of a tracer and its concentration ($c(t)$) in the water sample is known, then the model parameter in the convolution integral are the only free variables. For simpler age distributions, like the piston flow model and the exponential model, the only parameter is the mean age, which can be constrained sufficiently well with only one tracer of the right timescale.

Summing it up, an input function of a tracer is required, the concentration of that tracer in a water sample, and the right age distribution, or transit time distribution (TTD) as it will be called in the evaluation of the ocean samples in chapter 6.

In *Lumpy* , a set of data, the required $c(t)$, is included and selected via the *Measurements* button. The software contains already all atmospheric input functions that are required for the tracers used in the Rottnest Island field campaign and many more, as several tracers, like ^{85}Kr, have a locally varying input function depending on the hemisphere for instance. The infiltration conditions, as altitude, temperature and salinity, are adjusted and with that, $c_0(t - t')$ is given.

Now a model must be chosen. 9 different TTDs are available for modeling, that will not be further explained here, as the only TTDs that will be applied in the course of this chapter are the piston flow model (PM), the exponential model (EM) and the partial exponential model (PEM), which are described in section 2.3.

In general, *Lumpy* is capable of calculating two individual models A and B. This does make sense, when the sampled water is assumed to be a mixing of two distinct water masses with their individual age distribution. The result is a binary mixing of those individually modeled water masses depending on the mixing ratio that can be chosen. There is no reason to assume, that the samples of the freshwater lens are a mixing of water masses with a different distinct age distribution. It could, however, be very true for samples from monitoring wells, as the water in the mixing zone is probably formed out of younger fresh water and older seawater intrusions.

In the lower blue box, the settings for the output are displayed. Different fits will be calculated and plotted depending on what is chosen here. For a data set sampled over several years, it makes sense to plot the *Model Output vs. Time*. The *Synoptic Output* plots two tracer against each other and it is always useful to display the actual *Age Distribution* that is used for modeling the data. How well the model describes the data is indicated by the *Goodness Of Fit (GOF)* value, listed in the lower right corner.

Lumpy is a Microsoft Access database file, using MS Excel as a display interface. For better handling of the calculated data in the course of this chapter, the data was then imported from excel to *python* and plotted with the *Matplotlib* package (Hunter, 2007).

4.3.2. Evaluation of the production well data

Unfortunately, not much new insight could be derived from the samples taken at the monitoring wells. The only age tracer sampled for at all three monitoring wells was tritium and here, the concentrations are close to, or beneath the detection limit. The same applies for ^{85}Kr at well M18-90. Whenever results are present for the monitoring wells, they will be included in the plots, but the focus of the data analysis will be on the production wells.

Choosing the best TTD

Before analyzing tracers with a lumped parameter model, it is essential to pick the type of transit time distribution (TTD) that is best suited to describe the hydrological system. In groundwater hydrology

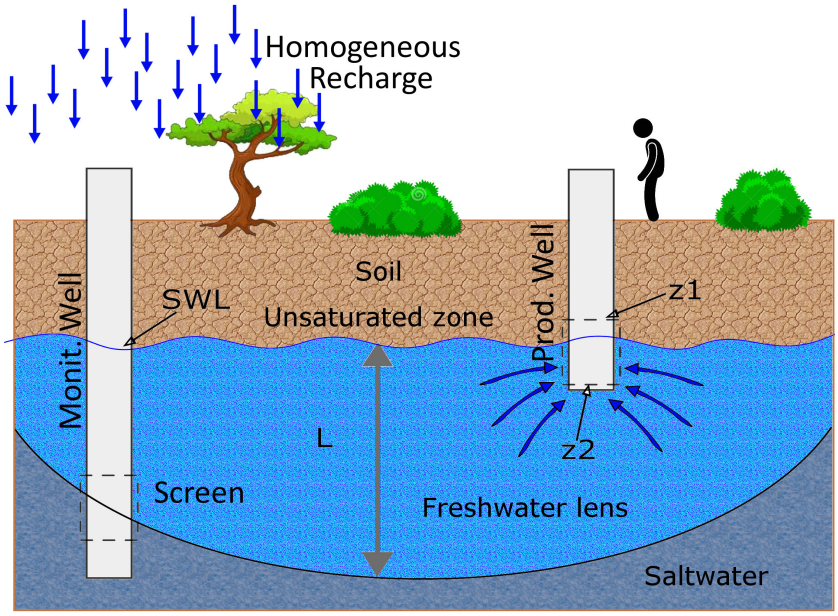

Figure 4.5.: A sketch illustrating the screen depth of the production and monitoring wells. With homogeneous recharge over the entire area of the freshwater lens, it can be described as a Vogel-aquifer.

the term "age distribution" and "mean residence time" is more popular than TTD and mean age but that is just convention. In Figure 4.5 is a sketch of the freshwater lens on Rottnest Island. It is an unconfined aquifer with rain as the only source of recharge, infiltrating homogeneously over the entire area of the lens (Bryan, Meredith, Baker, Post, et al., 2016). The freshwater lens, with a specific average thickness L, floats on top of more saline water. As all 'young' age tracers sampled at the one monitoring well M18-90 during this campaign, and tritium in most other monitoring wells sampled during the two previous field campaigns result in concentrations beneath the detection limit, the water in the saline mix zone can be assumed to contain no water younger than 60 yr.

According to section 2.3, the freshwater lens on Rottnest Island can be described as a Vogel-aquifer (Vogel, 1968) and with that, the age-to-depth relation can be described with an exponential decay function with the constraining parameter τ being the mean age. Thus, the exponential model (EM) would best describe the age distribution of a water sampled from a well with a screen over the entire thickness of the freshwater lens. To be precise, the EM as a theoretical model assumes, that the age of the water goes towards infinity when approaching the bottom of the aquifer. The effect of this assumption on the derived mean ages in the course of this section will be discussed later.

The production wells, which are mainly analyzed here, are characterized by very shallow screens. As seen in Figure 4.2, the production wells were closed off concrete wells and the actual bore hole was not accesible. Hence, the only information on the standing water levels (SWL) - which is basically the groundwater level in an unconfined aquifer, and the screen depth are taken from the archives of the

Table 4.2.: Screen depth and depth of the standing water levels (SWL) in meter Australien Hight Datum (AHD) from the archives of the Rottnest Island Authority. The AHD refers to the height of the mean sea level measured in 1971, which was then defined as 0 m AHD.

Well #	**Ground elevation** m AHD	**SWL** m AHD	**Top of Screen** (z_1) m AHD	**Bottom of Screen** (z_2) m AHD
P02-77	18.7	0.46	0.83	-0.64
P01-83	12.6	0	0.07	-1.33
P02-90	19.3	0.4	0.2	-1.3
P16-90	3	0	-0.2	-1.2
P03-93	19	0.19	0	-1
M18-90	17.54	0.1	-10.77	-11.77
M25-90	11.89	0.31	-5.71	-6.71
M15-90	16.87	0.34	-14.49	-15.49

Rottnest Island Authorities and displayed in Table 4.2. The screen of 2 of the 5 sampled production wells starts above the SWL, while for the other 3 wells it starts 20 cm beneath the SWL. The screen length of the wells varied between 1.40 m and 1.90 m. To prevent confusion: For the further evaluation, the groundwater level is defined as 0 m and the z-axis points downwards.

The setting is best described by the partial exponential model (PEM) (section 2.3). It describes the age distribution of water sampled from a Vogel-aquifer with a screen depth of $0\,\text{m} \leq z_1 \leq z_2 \leq L$, with z_1 being the upper screen level and z_2 the lower screen level. In the following, z_1 is assumed to be 0 m for all sampled production wells, which is justified considering that all wells were purged for some time before the actual sampling and that the 20 cm of initial water column was most likely pumped away.

Hence, the only free parameters that must be chosen to apply the PEM are the aquifer thickness L and the lower screen depth z_2. Reviewing Equation 2.29 and Equation 2.30 on realizes, that it is not z_2 but the depth of z_2 relative to L that is relevant for the TTD of the PEM. Hence, a $z_2 = 2$ m and $L = 10$ m results in the same age distribution as $z_2 = 4$ m and $L = 20$ m when $z_1 = 0$ m.

As indicated in the drawing, taking the real depth of the lower screen level as z_2 might not be the best choice, as it neglects the effects of pumping during the sampling as well as the fact that the wells are frequently abstracting several tons of fresh water during the year. These considerations already now suggest, that the actual hydrological settings are a little bit more complex than assumed by the simple box model applied here. But let the discussion be postponed to after the presentation of the model data.

In Figure 4.6, tritium is plotted against ^{85}Kr. The curves represent the mean age a sample with the corresponding ^{85}Kr and tritium concentration would have, when the hydrological system is correctly represented by the specific model. Three different types of models are plotted here. A piston flow model (PM) in blue, an exponential model (EM) in red, and the partial exponential model (PEM) with different lower screen depth (z_2).

As z_1 is set to zero, the PM and the EM are the limiting case of the PEM for $z_2 = 0$ (PM) and $z_2 =$ L

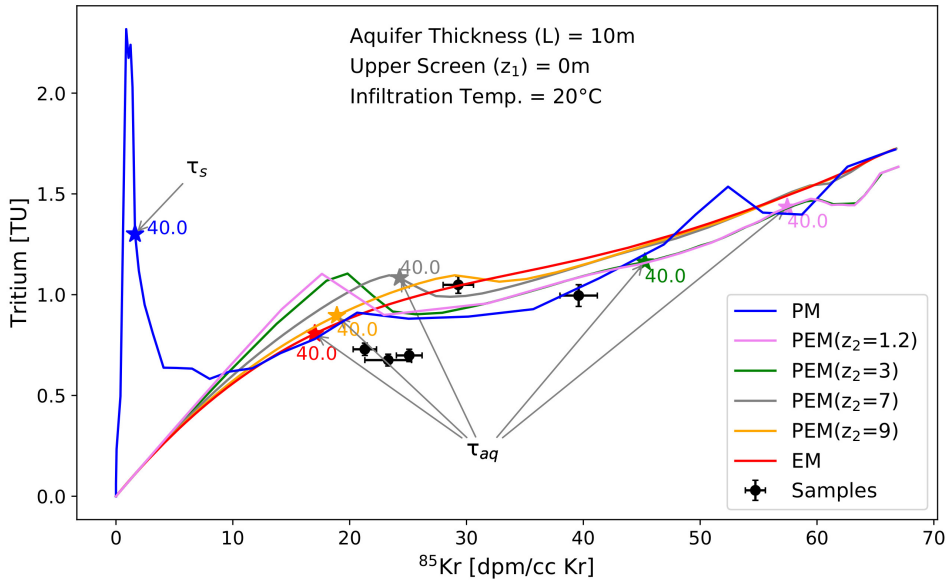

Figure 4.6.: Tritium is plotted against ^{85}Kr. The curves represent the expected concentration of both tracers for a specific mean age calculated with 3 different models, the piston flow model (PM), the exponential model (EM) and the partial exponential (PEM). The PEM is displayed in different variations for different depth of the bottom of the screen (z_2). τ_{aq} is the mean age of the total aquifer while τ_{S} refers to the mean age of the sampled water.

(EM). For the relation between the PM and the PEM it is a bit more complicated, as the PM can never be represented by the PEM as long as z_1 is zero. This becomes clear when looking again at Figure 2.9. It is important to remember, that whenever the mean age is plotted for the PEM, it is the mean age of the total aquifer τ_{aq} while for the PM it is the mean age of the sampled water τ_{S}. For the EM as the limiting case of the PEM, those two are obviously the same.

As an example, the mean age of 40 yr for the specific model is added in the plot. With increasing depth of z_2, the calculated mean ages of the aquifer get younger, as the sample concentration measured at the top of the aquifer represent more and more the total aquifer. Or to put it differently, if the depleted tracer concentrations in the sample represent only the very beginning of the exponential TTD and with that the young fraction of the total aquifer, then the mean age of the entire distribution must be considerably higher.

The black dots are the measured ^{85}Kr and tritium concentrations of the production well samples. If a PEM model is the adequate description of the age distribution of the freshwater lens at the position of the sampled well and ^{85}Kr and tritium reliably represent such an age distribution, then the samples should lie somewhere on the area that is formed from the transition of the PM to the EM by changing z_2 from 0 to L in infinitesimal steps. This way the information of two tracers constrains the ratio of z_2 to L. Although this is only partly true for the transition from the PM to the PEM, due to $z_1 = 0$ as mentioned before.

To check if a tracer combination allows for this approach, the tracers are first plotted and the location of the well data in these synoptic plots in relation to the models is evaluated. A PEM with a screen depth of $z_2 = 3$ m is chosen as a working hypothesis for a best description of the 'true' age distribution of the aquifer. The PM and EM are always included in the plot as the limiting case of the PEM.

Evaluation of stable noble gases

Already on a first glance at the data, one well and three tracers show an unexpected behavior. In the left graph of Figure 4.7, the stable noble gases neon and xenon are plotted, each in mL dissolved gas per L of water, normalized to standard temperature and pressure (T = 0 °C, p = 1013.25 hPa).

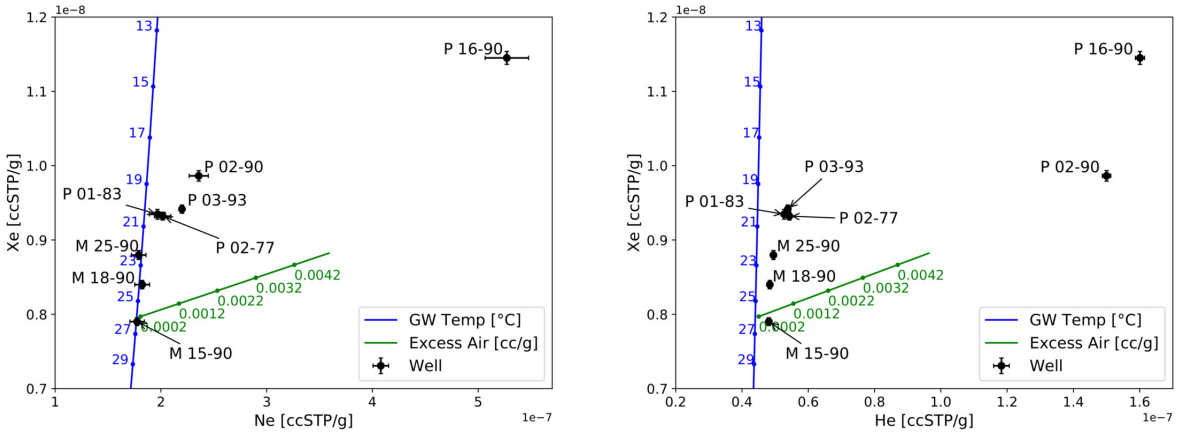

Figure 4.7.: Xenon is plotted against neon in the left graph and against helium in the right graph. The blue line marks the expected equilibrium concentrations for a given infiltration temperature. The green line stands for the influence of Excess Air on the gas concentrations in the water. The sample results are plotted as black dots.

The blue line indicates the solubility equilibrium for a given temperature and the green line the effect of Excess Air. As this is the only time that stable noble gases as a tracer are applied in the context of this thesis, explanations on excess air and noble gas thermometry are kept short and the interested reader is encouraged to further study books like Burnard et al. (2013).

Corresponding to its higher solubility, as pictured in Figure 2.11, xenon concentrations vary strongly with the infiltration temperature (Aeschbach-Hertig et al., 2013). Neon, on the other hand, has a comparably low solublity and thus, is very sensitive to excess air. Excess air is an expression for the phenomenon, that during recharge events, when the groundwater level is temporally rising, air bubbles get trapped in the saturated zone and are then (partly) dissolved due to the slightly higher surrounding pressure. This affects gases with a lower solubility stronger, as the ratio of excess air fraction to the equilibrium fraction is higher.

What is seen in this plot is that all monitoring wells lie well on the equilibration line with infiltration

temperatures between 22 °C and 27 °C, which is higher than the annual mean air temperature of ~20 °C on Rottnest Island (BOM, 2018). All production wells show slightly higher neon values which indicates the presence of excess air. This is reasonable, considering the constant change of the water levels around the wells due to freshwater abstraction. Well P16-90 however, shows a strong increase in neon and also in xenon, This is a strong hint for atmospheric contamination of the sample. As written earlier, this is the sample that was suspicious already during sampling and showed significantly lower argon and krypton concentrations during sample preparation.

In the right graph in Figure 4.7, the xenon versus helium concentration are plotted. As the solubility of helium is even lower than that of neon, the most likely contaminated sample P16-90 has a He concentration by a factor of 4 higher than air equilibrated water would have. The reason why usually not helium is used to evaluate the influence of Excess Air on a groundwater sample is, that there are subsurface processes that alter the helium concentration as well. As already discussed in section 2.2, ^{4}He is a product of the uranium-thorium decay and with that, high helium concentrations in aquifers is an indicator for older groundwater.

The slight increase of helium in the samples of the monitoring well might be due to this effect. It is however unlikely, that the high helium concentration of sample P02-90 is an indicator for the age of the sampled water here. As seen later, the sample does not show any other sign of admixture of older water and as it does not stick out in the Ne-Xe plot, the high He values here are hard to comprehend. In this case it is recommendable to measure a B sample, which could not been done yet, due to technical problems of the mass spectrometer at the Institute of Environmental Physics in Heidelberg.

Two conclusions are drawn from the stable noble gas data. First, the tracer results of well P16-90 will not be reliable, so the further evaluation will focus on the remaining 4 production wells. Second, the Excess Air component in *Lumpy* will be set to 5 cc/g for modeling the tracer results.

Evaluation of SF_6

In Figure 4.8, the SF_6 concentrations of the three measured samples are plotted. The left graph shows the input function. This illustrates the maximum concentrations that can be expected, as no mixing is included. In the right plot, SF_6 is plotted against Halon-1301. The PM, EM and PEM curves are almost not distinguishable, as the SF_6 concentrations are much too high for 'normal' groundwater samples.

The two obvious explanations for these high concentrations are either atmospheric contamination or subsurface production. In general, a third possibility is that the wrong infiltration conditions were chosen. Higher SF_6 model results would be calculated if either a lower infiltration temperature was chosen, or the the excess air component is raised. Because of its low solubility which is highly temperature dependent, SF_6 is very sensitive to excess air and temperature changes. However, model runs showed that an excess air component of > 50cc/kg and a temperature of < 5 °C must be chosen to

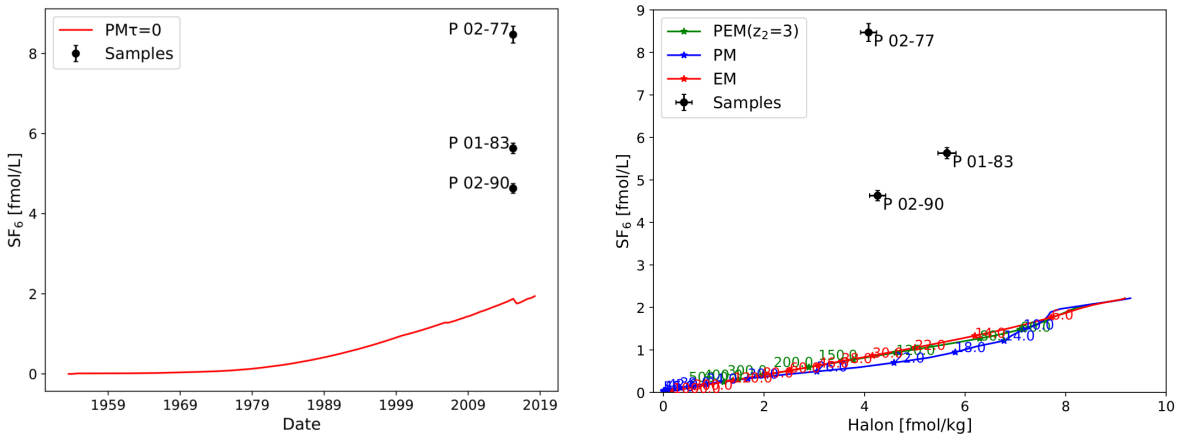

Figure 4.8.: The left graph shows the expected SF_6 concentrations in water over the past 60 years and the measured samples in relation. On the right, SF_6 is plotted against Halon-1301 for the PM, EM and PEM model.

fit the measured SF_6 concentrations, which are unrealistic conditions on Rottnest Island.

Without any additional information, an atmospheric contamination of the samples, either during sampling or during analysis, would be the most obvious explanation. However, Halon-1301 and SF_6 are measured on the same sample and as seen in the right plot, no sign for contamination is found for Halon-1301. In early studies with Halon-1301, the tracer has proven well to identify contamination of a well with SF_6 through underground production, which is maybe the case here (Beyer et al., 2017).

Subsurface production of SF_6 is a common phenomenon in groundwater studies. Busenberg et al. (2000) investigated 16 different mineral and rocks of igneous metamorphic, hydrothermal and sedimentary origin and found values significantly higher than the equilibrium concentration with modern air. Mostly, these high values were found in relation to geothermal or volcanic activity, but subsurface production was observed in carbonate aquifers in different studies as well (Katz et al., 2001).

The consequence is that SF_6 results can not be used for the further evaluation.

Evaluation of CFC-11

In the right plot of Figure 4.9, CFC-11 is plotted against CFC-12. As the tracers have a very similar input function, the models don't deviate much. Considering this fact, it is all the more surprising that the measured concentrations are not represented by any model. As both tracers are measured on the same sample, atmospheric contamination can be excluded as an explanation as it would affect both tracers and would lead to a stronger relative increase in CFC-11 due to its ~4 times lower solubility (calculated for $T = 20\,°C$ and $S = 0\,‰$, after Plummer et al. (2006)), similar to the Excess Air effect for stable noble gases.

Hence, the only reasonable explanation for this effect is, that CFC-11 is degraded in the subsurface by

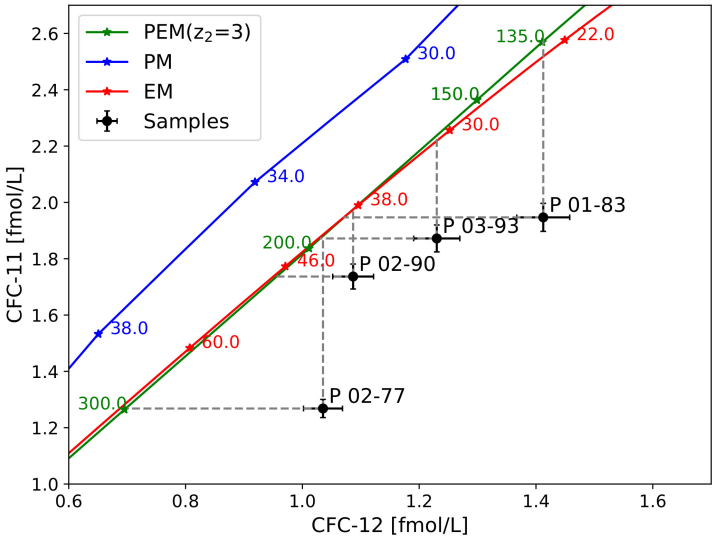

Figure 4.9.: CFC-11 is plotted against CFC-12, including the expected outcome for the PM, EM and PEM model.

microbial activity. This usually happens under anoxic conditions and, as listed in Table A.1, oxygen is indeed depleted in the production wells to various degrees. Unfortunately, degradation affects all CFCs. In a systematic investigation of different environments Oster et al. (1996) calculate a ~10 times faster degradation of CFC-11 than of CFC-12 in anoxic groundwater. This leads to a systematic overestimation of the modeled mean ages derived from CFC-11 as well as CFC-12. Still, as the effect is expected to be an order of magnitude stronger for CFC-11, that tracer is not used for the further evaluation.

Evaluation of ^{14}C

In the plot on the left side of Figure 4.10, the ^{14}C and δ^{13}C values are evaluated and on the right side, ^{14}C is plotted against ^{85}Kr. Focusing on the right plot first, it is obvious that the ^{14}C values are much too low to represent the true mean age of the aquifer or the samples. As written in subsection 2.2.3, ^{14}C is often diluted with old ^{14}C dead carbon, which is clearly the case here. A way to quantify this dilution is to relate the ^{14}C concentrations to the δ^{13}C values, which is done in the plot on the left side of the figure.

The idea is, that the dissolved inorganic carbon (DIC) that is extracted for the ^{14}C measurement of these samples is a binary mixture of two components, the carbon in the soil air, and the carbon washed out of the calcite of the limestone the island consists of. The latter are typically marine carbonates which have a δ^{13}C value and a ^{14}C concentration of zero.

As explained in the subsection 2.2.3, the standard used for δ^{13}C is VPDB, an artificial standard based on the δ^{13} signature of the shell of a marine fossil. As the islands carbonates basically consist out of those shells, they can be assumed to have a δ^{13}C value of 0 ‰. As the limestone was formed millions

of years ago, all ^{14}C is decayed so the one end-member of the marine carbonates of the island is located at (0/0).

The end-member for freshly formed groundwater is mainly given by the ^{14}C and $\delta^{13}C$ signature of the soil air. ^{14}C here can be assumed to be 100 pmC, as all contribution to the CO_2 at this stage originates directly or indirectly from the atmosphere. Fractionation processes caused by plant activity are corrected for via the $\delta^{13}C$ value.

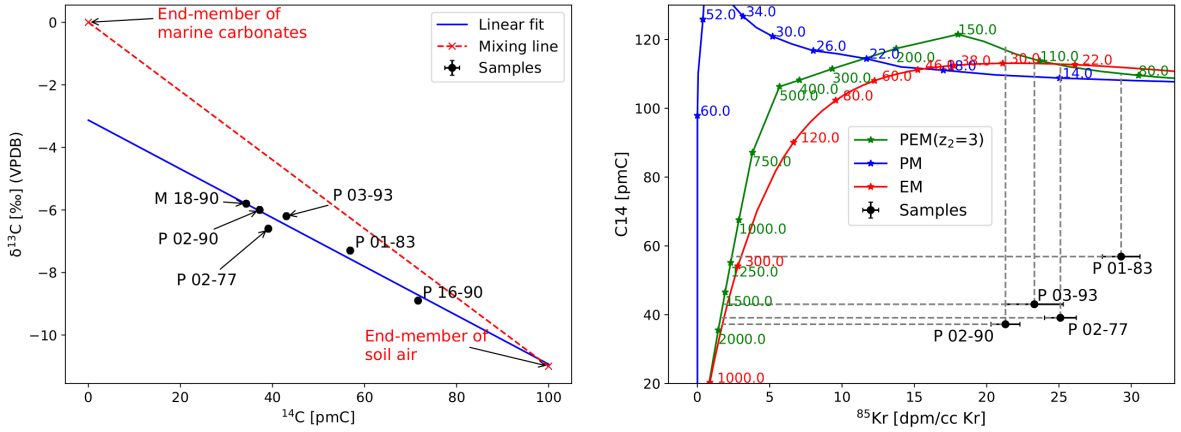

Figure 4.10.: On the left, $\delta^{13}C$ in per mil is plotted against ^{14}C in percent modern carbon. The dashed red line indicates the expected dilution with old carbon. On the right side, ^{14}C is plotted against ^{85}Kr.

The $\delta^{13}C$ itself is a product of different chemical and biological processes (Clark et al., 1997). The CO_2 concentration in the soil air is typically by a factor of 10 to 100 times enriched compared to the atmospheric concentration. The subsurface production of CO_2 is often called soil respiration and comprises the respiration of plant roots, of microbes and microorganisms. The first two contribute the most and the $\delta^{13}C$ signature of the CO_2 released by these processes is that of the plant material. Either because it is decomposed by the microbes or respired by the roots directly. The $\delta^{13}C$ values depend on the photosynthesis pathway the plant is using and after which plants can be categorized in C^3, or C^4 plants with an average $\delta^{13}C$ value of -27 ‰ (C^4) and -12.5 ‰ (C^3). The atmospheric CO_2 has a typical $\delta^{13}C$ value of -7 ‰. The gradient between soil air and atmosphere leads to a slight increase of the $\delta^{13}C$ values again.

After this short excursion, a simple shortcut is taken. Bryan, Meredith, Baker, Andersen, et al. (2017) simply took the $\delta^{13}C$ value of the freshest and youngest well (P 2-94 in Figure 4.1) with a value of -11 ‰ as a representative for the $\delta^{13}C$ signature of freshly formed groundwater, which will be done here as well.

The red dashed line in Figure 4.10, left panel is the mixing line between these two components. The lower the ^{14}C value and the higher the $\delta^{13}C$ value, the more diluted the sample is with old carbon. The

end-member of the soil air is well represented with a linear fit through the data, while the slope of that fit is less steep than that of the mixing line. The overall trend however, represents the samples quite well. The more a well tends towards the marine carbonate end-member, the higher is the mean age derived from the models in the right plot. As a consequence of the dilution, ^{14}C can not be used as a dating tracer for the further evaluation.

Evaluation of ^{85}Kr, tritium, Halon-1301 and CFC-12

After discarding the three tracers SF_6, CFC-11 and ^{14}C due to their altered concentration by subsurface processes and the well P 16-90 due to atmospheric contamination, four tracers and 4 wells remain for analysis.

In Figure 4.11 all combinations of the four tracers, ^{85}Kr, tritium, Halon-1301 and CFC-12 are plotted. Graph (I) is a zoom in the graph shown in Figure 4.6, again with the three models and the dashed lines indicating the mean age of the tracers derived from the models. For well P01-83 the measured tritium concentration allows for three different aquifer mean ages. The bump in the PEM3 model at τ_{aq} = 135 yr represents the tritium peak in the 1960s and the tritium concentration in the sample of well P01-83 refers to a tracer age of either just before the maximum peak height, just after the peak, or to recently equilibrated water. For the mean age derived from the models, the oldest of all three possible mean ages is taken for that well, as it is closest to the other 3 samples.

Unfortunately, none of the four samples lie on the area between the PM and the EM for constraining the parameter of the PEM model. The ^{85}Kr and tritium concentration in well P01-83 however, can apparently be well described by an EM. This would mean, that the samples taken from that well represent an even mix of water from all depths down to the very bottom of the lens and the mean age of the aquifer, as well as the mean age of the sample would then be ~19 yr. In general, the mean ages derived from the tritium concentrations for the PEM3 scenario are by a factor of about 2 higher than those derived from the ^{85}Kr activity concentrations.

In graph (II), Halon-1301 is plotted against ^{85}Kr. Here the derived mean ages lie much closer together and well P01-83 and P02-90 can at least theoretically be described by a PEM model, although the PEM3 scenario overestimates the mean ages here, as the EM seems to be a better fit for the two tracers in these wells. P02-77 has either a too high ^{85}Kr activity concentration, or a too low Halon-1301 concentration to be described by any version of the PEM. In graph (III), CFC-12 is plotted against ^{85}Kr. Unfortunately, none of the four data points can be represented by a PEM as they lie beneath the EM curve. The mean ages of the aquifer derived from the CFC-12 concentrations for PEM3 are between 50 yr and 100 yr higher than those for ^{85}Kr. In the following plots, the mean ages are not indicated anymore, since they are obviously the same as derived from the other three plots.

Graph (IV) displays the tritium concentration versus the halon concentration. Here again, both tracer

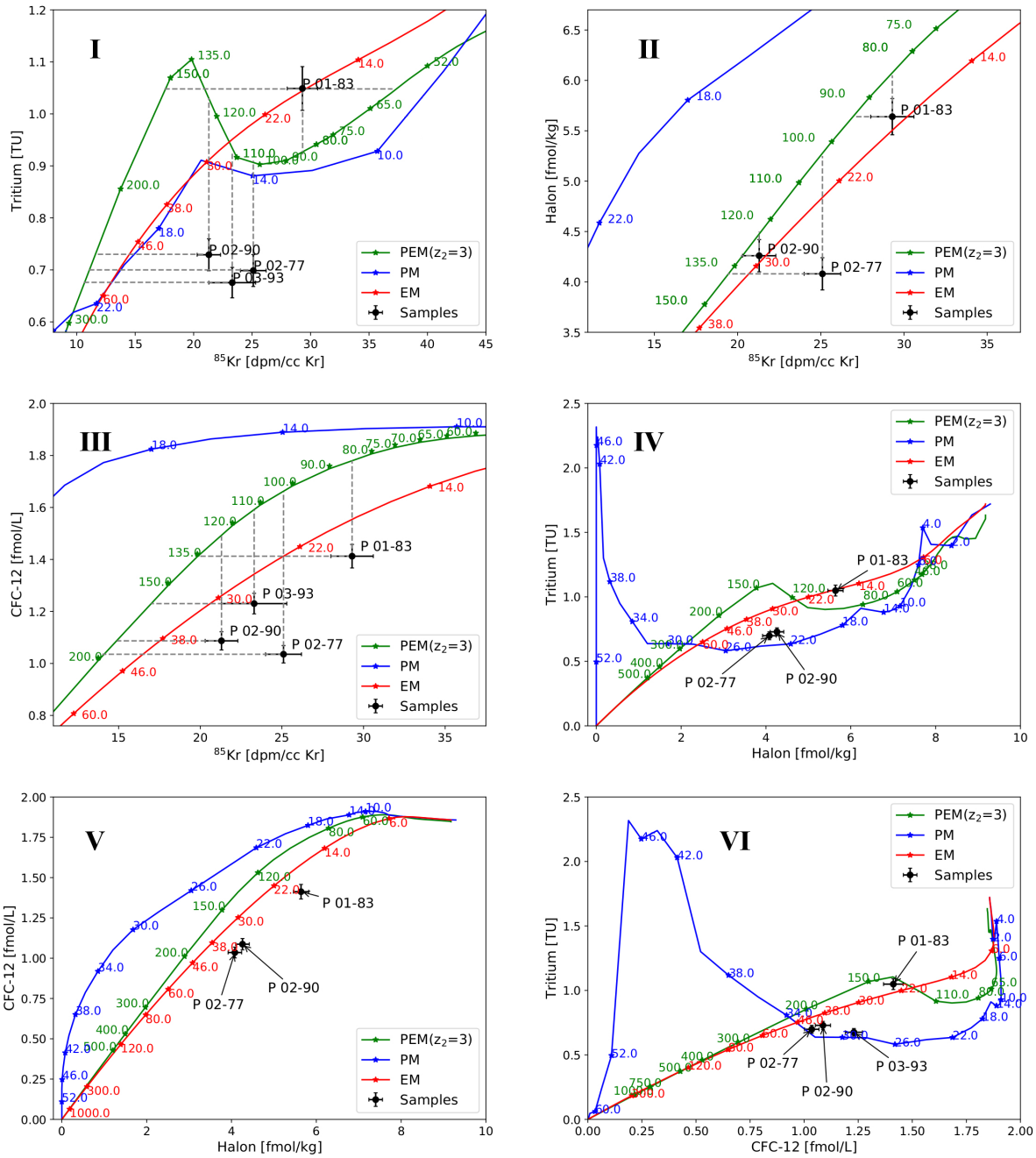

Figure 4.11.: The four tacers ^{85}Kr, tritium, CFC-12 and Halon-1301 are plotted against each other in all six variations. The sample results are indicated as black dots and the possible mean ages for the three different models PM, EM and PEM are written in the color corresponding to the specific model. The gray dashed lines point to the mean age that the specific model calculates for either the tracer on the x-axis or the y-axis.

concentrations can be modeled with an EM for well P01-83, with a mean age of 19 yr. The other two wells seem to lie within the area to be modeled with a PEM by decreasing z_2 to come closer to the PM.

This however, is not possible at this location of the graph. At least not, when z_1 is kept zero. For z_2 approaching zero, not only does the mean age calculated for the entire aquifer tend to infinity, but also only the youngest fraction of the water is taken into account, while it should still represent a tracer age of about 24 yr, according to the PM. The confusing part here is, that all these plots are basically three dimensional plots having the mean age as third parameter, while at the same time comparing the PEM, which models τ_{aq}, and the PM, which represents the tracer age of the sample.

In plot (V), the case is obvious again. All well concentrations are either too high in Halon or too low in CFC-12 to be represented by the PEM. In plot (VI), the well P01-83 can be modeled with a PEM, which is done further below, while the other three wells are again in an area that can not be represented by a PEM.

In Table 4.3, the mean ages for the aquifer derived from the EM and the PEM3 model for the single tracers are listed as well as the tracer age of the samples derived from the PM.

Table 4.3.: Table with mean ages of the freshwater lens for a PEM model with an aquifer thickness of 10 m and a well screen reaching from the groundwater level down to 3 m beneath groundwater level. In the second section the mean ages derived from an EM are listed and in the third section, the sample ages calculated after the PM.

Well	**P02-77**	**P01-83**	**P02-90**	**P03-93**
Aquifer mean ages derived from the PEM [yr]				
^{85}Kr	103±5	85± 5	125±6	111±10
Halon-1301	137± 5	94 ± 4	132± 6	-
CFC-12	195 ± 10	135 ± 6	182 ± 9	158 ±7
Tritium	250±12	158±13	245±12	275±13
Aquifer mean ages derived from the EM [yr]				
^{85}Kr	23±2	19± 2	30±2	28±2
Halon1301	32± 3	18 ± 1	29± 2	-
CFC-12	43 ± 1	23 ± 1	38 ± 1	31 ±1
Tritium	53±3	19±2	48±3	57±3
Sample tracer ages derived from the PM [yr]				
^{85}Kr	14±1	12± 1	16±1	15±1
Halon-1301	23± 0.5	18.5 ± 0.5	23± 0.5	-
CFC-12	34 ± 1	26 ± 1	33 ± 1	29 ±1
Tritium	20±1	6±1	19±1	21±1

Other PEMs

From the evaluation so far, constraining the z_2 to L ratio might work for only two tracer combinations and only for the well P01-83 and P02-90. In the left graph of Figure 4.12, tritium is plotted against CFC-12. As discussed before, the three data points below the EM can't be modeled by a PEM as they are too close to the PM and with that, τ_{aq} is approaching infinity. P16-90 is not worth modeling as

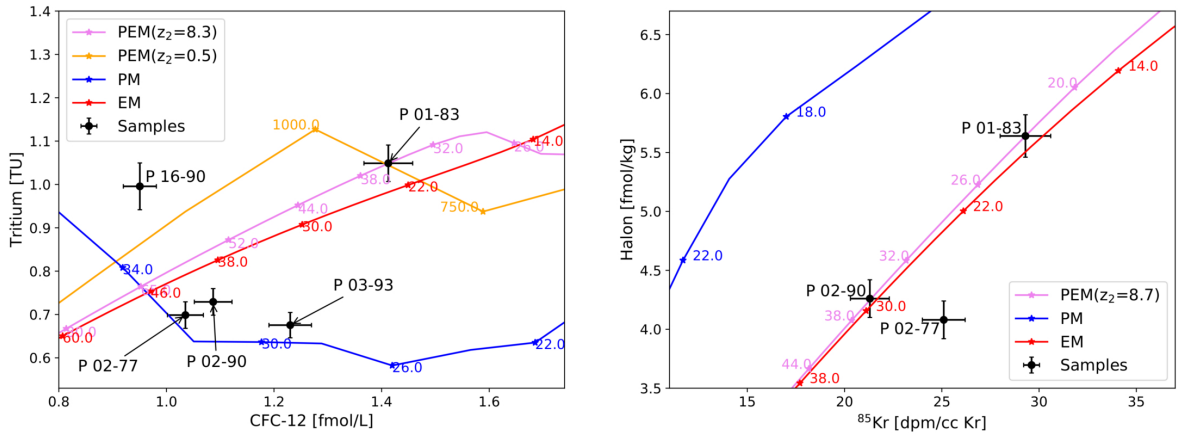

Figure 4.12.: On the left, tritium is plotted against CFC-12. The well P01-83 is fitted with a PEM model resulting in two different mean ages for two different screen depth. On the right, the well P01-83 and P02-90 are fit with a PEM resulting in a bottom screen depth of $z_2 = 8.7$ m.

the sample is contaminated, leaving only P01-83 for this tracer combination. The software found two minima for $z_2 = 8.3$ m with $\tau_{aq} = 36$ yr and $z_2 = 0.5$ m with $\tau_{aq} = 920$ yr.

On the right side of that figure, Halon-1301 is plotted against ^{85}Kr. Here it was obvious that the best fit for the two wells P02-90 and P01-83 is found close to the EM, so with z_2 close to L. *Lumpy* results in $z_2 = 8.7$ m with $\tau_{aq} = 23$ yr for well P02-90 and $\tau_{aq} = 36$ yr for well P01-83.

4.4. Discussion

The data of the 8 wells that were sampled on Rottnest island in May 2016 unfortunately does not tell a consistent story. The further discussion will focus on the production well data, as not enough significant data could be collected from the monitoring wells.

The considerations will be along the following questions:

- Why does the age information derived from the tracers deviate so much?
- What is the best TTD to describe the samples and the aquifer?
- What is the effect of frequent groundwater abstraction on the age distribution of the sampled water?
- What new information is gained from this study? What lesson can be learned?

A few general remarks first: It is quite disappointing, that from the initial plan to sample 10 wells with 8 different dating tracers, the final evaluation shrunk to only 4 production wells with 4 tracers. Then, although the four evaluated wells have a similar screen depth, are located not more than 2 km

apart and all 4 tracers have a similar dating range, the derived mean ages differ in some cases by a factor of 2 between the different tracers.

For all four wells, tritium yields the highest mean ages, followed by CFC-12, than Halon-1301 and the lowest mean ages are derived from ^{85}Kr. All 4 tracers date well P01-83 the youngest, but for the other three wells each tracer gives a different order. In almost all cases, neither the wells for one tracer, nor the tracers for one well result in a mean age consistent with another well or tracer within the error.

While ^{85}Kr, CFC-12 and Halon-1301 are gaseous tracers, tritium is measured on the water molecules. In some field settings this leads to different definitions of a modern sample. While the dating clock is set to zero in the unsaturated zone just above the groundwater level for gaseous tracers, for tritium it is the moment the rain reaches the Earth's surface. Depending on how long it takes for the rain to reach the unsaturated zone, the water 'aged' already in tritium. The time for rain to travel through the unsaturated zone is difficult to approximate as the corresponding equations for water movement through the unsaturated zone are nonlinear partial differential equations (Richard equation) (Assouline, 2013). The infiltration time depends on the hydraulic conductivity, the volumetric water content, the capillary forces and the height difference between ground level and groundwater level. On Rottnest Island, the average distance between ground surface and groundwater level is ~10 meter and limestone has a hydraulic conductivity in the range of 10^{-9} to 10^{-6} m/s (Domenico et al., 1998). Hence, the time for rainwater to reach the freshwater lens should be in the order of months, rather than years.

Another factor leading to different mean ages for different tracers is the uncertainty of the input function. Especially the tritium concentration in rain varies strongly with latitude. In *Lumpy*, the tritium input function measured in New Zealand was taken (Database, 2012). Tadros et al. (2014) evaluated tritium concentrations all over Australia and found significantly lower tritium concentration in rain in Perth, 20 km distance to Rottnest Island than in Hobart, which is on a similar latitude as the station measuring tritium in New Zealand. Hence, Lumpy most likely overestimates the tritium ages on Rottnest Island.

While CFC-12 and Halon-1301 can in general be slightly degraded by the same effects as CFC-11, ^{85}Kr as noble gas is not influenced by any subsurface processes and its southern hemispheric input function is well known (see chapter 5). This makes it the most reliable tracer in this study.

The different models the tracer data was evaluated with, have obviously a major influence on the derived mean ages. *Lumpy* has many other TTDs to model hydrological data with, but all the other models (such as the dispersion model and the Inverse Gaussian distribution applied in chapter 6), assume that no water in equilibrium with the soil air is sampled, which is definitely not the case for the production wells. As the freshwater lens fulfills all characteristics of a Vogel-aquifer, the PEM or EM are the only reasonable models. In some tracer combinations, like Halon-1301 versus ^{85}Kr, the measured concentrations seem to be quite well fit by the exponential model. As it is the limiting case of the PEM, with $z_2 = L$, it might indicate that an effective screen depth much larger than the assumed

3 m is realistic. In other words, that the ratio of z_2 to L must be closer to 1.

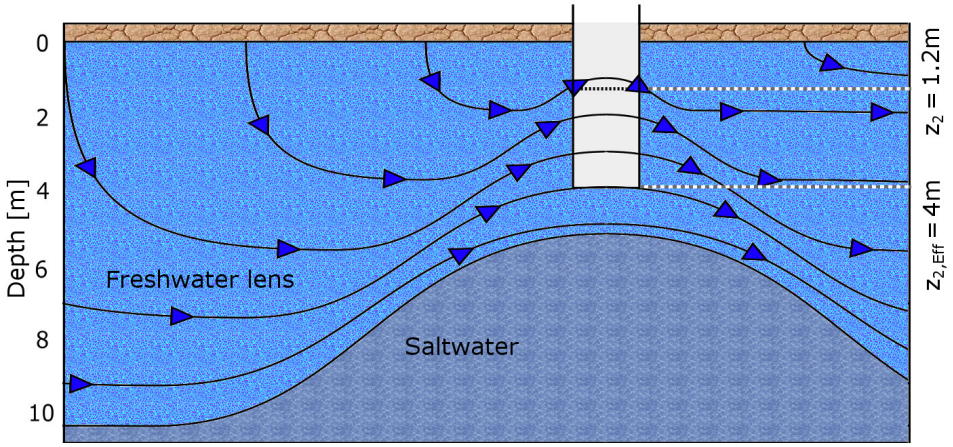

Figure 4.13.: The effect of frequent groundwater abstraction and pumping during sampling on the flow system under a production well is illustrated.

This scenario might be a realistic description, if one not only considers the effect of pumping during sampling, but also the frequent abstraction of groundwater for the freshwater supply of the island. Bryan, Meredith, Baker, Post, et al. (2016) states, that due to their estimates of the annual recharge of the freshwater lens, groundwater abstraction is less than 10 % of the recharge and thus, is not the main reason for the shrinking of the lens. According to their research, the average annual freshwater abstraction since 2005 was 33,000 m^3 per year. As seen in Figure 4.1, only 10 production wells are located in the estimated fresh water lens area. This means, that on average one production well abstracts ~9 m^3 of freshwater daily. That might not influence the overall lens volume much, but surely does influence the local water flow.

Figure 4.13 illustrates a possible effect of the freshwater abstraction. The darker blue color symbolizes the saltier water from the mixed layer. The horizontal dimensions are highly distorted against the vertical dimensions, for the sake of clarity.

The idea is, that through constant pumping, the hydraulic pressure is less in the area beneath the production well, leading to a thinning of the freshwater lens here and allowing the saltier water to rise. The general direction of the freshwater flow, from the center of the freshwater lens to the outside, is not changed (here indicated with blue arrows from left to right). But as the freshwater still floats on top of the more saline water, the flowlines are compressed here. That does not mean that the flow velocity has to rise, as part of the fresh water gets abstracted by the well.

The real depth of the production well screen is of course still 1.3 m (P01-83). When the well is not operated this would still mean, that water from a depth of 2 m in other parts of the lens flows here at the height of the screen. During the sampling, the well was now operated and the hypothesis is, that this pumping 'increases the screen' to the effective screen depth ($z_{2,Eff}$) to for instance 4 m. At this state,

the age distribution of a water sample could be described with a PEM model with $L = 5$ m and $z_2 = 4$ m, which is of course the same as $L = 10$ m and $z_2 = 8$ m, for the undisturbed parts of the lens. This would be quite close to a EM and in good agreement with the results of the two wells P01-83 and P2-90 for Halon-1301versus ^{85}Kr.

A second interesting hypothesis can be drawn from this scenario. The decrease of the effective screen depth from 1.3 m to 4 m does not happen instantaneously. For sampling, the well was purged first until the water had stable conductivity and dissolved oxygen values. Then the sampling for ^{85}Kr and ^{39}Ar was started, which required typically 1 m^3 to 2 m^3 of water. Afterwards the samples for all the other tracers were taken. Assuming that during sampling for ^{85}Kr and ^{39}Ar the effective screen depth dropped to 4 m, it would mean, that the mean age of the water degassed for ^{85}Kr was lower than that for the other tracers, which again is in agreement with the data. Although it still does not explain the difference between tritium, CFC-12 and Halon-1301.

Assuming now the mean age of the aquifer τ_{aq} derived from well P01-83 is a realistic estimate, the annual recharge rate (R) to the lens can be calculated after Equation 2.25:

$$R = \frac{L\Theta}{\tau_{\text{aq}}} \tag{4.3}$$

According to Smith et al. (2012), the porosity Θ on Rottnest Island varies between 0.3 and 0.5. With a lens thickness of $L = 10$ m and the two τ_{aq} of 36 yr, according to the tritium versus CFC12 plot and a τ_{aq} of 23 yr after the Halon-1301 versus ^{85}Kr plot, a recharge of (83 - 130)mm/yr (Θ=0.3) and (138 - 217)mm/yr (Θ=0.5) can be derived. This is a little bit less than the recharge estimated by Bryan, Meredith, Baker, Post, et al. (2016) of (147 - 245)mm/yr, derived from the three approaches described in the beginning of this chapter.

A few general lessons can be learned from this field study. The campaign demonstrates once more how important multi-tracer studies are. Relying only on CFCs, SF_6 or ^{14}C would have gone very wrong in this hydrological system. With just one tracer, one has to trust that it is not affected by any subsurface processes and no atmospheric contamination occurred during sampling. Beside the role to back up information, multiple tracers are essential if more parameters than just the mean age of a simple PM or EM is to be constrained. The PEM is a good example for that and of course when mixing of waters with different histories occurs, as it would have been expected in the mixing zone for the samples of the monitoring wells.

But the biggest lesson learned in this study is, that a required sample size in the order of a ton of water can be a huge obstacle, even in groundwater studies. On the one side, because of the technical requirements, on the other side, because of the influence it has on the investigated hydrological system.

Degassing water in the field is already challenging with a sufficient water flow rate, as the equipment has to be moved all over the island and the whole procedure is more susceptible to errors. But with a

flow rate in the order of 4 L/min and a low gas content, it takes a whole day for a sample, which might not be worth the effort. If then additionally, the water pumps can't cope with the water loads, one ends up with no sample and a lot of frustration.

In a very small and thin aquifer, like the freshwater lens on Rottnest Island, one must not underestimate the effect the sampling itself and water abstraction in general can have on the hydrological system, whose 'natural' state is of interest.

For the aquifer system on Rottnest Island it would be best to not need to sample production wells at all, but to have monitoring wells with screens in different depth in the area of the freshwater lens. Moreover, it would be of great benefit if only a few liters of water were required for analysis, which is the case for most tracers anyway. Luckily, with the advent of ATTA this will soon be the case for ^{39}Ar and ^{85}Kr too.

5. Atmospheric ^{85}Kr concentrations

^{85}Kr can be considered as a purely anthropogenic tracer as its pre-industrial atmospheric concentration lies about 4 orders of magnitude below the current values (Styra et al., 1991). Monitoring the atmospheric concentration of ^{85}Kr is of relevance in several aspects.

Its value as age tracer for groundwater and ocean studies for the past 50 years will increase, as tritium gets less sensitive and SF_6 as well as CFCs become harder to interpret, due to their further decreasing atmospheric concentration. In addition to that, the sampling and analytical effort for ^{85}Kr becomes less with reduced sample sizes thanks to ATTA. Furthermore, ^{85}Kr is used as a tracer to study interhemispheric exchange times and processes close to the Intertropical Convergence Zone(ITCZ) due to its higher concentration on the northern hemisphere (NH) (Bollhöfer et al., 2014). Amongst other isotopes, ^{85}Kr has been proposed as a candidate to monitor compliance with a potential future Fissile Material Cut-off Treaty (FMCT) (Ross et al., 2010).

One remark at this point: In the following, the term "atmospheric ^{85}Kr concentration" is used. Being precise, it should be "atmospheric ^{85}Kr activity concentration in ground level air". Activity concentration, because ^{85}Kr is measured in Bq/m^3 air and ground level air, because that is were the samples were taken. For reasons of consistency within the thesis and better readability, only "concentration" will be used. As for the term "ground level air": the global atmosphere is treated as a simple two box model of northern and southern hemisphere in the course of this chapter and no vertical subdivision is taken into account. As ^{85}Kr is mainly evaluated in regards to its properties as a dating tracer for ice and water, this simplification is justified, as the ground level air equilibrates with surface waters and ice reservoirs.

The main source of ^{85}Kr are nuclear reprocessing plants, of which it is released into the atmosphere once the nuclear fuel rods are dissolved in acid. Other sources are nuclear power plants, which account for ~1 % of all ^{85}Kr emissions, and medical and scientific institutes, whose contributions are negligible. Figure 5.1 shows a map with all existing and operational sites. Currently no reprocessing plants are active on the southern hemisphere (SH).

The global ^{85}Kr budget is calculated from the monitored ^{85}Kr concentrations of stations around the globe and multiplied with the atmospheres volume. With a specific conversion factor depending on the reprocessing technique, the plutonium production in reprocessing plants can be estimated from its ^{85}Kr emissions (Winger et al., 2005; Ahlswede et al., 2013). As seen in figure 5.1, annual emissions steadily

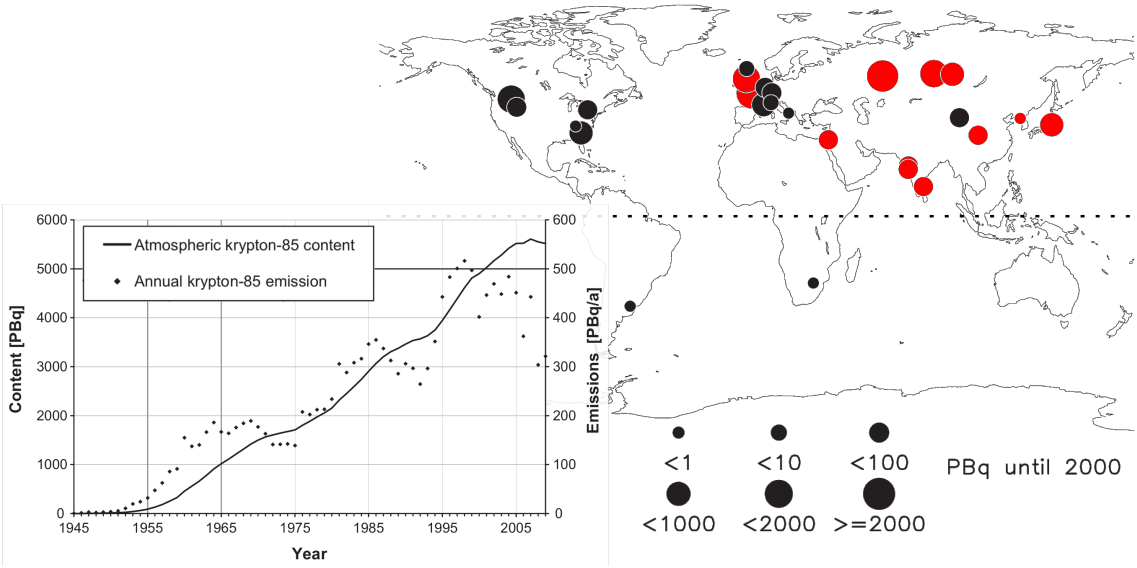

Figure 5.1.: Left: The annual ^{85}Kr emissions and the global ^{85}Kr budget since 1940. Right: Location and ^{85}Kr emissions in PBq of still operational (red) and decommissioned (black) reprocessing facilities after Ahlswede et al. (2013) and Winger et al. (2005).

increased since 1945 and peaked with about 500 PBq/yr in 1999. The global budget, which is the equilibrium of the ^{85}Kr emissions and the radioactive decay, peaks around 2007 with about 5500 PBq. The accuracy of this inventory is estimated to be in the range of a few percent.

One of the observation sites in the northern hemisphere is the monitoring station Schauinsland in southern Germany close to Freiburg. Here, almost weekly samples of atmospheric air for ^{85}Kr analysis have been taken since 1976, representing one of the largest ^{85}Kr data sets of a single station. Before that, 24 samples were measured since 1953, which will be called 'pre-measurement' samples in the course of this section.

In 1983 air sampling for ^{85}Kr analysis was started in Antarctica, making it the first known sampling station on the southern hemisphere. When sampling was stopped in 2008, over 400 samples have been analyzed. Other stations on the southern hemisphere were Cape Grim on Tasmania from 1987 to 1996, Cape Point in South Africa from 1985 till 1997 and Darwin in Australia from 2007 till 2010. All together about 1100 atmospheric ^{85}Kr samples from the southern hemisphere have been analyzed since 2010.

In August 2015 a new sampling station has been set up at the CSIRO in Adelaide, Australia. Up to now 150 samples have been taken and analyzed on a weekly basis, as described in section 3.1 and section 3.3. The new data is taken as a motivation, to reevaluate the complete ^{85}Kr data of the SH in relation to the Schauinsland data set.

5.1. Data evaluation

Figure 5.2 shows the entire data set that is worked with in this section. It comprises all data of the observation sites in Antarctica, Cape Grim, Cape Point, Darwin and Adelaide, which, to the authors knowledge are the only stations on the southern hemisphere ever taking series of atmospheric ^{85}Kr samples. Furthermore, the data set of the Schauinsland station as well as the data of the pre-measurements are included. It would have been very beneficial for the evaluation if data of other monitoring stations in the northern hemisphere were included, unfortunately these stations are very protective with their data.

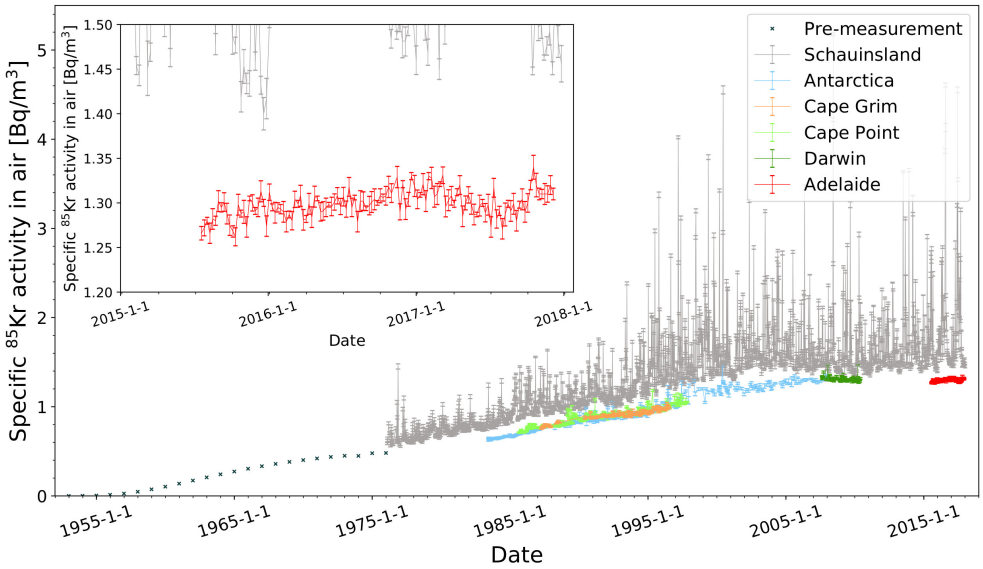

Figure 5.2.: Specific ^{85}Kr activities from samples taken at 6 different observation sites are plotted against time.

One of the most striking characteristics of the Schauinsland data are the spikes with concentrations of up to a factor of 5 higher than an estimated baseline. The most productive and currently only operational reprocessing plants in Europe are Sellafield in the north west of England and La Hague in the north west of France. Depending on the operation mode of the plants and the weather and wind conditions over Europe, highly enriched plumes of ^{85}Kr, emitted mostly from La Hague, cross the south of Germany and are detected at the monitoring station Schauinsland. As the sampling itself takes a week, all values represent an average weekly ^{85}Kr concentration, hence, single emission events of La Hague give a significantly stronger signal (Felsberg et al., 2018).

In the data of southern hemisphere, hardly any spikes are present. The only existing reprocessing plants on the southern hemisphere were Ezeiza, in Argentina, operational in 1989 and 1990 and the plant

Pelindaba in South Africa, online from 1986 till 1992. With an annual emission of ~0.1 PBq of ^{85}Kr, their contribution to the global budget is negligible, considering that the average annual emissions of just La Hague amount to 106 PBq (Winger et al., 2005). The ITCZ hinders a fast equilibration between the hemispheres, hence, air masses crossing the equator from north to south represent rather an average ^{85}Kr concentration of the northern hemisphere.

In the upper left corner of Figure 5.2, a zoom on the data sampled in Adelaide is pictured. The ^{85}Kr concentrations of the weekly taken samples show slight fluctuations around an average of 1.3 Bq/m3 and a mean squared error of 0.015 Bq/m3 . No significant decrease or increase is detectable over more than two years.

Beside the obvious characteristics, the present data set can be further examined in many aspects. As a tracer for ocean, ice or groundwater studies, local or hemispheric related input functions for ^{85}Kr are required and as a tracer for atmospheric circulation, the relation of northern hemispheric to southern hemispheric concentrations are of interest. A deeper analysis will be done along the following considerations:

- What was the average ^{85}Kr concentration on the northern hemisphere during the past 40 years and can it be derived from the Schauinsland data? What does a local or northern hemisphere related input function look like?
- What is the input function on the southern hemisphere?
- What is the interhemispheric exchange time?
- Can the southern hemispheric input function be estimated from the Schauinsland data to bridge data gaps on the southern hemisphere and if yes, with what precision?
- Can an average ^{85}Kr concentration of the northern hemisphere be derived from the southern hemispheric input function to avoid the spikes of the Schauinsland data set?
- How much does the uncertainty of an input function influence ^{85}Kr tracer ages in environmental samples?

All calculations and modeling of the data has been done in *python*.

5.1.1. The Schauinsland data set

When analyzing the Schauinsland data it is obvious, that the locations of monitoring stations in relation to nuclear reprocessing plants as well as weather conditions have a huge impact on the measured ^{85}Kr concentration and that the northern hemisphere can not be approximated as a well mixed reservoir for ^{85}Kr for many areas. Hence, local input functions are required for dating with ^{85}Kr.

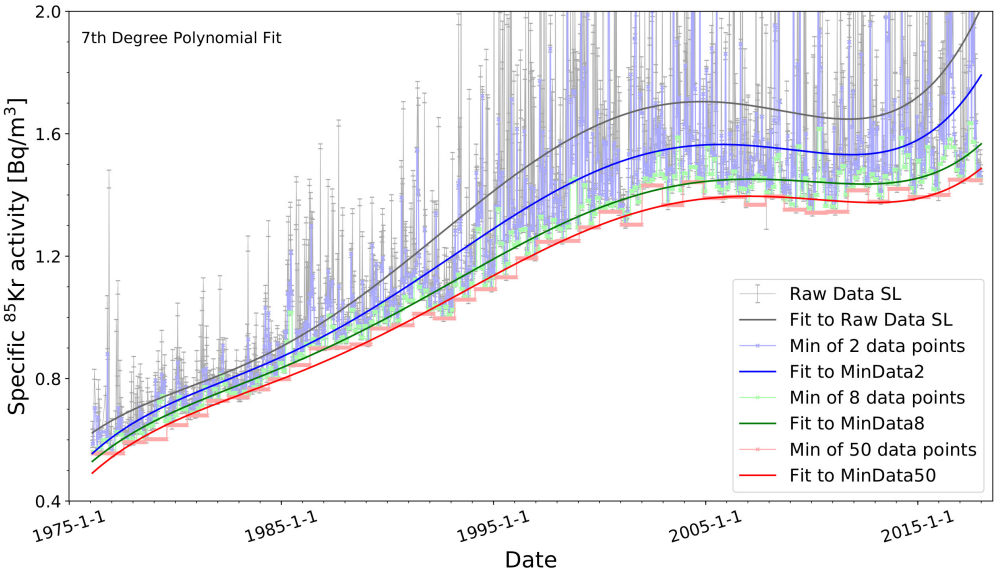

Figure 5.3.: Four 7th degree polynomials are fitted to the Schauinsland data, each to a different scenario in which the minimum of 1, 2, 8 and 50 data points is taken.

In Figure 5.3 the Schauinsland data is plotted, as well as three scenarios in which the minimum of a specific number of data points is taken for all of these data points. A 7th degree polynomial function has been chosen for fitting the data. Polynomials of different degrees and their least square values (as explicated later in this section) are compared in Figure A.4 in the Appendix.

The original Schauinsland data set contains 2127 ^{85}Kr measurements from 1975 till December 2017. Hence, the gray line represents the local input function, for example for groundwater studies with a recharge area near Freiburg. Here, all water infiltrating the ground can be assumed to be in equilibrium with air, having the same ^{85}Kr concentration as the one sampled at the Schauinsland station. Hence, all single emission events of La Hague will infiltrate as well. The ^{85}Kr peaks infiltrating aquifers are then smoothed out by mixing with waters with slightly different recharge times, resulting eventually in averaged activities represented by the gray fit.

This fit obviously does not represent the average ^{85}Kr concentration of the northern hemisphere as the signal is polluted by La Hague and Sellafield. The hypothesis is, that the lower envelope of the plotted data represents the 'true' mean hemispheric value. Therefore the highest values are kicked out by taking only the lowest value of a certain amount of data points. For the light blue values in Figure 5.3, two data points are compared and the value of both is set to the smaller one. The light green and light red data set is generated accordingly but with a comparison of 8 and 50 data points respectively. To each of the three scenarios a 7th degree polynomial is fitted.

With just discarding the highest of two values, the fitted atmospheric ^{85}Kr concentration in January

2005 is lower by 0.15 Bq/m^3 air compared to the fit to the raw data. It decreases by another 0.12 Bq/m^3 air for the minimum of the 8 data points scenario and by another 0.04 Bq/m^3 air for the minimum of the 50 data point scenario. As a data point typically represents one week of sampling, the last scenario reduces the resolution to the minimum of an annual measurement cycle, hence, to 43 different values. This makes the fit vulnerable to single outliers that might occur due to mistakes during sampling or during the measurement. The goodness of the possible scenarios as a candidate for the lower envelope is hard to quantify. One possibility is to compare it to the input function of the southern hemisphere, as the lower envelope might represent the mean northern hemispheric ^{85}Kr concentration and with that, the source for the southern hemispheric concentration under consideration of the interhemispheric exchange time and the radioactive decay.

From a qualitative perspective, the fits for 8 and 50 data points both describe a lower envelope of the data quite well. In the following, the minimum of 30 data points is chosen as the best description for the lower envelope of the Schauinsland data set as a compromise between data point resolution and exclusion of spikes.

5.1.2. Input function of the southern hemisphere and the interhemispheric exchange time

The subdivision in local and southern hemispheric input function is unnecessary, as the emissions of the only two reprocessing plants that were ever operated on the SH are negligible. Thus the samples taken at different sites on the SH can be treated as a true representative of the entire SH at that time. Hence, the division into different monitoring sites is not done anymore and all SH data is treated as one set.

In Figure 5.4 a 7th degree polynomial is fitted to the ^{85}Kr concentration of the SH. While the concentration on the NH was measured weekly, the data collection on the SH is distributed less homogeneously along the time axis. Between 1987 and 1996 three monitoring stations were active resulting in a high density of data points, while between 2010 and 2015 no sampling was done at all. The goodness of the fits is quantified with the chi-square test:

$$\chi^2 = \sum_{\mathrm{i}} \frac{(f(x_{\mathrm{i}}) - y_i)^2}{f(x_i)} \tag{5.1}$$

with: $\mathrm{f}(\mathrm{x}_i)$: value of fit function at position i
y_i : data point i

Python finds the best suited polynomial to fit the southern hemisphere data with the method of least squares as illustrated in Equation 5.3. The fit is constrained strongest by the denser data clouds till 1998 and by the Darwin and Adelaide data. Still, with χ^2 = 1.403 all data is well represented by the fit.

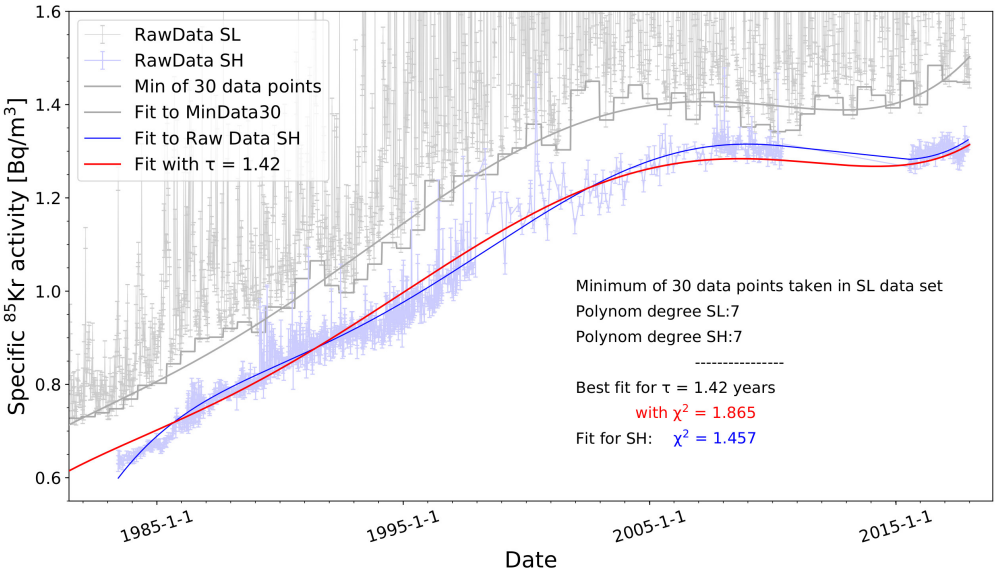

Figure 5.4.: A lower envelope of the Schauinsland data is fitted to the minimum of 30 data points, representing the average ^{85}Kr concentration on the NH. In blue a 7th degree polynomial is fitted to the SH data representing the average ^{85}Kr concentration on the SH. From the two fits the interhemispheric exchange time τ is calculated.

The average ratio of southern hemispheric ^{85}Kr concentration to northern hemispheric concentration is 0.877 ± 0.029, so on average, the ^{85}Kr concentration on the SH is ~13 % lower than the one on the NH (estimated from the Schauinsland data). The error of that ratio is the mean squared error of all single ratios of the lower envelope of the Schauinsland data to the SH data.

Treating each of the hemispheres as one well mixed box, assuming that all ^{85}Kr sources are located on the NH and that the input functions of the ^{85}Kr concentration of both hemispheres are well known, then the concentration difference of the hemispheres is solely determined by the interhemispheric exchange time τ:

$$A_{SH}(t) = A_{NH}(t - \tau) \cdot e^{\tau \cdot \lambda} \tag{5.2}$$

with: $A_{NH/SH}$: ^{85}Kr concentration on NH and SH respectively
λ : ^{85}Kr decay constant of $6.44 \cdot 10^{-2}$ yr^{-1}

The fit of the minimum of 30 data points scenario of the Schauinsland data set is assumed to represent the 'true' ^{85}Kr concentration of the NH. Now the interhemispheric exchange time τ is varied in steps of 0.01 years between 0 and 3 and the best fit is found according to the method of least squares:

$$\min(S(\tau)) = \min \sum_i (f(x_i, \tau) - y_i)^2 \rightarrow \vec{\nabla} S(\tau) = 0 \tag{5.3}$$

The best fit with a χ^2 of 1.872 is found for an interhemispheric exchange time of $\tau = 1.42$ yr. Again, the higher data density in the late 80s early 90s influences the fit stronger, while its shape is now fixed, as it is the shape of the NH input function. This leads to a slight underestimation of the SH data from 2003 on. Still, the extrapolated curve fits remarkably well to the SH data.

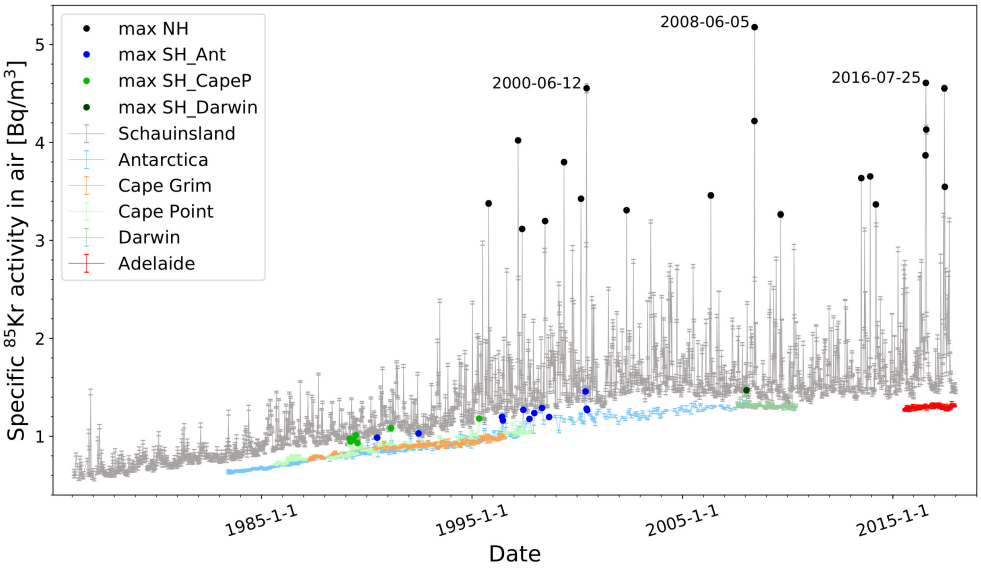

Figure 5.5.: The 20 strongest outliers of the Schauinsland data and the SH data are marked. The ^{85}Kr peaks on the SH seem unrelated to those in the Schauinsland data.

Another possibility to estimate the interhemispheric exchange time is to compare single peaks in the data of the NH and the SH. The idea is, that strong emission events by reprocessing plants on the NH might be detectable on the SH after time τ. In Figure 5.5 the 20 strongest events in the Schauinsland data and on the SH are marked. Unfortunately no significant relation between the peaks in the hemispheres can be observed.

The highest activities measured at Schauinsland are in June 2000, June 2008 and July 2016. None of these events is detectable in the data of the southern hemisphere. Although, assuming an exchange time of more than 17 month, the last event might still occur in the Adelaide data soon. The occasional peaks measured at Cape Point might be related to emissions of the reprocessing plant Pelindaba, which was active during that time in South Africa. 13 of the 20 highest ^{85}Kr activities measured on the SH were detected at the station in the Antarctic. This is astonishing, as it is a station remote from any existing ^{85}Kr sources and furthest away from the ITCZ.

Over the past 50 years, the interhemispheric exchange time has been determined in different studies with different approaches. Values vary between 0.7 yr, derived from simulations with an atmospheric circulation model (Aghedo et al., 2008) and 1.7 yr, calculated from ^{85}Kr concentrations with a two box model of the atmosphere (Levin et al., 1996). A good overview of different interhemispheric exchange time calculations is found in Ross et al. (2010).

The on average longer exchange time derived from ^{85}Kr concentrations might be related to the structure of the atmosphere. Most of the interhemispheric transport takes place in the upper troposphere and as both, sources of ^{85}Kr emissions as well as monitoring stations, are on the ground level on the hemispheres, the time for vertical mixing within a hemisphere must be taken into account.

5.1.3. ^{85}Kr concentration on NH extrapolated from SH data

One could ask, whether any of the measured activities at the Schauinsland station represents the average NH ^{85}Kr concentration at a given time. Since the beginning of sampling at that station in 1976, there were always reprocessing plants operated in Europe. As one data point is the average of a complete week, one could argue that all samples are biased by local emissions to a certain degree. That would result in an overestimation of the interhemispheric exchange time as it was calculated earlier.

The idea here is, that the 'true' mean ^{85}Kr concentration in the NH could be derived from the SH data with a given interhemispheric exchange time. This makes obviously only sense, if a reliable value for the interhemispheric exchange time can be assumed, which is difficult considering the range of different estimates for τ as discussed above. Still, as an experiment an interhemispheric exchange time of 1.1 yr is chosen, as it is the average of τ from 14 different studies listed in Ross et al. (2010). Transforming Equation 5.2 leads to:

$$A_{NH}(t) = \frac{A_{SH}(t+\tau)}{e^{\tau \cdot \lambda}} \tag{5.4}$$

In Figure 5.6 the extrapolated NH concentration is plotted for $\tau = 1.1$ yr. The fit deviates strongly before 1985 which does not reflect any physical processes but is a consequence of the polynomial fit that is only suited to describe the SH data between 1985 and 2017. The extrapolated ^{85}Kr concentrations are on average 2.1 ± 1.8 % below the once from the lower envelope but the fit describes the trend of the Schauinsland data quite well and is in good agreement with the lower envelope from 2005 on.

A comparison with data from other monitoring stations on the NH could generate new insight, especially from stations further away from reprocessing plants.

5.1.4. Consequences for dating with ^{85}Kr

In Figure 5.7 the decay corrected input functions for two scenarios on the NH and two scenarios on the SH are plotted. For the NH the activities of the local input function (fit to the raw data) and

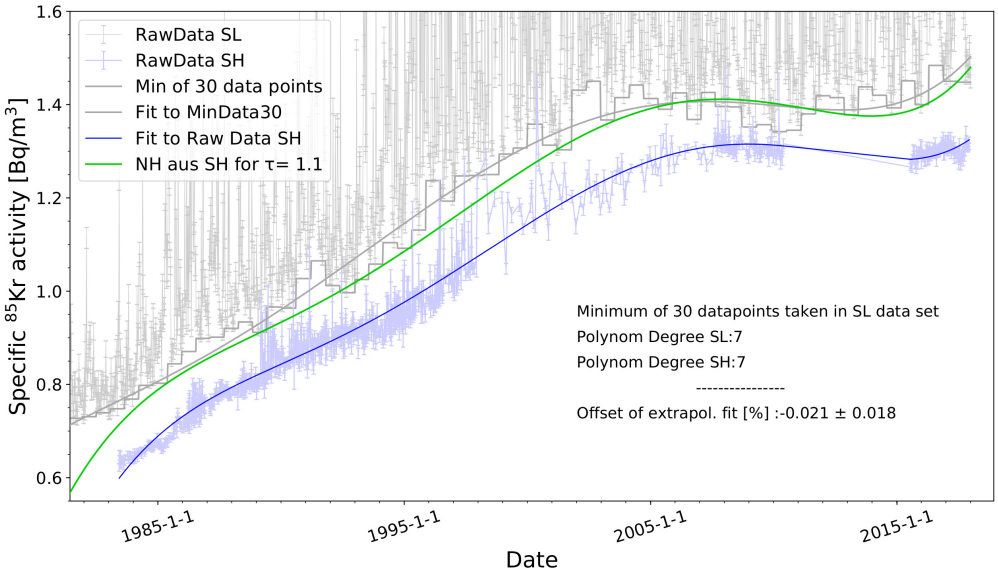

Figure 5.6.: With three different interhemispheric exchange times, potential average ^{85}Kr activities on the NH are extrapolated from the SH data.

the lower envelope (fit to the minimum of 30 data points) of the Schauinsland data are corrected for the radioactive decay and plotted as dashed lines. Assuming an environmental sample is taken and analyzed in December 2017 and its concentration is measured to be (0.5 ± 0.025) Bq/m^3 air, then two very different tracer ages are calculated depending on which input function is taken. For the sake of simplicity, the calculated tracer age is based on a piston flow model. Taking the local input function, the sample represents the atmospheric ^{85}Kr concentration on the 3rd of April 2000. In case the lower envelope of the Schauinsland data is taken as input function, the sample represents the atmospheric concentration on the 30th of December 2002.

The error bars represent an assumed measurement uncertainty of LLC and ATTA of 5 % (Ritterbusch, 2018). This leads to a tracer age uncertainty of $\pm$220 days for this specific concentration. Hence, the difference of 1000 days between the two input functions is a factor of ~4.5 times larger then the measurement uncertainty.

Analyzing now the two scenarios on the SH the picture is quite different. In general the two fits describe the SH data very well. The biggest difference is around the year 2010 so this is where the comparison is made. A sample analyzed in December 2017 with a measured ^{85}Kr concentration of (0.8 ± 0.04) Bq/m^3 results in a tracer age of 7.24 yr when the input function derived from the SH data is used. This corresponds to the atmospheric concentration on the 18th of March 2010. Taking the extrapolated fit from the Schauinsland data, the sample is about half a year younger. However, the age uncertainty is in the range of $\pm$300 days and with that, the difference of the two input functions lies

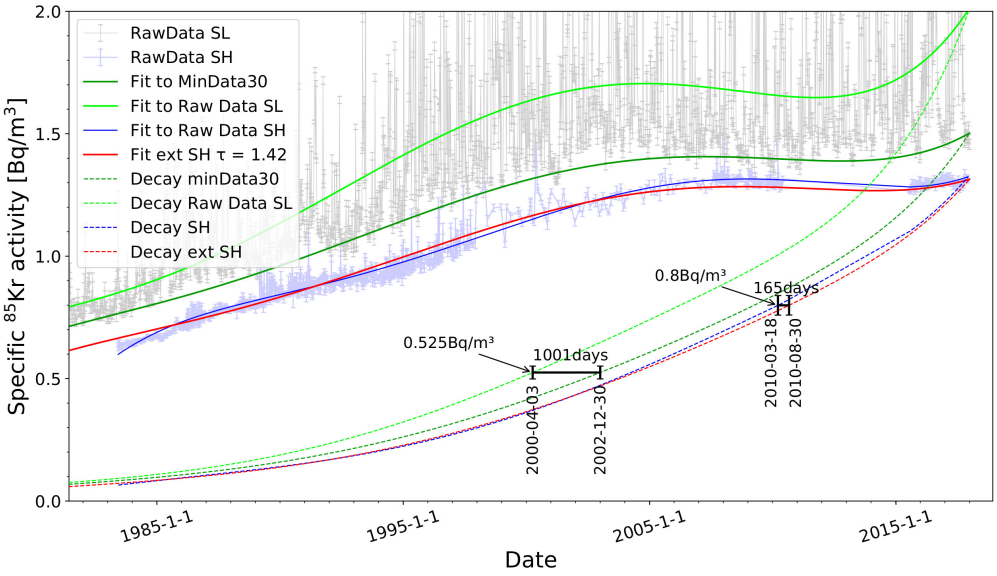

Figure 5.7.: Two different input functions on the NH and the SH are decay corrected and the effect of their differences on ^{85}Kr dating is evaluated.

within the measurement uncertainty even for the age range in which they differ the most.

From the above it can be concluded, that for studies on the NH it can make a huge difference if a local ^{85}Kr input function is taken or the estimated average one for the NH. Applying ^{85}Kr in oceanography, groundwater or ice studies requires a good knowledge of where the analyzed sample last equilibrated with the atmosphere on the NH and what the local input function has looked like. Although it is probably less crucial for ocean application considering the distance to reprocessing plants. For ice dating, application of ^{85}Kr is not so important as its dating range is easily covered by other methods like layer counting.

For the SH, ^{85}Kr applications are in general easier as one unique input function can be taken for evaluation. For measured activities below 0.08 Bq/m^3 air, meaning for samples equilibrated before 1983, the input function extrapolated from the Schauinsland data can be taken.

6. First ^{39}Ar ocean study in ATTA times

The potential of ^{39}Ar as oceanographic tracer has long been known in the ocean science community (Loosli, 1989). As a noble gas it is not involved in any biological or chemical processes and the atmosphere can be considered the only source for ^{39}Ar in the ocean, with an almost constant atmospheric ^{39}Ar concentration over the past 1000 years. With an air-sea gas exchange rate similar to that of oxygen, argon can be considered as constantly in equilibrium with the atmosphere (Stanley et al., 2009) and it covers perfectly the timescale of 50 to 1000 years over which ocean circulation takes place.

Because of these ideal properties, the tracer was applied in a few ocean studies with LLC already in the 1980s, despite the tremendous effort of sampling the required 1000 to 1500 L of water (section 3.1). With the latest progress in optimizing the ArTTA apparatus in Heidelberg, the required sample size for ^{39}Ar analysis could be reduced to 5 L of seawater, which might be the dawn of a new era in ^{39}Ar ocean dating. In this sense, the ocean campaign presented in the following can be seen as a pioneer project for this new era.

6.1. The M116 ocean cruise

From the 1st of May till the 2nd of June 2015, a research cruise was conducted along the 11th degree latitude from Guadalupe to Cape Verde with the Meteor III, the third biggest research vessel of Germany (Figure 6.1). The main objective of the cruise, with the name M116, was to investigate the eastern tropical North Atlantic (ETNA) oxygen minimum zone (OMZ). It is a poorly ventilated area in the North Atlantic with its center at around 8° N/23° W and can be subdivided into an upper and a lower OMZ at ~330 m depth and ~450 m depth respectively.

Oxygen minimum zones occur in regions where organic matter is quickly decomposed due to high biological activity consuming the present oxygen. In addition to that, only limited mixing with the oxygen rich ocean surface or deep waters takes place. This is the case close to the equator due to high water temperatures and near western coastlines in so called shadow zones of the large gyres of the ocean basins. In the center of the ETNA OMZ at 400 to 500 m depth reaches values < 60 μmol/kg compared to typically 250 μmol/kg at the oceans surface (Stramma et al., 2016). An ongoing deoxygenation of OMZs is observed throughout the ocean, with problematic consequences for ecosystems and the fishing industry. In Figure 6.2 the oxygen concentration measured during the M116 track is plotted. The

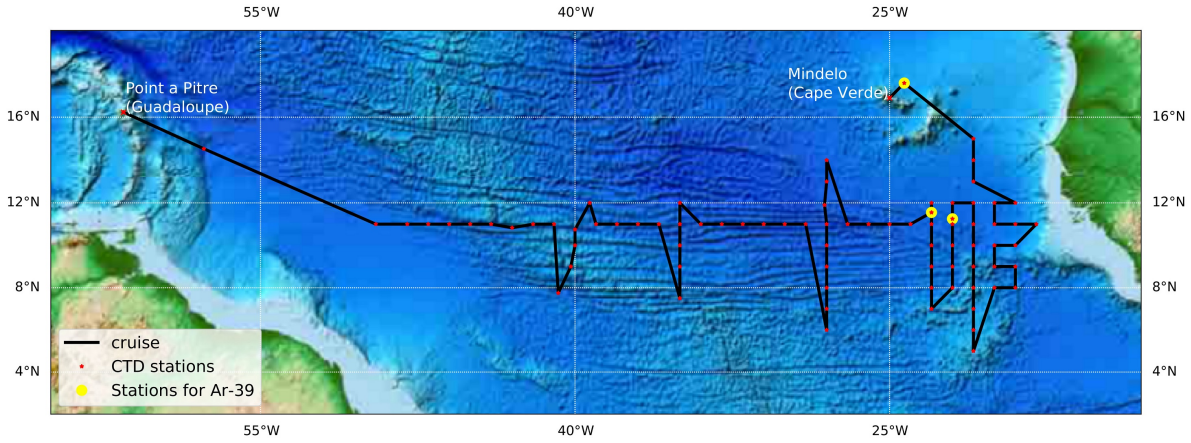

Figure 6.1.: Map of the M116 cruise track including the 82 CTD stations of which 3 were for sampling water for ^{39}Ar analysis.

OMZ is easily identified spreading far horizontally by starting already at about 42° W and with a strong oxygen concentration gradient in vertical direction.

To better understand the transport mechanisms of oxygen into these areas, two tracer release experiments have been performed. The Guinea Upwelling Tracer Release Experiment (GUTRE) in 2008 and the Oxygen Supply Tracer Release Experiment (OSTRE) in 2012. In 2008, 92 kg of the artificial tracer CF_3SF_5 was injected close to the center of the upper OMZ at 330 m depth, and in 2012 a similar amount of the same tracer was injected at 10°N/21°W at a depth of about 500 m. The isopycnals (the surfaces of equal density) in which the tracers were released are marked by the red lines in Figure 6.2

The M116 cruise performed the third mapping of the distribution of CF_3SF_5 that was injected during OSTRE, while also monitoring the tracer distribution of GUTRE. 27 scientists worked on the ship in different laboratories, although many of them were not involved in investigating the OMZ, but rather worked for their own projects ranging from marine biology to meteorology. Of the 82 CTD profiles that were taken along the cruise track heading east, 3 profiles were solely taken for ^{39}Ar analysis (see figure 6.1). On these three stations, all water sampled with the Niskin bottles was later used for argon extraction and no other tracer was measured on these water samples. However, CFC-12 concentrations were measured on all water samples of the remaining 79 CTD profiles, which will be compared to the ^{39}Ar results in the course of this chapter. For this comparison, the CFC-12 concentrations from stations next to those for the argon sampling and from the corresponding depth, extrapolated along lines of constant density were taken.

The sampling procedure for the 24 water samples for ^{39}Ar analysis is described in section 3.1. The first two stations (no. 44 and 55) are located ~500 km south of Cape Verde and 100 km apart from each other, while the third station (no. 82) is located ~100 km north of Mindelo, the destination harbor. At station 44 and 55, depth profiles down to 4000 m were taken while at station 82 the ocean ground was

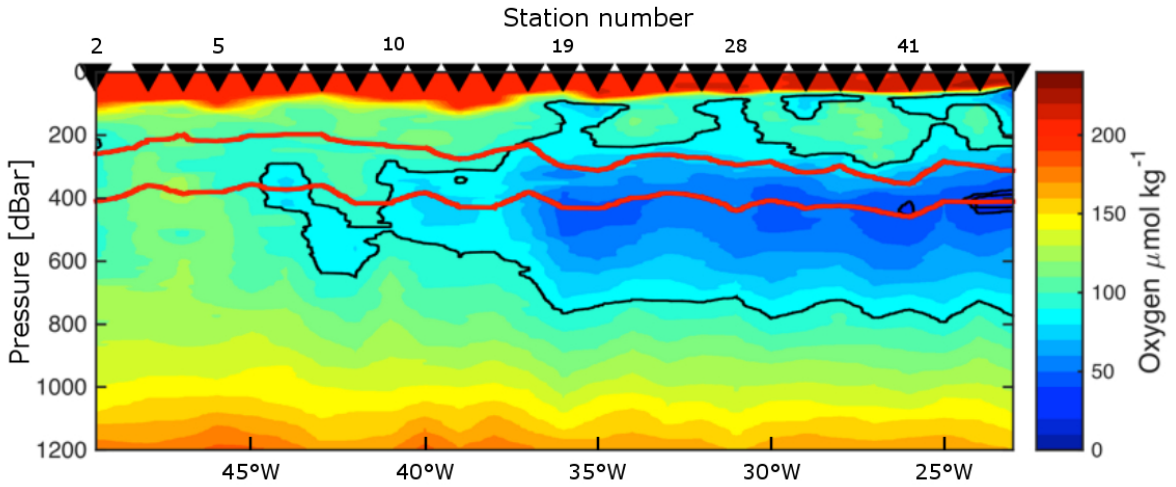

Figure 6.2.: The plot shows the oxygen concentrations in μmol/kg measured along the 11° N latitude during the M116 cruise. The black arrows at the top indicate the position of the CTD stations along the cruise and the red lines are the isopycnals that the artifical tracer CF_3SF_5 was released in, in the context of the GUTRE (upper line) and OSTRE (lower line) (Visbeck, 2016).

reached at 3500 m. As at station 44 and 55 the same depth was sampled, the samples are expected to be identical in ^{39}Ar.

6.2. Sample purification and analysis

In the months following the cruise, the 24 ocean samples arrived at the Institute of Environmental Physics in Heidelberg. Over the course of the following year, they were degassed and purified, partly in the context of a master thesis (Beyersdorfer, 2016). The setup used for purification is a previous model of the one described in section 3.1 and is based on the same principles of purification on hot titanium sponge getters.

In table 6.1 all purification and ^{39}Ar results are listed. Of the original 24 samples, sample #18 from profile 55 and Sample 5HD, 3HD and 4HD from profile 82 were not measured. The 4 samples labeled with 'HD' are 10 L stainless steel containers that were used to test different sampling containers than the propane gas bottles, but they proved to not be robust enough, as 3 out of 4 containers were either leaky or broke during transport. Sample #18 got contaminated with air during the purification and could not be evaluated.

The preparation of the remaining 20 samples was done according to the steps described in section 3.1. The degassing efficiency varied drastically depending on the number of shaking cycles and even more, depending on the gas composition of the samples at the time of the degassing. The longer the samples

Table 6.1.: Purification and measurement results of the 20 samples taken during the M116 cruise for ^{39}Ar analysis with the ArTTA apparatus in Heidelberg.

Station	**Sample**	**pressure**	**sampled water**	**S**	**T**	**expected Ar**	**extracted Gas**	**pure Ar**	**^{39}Ar result**
#	#	dBar	kg	‰	°C	mL STP	mL STP	mL STP	pmAr
44	10	4013	20.1	34.889	2.385	7.3	566.6±3.3	7.5	47.3±5.3
44	13	3001	22.2	34.923	2.737	7.9	522.8±3.1	6.6	35±4.2
44	4	148	24.1	34.954	4.334	8.4	617.5±3.6	6.1	46.2±6
44	9	997	22.0	34.807	5.614	7.4	691.4±4.0	6.8	54.7±5.1
44	20	447	22.5	35.063	9.948	6.9	585.3±3.4	5.3	78.7±7.7
44	17	398	23.1	35.1	10.409	6.8	539.1±3.1	5.7	80.3±7.6
44	19	349	22.0	35.19	11.192	6.6	525.5±3.0	6.5	74.9±7.1
44	14	12	20.7	35.909	24.954	4.9	520.3±3.0	5.2	95.2±9.4
55	5	4006	22.5	34.888	2.377	8.1	489.6±2.8	7.2	36±4.8
55	18	3000	24.0	34.922	2.733	8.6	Lost during purification		
55	8	1500	24.0	34.962	4.305	8.3	512.4±3.0	6,4	55.3±6.2
55	16	849	22.0	34.758	5.987	7.3	473.6±2.7	6.4	61.5±6
55	7	448	22.0	35.093	9.774	6.7	500.2±2.9	6.0	66.4±6.6
55	11	398	24.0	35.155	10.471	7.2	440.2±2.5	5.9	78.9±7.7
55	15	348	22.0	35.19	10.99	6.6	523.2±3.0	5.5	80.7±7.7
55	6	9	21.2	35.878	26.528	4.9	493.2±2.9	5.0	98.5±8.9
82	2	3498	25.0	34.907	2.514	9.0	828.4±4.8	5.4	36±5.3
82	5HD	2999	10.5	34.929	2.767	3.8	151.0±0.9	2.7	leaky
82	3HD	2996	10.0	34.929	2.768	3.6	153.2±0.9	3.1	leaky
82	3	1998	25.5	34.978	3.666	8.9	848.2±4.9	5.2	46.4±5.9
82	1	1498	25.0	35.011	4.659	8.7	1043.5±6.0	7.8	54.1±6.1
82	4HD	798	9.0	34.918	7.057	2.9	Broke during transport		
82	1HD	795	10.0	34.919	7.084	3.2	134.4±0.8	2.3	51.1±8.5
82	12	298	26.3	35.436	12.137	7.7	427.1±2.5	7.3	78.2±8.5

With: Δpressure = 1 dBar; Δsampled water = 0.2 kg; Δpure Ar = 0.1 mL STP; Δextracted Ar = 0.1 mL STP

were stored, the more the composition changed due to two effect: oxygen got removed through oxygen corrosion of the iron bottle, and hydrogen accumulated in the bottle through anaerobic corrosion (Reardon, 1995):

$$Fe + 2H_2O \rightarrow Fe^{2+} + 2OH^- + H_2. \tag{6.1}$$

All samples of profile 44 were prepared within half a year after sampling. Most other samples were processed more than 18 months after sampling, resulting in significant amounts of hydrogen that accumulated in the propane gas bottles. An additional step of pumping away the hydrogen from the liquid nitrogen cooled activated charcoal was added. Although the hydrogen should not make any difference for the degassing process of argon, as corresponding to Henry's law, the partial pressure of a gas species and not the total pressure is relevant. In reality, large amounts of hydrogen lower the degassing efficiency for all gases. The reason for this is probably the lower pumping capacity of the activated charcoal trap. Although hydrogen should not get adsorbed on activated charcoal at liquid nitrogen temperature, it might still block adsorption sites for other gases, due to its high partial pressure. Another reason is the high pressure in the head space in general, causing a slower gas flux between bottle and ACT. The purity of the final argon sample however, was >98 % for all 20 samples.

Within 3 months, all 20 samples have been measured by Sven Ebser with the ArTTA apparatus at the Kirchhoff-Institute for Physics in Heidelberg. An ideal measurement run for a 2 mL sample is pictured in figure 6.3.

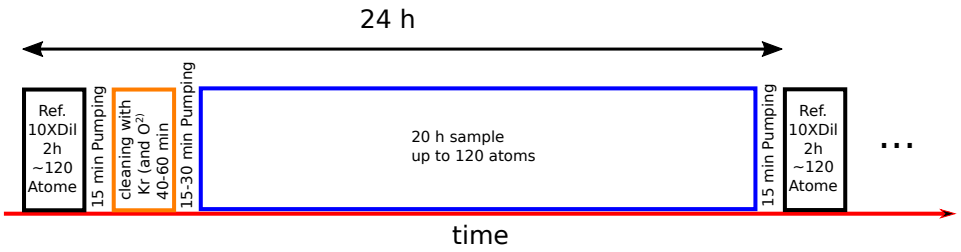

Figure 6.3.: Cycle of a daily measurement of an ^{39}Ar ocean sample with the ArTTA apparatus in Heidelberg. (Ebser, 2018)

In general, the analytical routine alternates between measuring the reference sample and measuring an ocean sample. The reference, which is argon 10 times enriched in ^{39}Ar, is measured for 2 h so that around 120 atoms are detected, assuming a count rate of 6 atoms per hour for a modern argon sample. Afterwards, the vacuum system is pumped and cleaned by flushing it for up to 1 h with a mixture of krypton and oxygen to minimize possible cross sample contamination. After additional pumping, the sample is introduced into the system and measured typically for 20 h. Finally, the cycle is restarted by preparing the system for the reference sample.

The purified argon amounts vary between 5 mL and 7.5 mL for the propane gas bottles. This mainly

depends on the water amount sampled, the degassing efficiency as well as the temperature and salinity the sampled water had when it originally equilibrated with the atmosphere. Each sample was split into three fractions and measure with 1.7 mL to 2.5 mL of argon. The advantage is, that during 3 times 20 h analyses, the contribution of background contamination from the former enriched ^{39}Ar calibration measurements (see subsection 3.3.1) is by far lower than during one measurement of 60 h.

6.3. Data evaluation

In Figure 6.4 the final ^{39}Ar concentrations are plotted versus ocean depth. The stars indicate the results of the single split measurements, while the circle represents the average concentration for the sample. The map in the lower right corner indicates the location of the stations the samples were taken from. As station 44 and 55 are only ~100 km apart, the samples taken at the same depth are treated as A and B samples of the same water mass . Therefore, the results of these samples were averaged and are represented by the blue dots in the graph. The red dots represent the averaged single measurements of the samples from station 82.

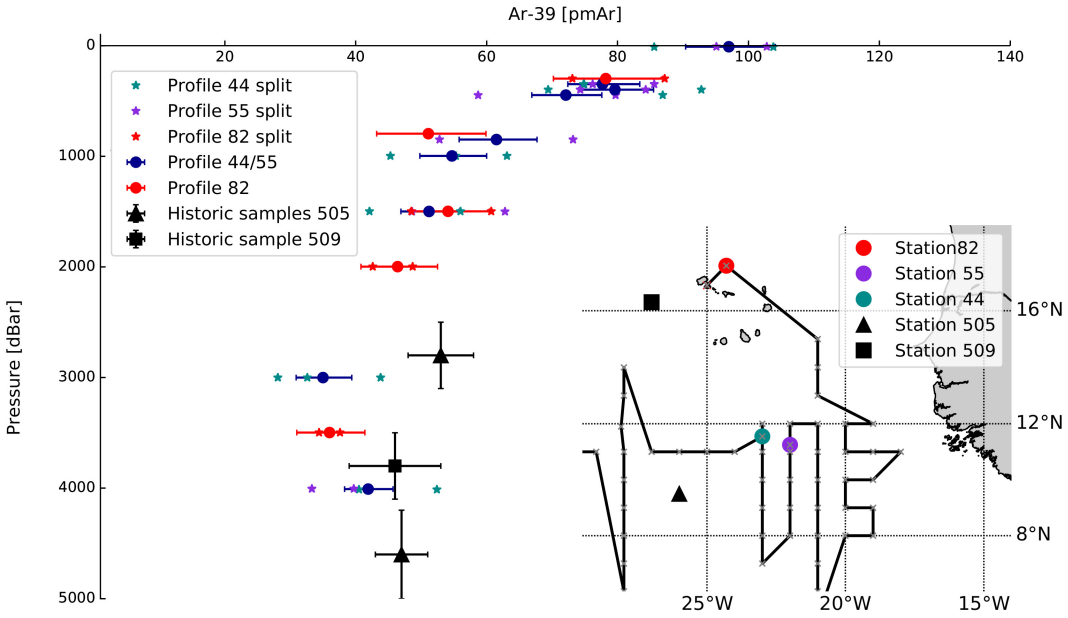

Figure 6.4.: The final ^{39}Ar results plotted against depth. Historic values are taken from Schlitzer et al. (1985).

The errors of a single measurement includes the statistical error of the atom counting, the error of the background contamination and the error of the reference, and is in the order of ~10 %. Averaging over the single measurements yields in the plotted errorbars. A detailed calculation of the errors can be found in Ebser, 2018.

The ^{39}Ar results for each sample are listed in Table 6.1. As expected, the ^{39}Ar concentration decreases with increasing depth. Within the first 1000 m it drops rapidly from the initial near 100 pmAr to almost 50 pmAr. Between 1000 m and 2000 m, ^{39}Ar concentrations decrease further but with a lower gradient to 46 (-5.6 +6.1) pmAr for the 2000 m sample of station 82. The lowest values are found in the 3000 m sample of station 44 with an ^{39}Ar concentration of 35 (-4.1 +4.4) pmAr. At 4000 m the ^{39}Ar concentration seems to slightly increase again.

As a comparison, three historic samples are included in the figure. They originate from a cruise in April 1981 that sampled for ^{39}Ar along a meridional section from 8° S to 45° N in the eastern Atlantic (Schlitzer et al., 1985). For one single ^{39}Ar value, four 250 L Gerard-Ewing samplers were connected in series over a length of ~400 m, hence, represent an average of 400 m water column, resulting in the errors on the y-axis in Figure 6.4. The water was degassed on board and measured over 6 weeks with LLC. At station 509 one sample was taken and the result fits quite well to the results of the recent campaign. The upper of the two samples taken at station 505 sampled in 1981 shows significantly higher ^{39}Ar concentration than the samples presented here. This might be due to statistical fluctuations or a slightly different flow regime further south west of the investigated locations.

The sampling for ^{39}Ar in this region had two main objectives. First, sampling for a complete depth profile in a resolution that has never been possible before, thanks to the reduced sample size. With that, the age distribution of the sampled water bodies in that region can be derived by combining the ^{39}Ar information with that of a second tracer. Secondly, to see if ^{39}Ar brings new insight into the ventilation of the eastern Tropical North Atlantic Oxygen Minimum Zone (ETNA). This is why the density of samples taken is the highest in the corresponding depth between 300 and 450 m.

The different ^{39}Ar concentrations measured are closely related to the history of the water masses they were sampled from (the concept of water masses is introduced in subsection 2.1.1). To distinguish water masses, it is helpful to plot the two parameters salinity and temperature, as done in Figure 6.5. For all 82 stations of the M116 cruise, the CTD sensor mounted to the sampling rosette monitored the in-situ temperature and salinity in increments of 1 m depth. The temperature is then converted into potential temperature by correcting for the effects of compression according to Equation 2.5. Of the 82 depth profiles taken during the cruise, 26 were deep profiles down to the ocean floor while the remaining 56 were profiles taken down to 1200 m, and no deeper than 2000 m (Visbeck, 2016).

In Figure 6.5 the salinity is plotted against the potential temperature, derived from the high resolution CTD measurement of all 82 stations. The depth is color coded and the three profiles from which the argon samples originate are highlighted. The biggest changes in salinity and temperature occur in the topmost layer of the ocean down to ~300 m, which is not very surprising as the gradient represents the thermocline and the increased salinity is an effect of evaporation at the ocean surface.

The terminology and differentiation of the different water masses applied in the following is based on Emery et al. (1986). Vertically, the water masses can be divided into upper (0 - 500 m), intermediate

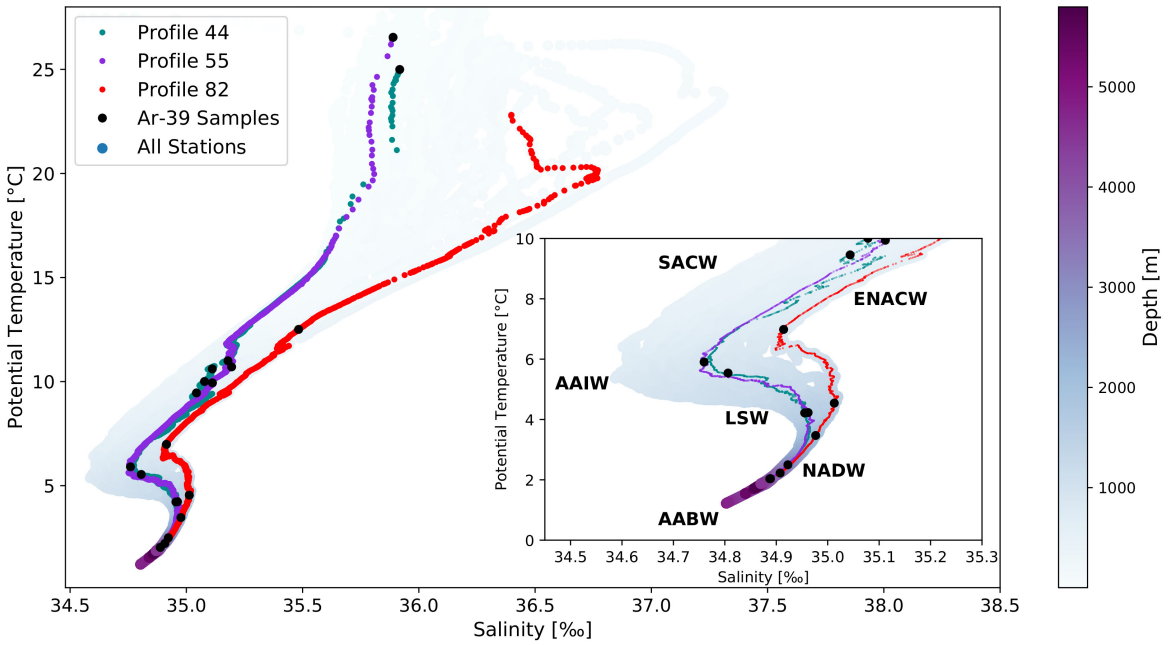

Figure 6.5.: The salinity is plotted against the potential temperature for all 82 stations. The three sampling stations are highlighted and the depth that each data point is taken from is indicated by the color code. In the lower right corner, a magnification of the samples below 1000 m is shown, and the main water masses are identified according to their temperature and salinity signature.

(500 - 1000 m) and deep waters (1.500 m to bottom). The upper water masses influencing the study area are the South Atlantic Central Water (SACW) and the Eastern North Atlantic Central Water (ENACW). Their temperature is relatively similar, but they can be distinguished by the increasing salinity towards the East, due to the influence of the Mediterranean Sea. This is also the reason for the significant difference in the entire depth profiles of 44/55 and 82. Although all three stations lie on a similar degree longitude, the influence of the very salty Mediterranean water is much stronger 6° of latitude further north.

The first relevant intermediate water mass along that transect is the Antarctic Intermediate Water (AAIW), which is formed in the Antarctic Polar Front zone around 50° to 60° south and characterized by its relatively low salinity. It spreads typically up to 20°N. The second intermediate water is the Labrador Sea Water (LSW) which is part of the upper stream of the North Atlantic Deep Water (NADW).

The two deep water masses that are most likely represented by the water sampled at depth below 1500 m are the NADW and the Antarctic Bottom Water (AABW). The NADW is the major deep water mass in the North Atlantic. It is a mix of several water masses formed in the Arctic and flows after formation along the west side of the Mid-Atlantic Ridge, to the South and near the Equator, and across

to the eastern Atlantic. The AABW is the densest water mass in the entire ocean due to its very low temperatures of down to -0.8 °C. Because of that, it is the major water mass below 4000 m in most (southern) ocean basins.

The influence of the AABW is possibly the reason for the slight increase in ^{39}Ar of the samples taken at 4000 m depth at station 44 and 55. The reason that the AABW is 'younger' in this part of the ocean is related to the flow path of the NADW and the AABW. A part of the AABW flowing north along the west site of the Atlantic ocean basin crosses the Mid-Atlantic Ridge sooner through the Vema Fracture Zone and with that, has a shorter transit time to the ETNA than the NADW.

6.3.1. Constraining the TTD

Both questions raised above, regarding the ventilation of the oxygen minimum zone and regarding the mean ages of the sampled water column, can be addressed by analyzing the age distribution of the sampled water with a second tracer. As described in section 2.3, the transit time distribution (TTD) of a water body is a key factor in investigating the ocean ventilation or calculating the concentration of any atmospheric component in the water, like the anthropogenic fraction of CO_2, as long as its atmospheric input function is known. The probability density function that has proven successful as the TTD in former ocean studies is the Inverse Gaussian (IG), presented in Equation 2.3 (Waugh et al., 2003; Schneider et al., 2014).

As a TTD, the IG propagates the equilibrium gas concentrations at the ocean surface into the ocean interior, reflecting the processes of mixing by convection and diffusion. This is expressed by the convolution integral in Equation 2.19. In order to calculate a tracer concentration in a water parcel, the first two moments of the probability function, the mean (age) and the width, must be given. Conversely, when the atmospheric input function of a tracer is known and its concentration in a water parcel is measured, one can partly solve the inverse problem and reduce the variables to one. When a second tracer is applied, the TTD can be fully constrained.

The second tracer used in this study is CFC-12. It was measured from each Niskin bottle at every station, except for the three stations used solely for argon sampling, as all water from these casts was needed for ^{39}Ar analysis. After each cast, a 200 mL glass syringe was sampled from each Niskin bottle and the CF_3SF_5, CFC-12 and SF_6 concentrations were measured with a commercial gas chromatograph in a laboratory on board. Because of its longer atmospheric history and higher concentrations, CFC-12 was chosen for the comparison with ^{39}Ar. The CFC-12 values taken are plotted in Figure 6.6 and listed in Table 6.2.

The atmospheric CFC-12 concentration was basically zero before the year 1940, hence, the measured concentrations drop rapidly from 1017 fmol/kg to 16 fmol/kg at 1000 m depth. The right box in the graph is an enlargement to the CFC-12 concentration beneath 1500 m. Although the concentrations are

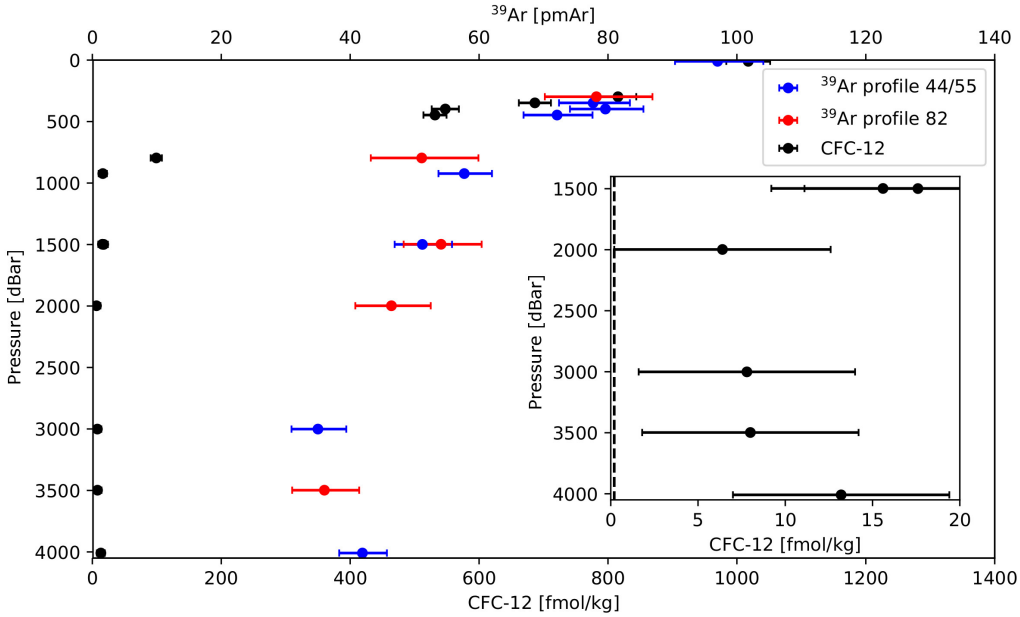

Figure 6.6.: On the lower x-axis the CFC-12 concentrations and on the upper x-axis the ^{39}Ar concentrations are plotted against depth. The plot in the lower right corner is an enlargement of CFC-12 concentrations below 1500 m. The dashed vertical line represents the detection limit of the CFC-12 measurements.

lower than the surface by a factor of 100, they are still higher than the detection limit (indicated by the dashed line) within 1 sigma confidence. Still, the relative error is close to 100 % making the tracer not well suited to constrain the TTD in this region, as will be seen in the following.

One important fact to remember is, that the knowledge of the atmospheric input function required for the analysis of a measured tracer concentration includes the knowledge of the equilibration conditions in the formation area of the sampled water. This is especially true for CFCs, as their solubility varies drastically with temperature. The Ostwald Solubility of CFC-12, calculated after Plummer et al. (2006), is about $2{\cdot}10^{-3}$ for T = 25 °C (S = 35 ‰), which are equilibration conditions in the study area and about $6{\cdot}10^{-3}$ for T = 1.5 °C (S = 35 ‰), which are realistic infiltration conditions in the formation area of NADW and AABW.

The process of constraining the TTD for a sample with known ^{39}Ar and CFC-12 concentration is demonstrated in Figure 6.7. The plot in the upper right corner shows different IG distributions with a mean age Γ of 335 yr and varying width Δ, expressed as the ratio Δ/Γ. The higher the ratio, the higher the younger contribution, but at the same time the longer the tail of the distribution towards older water. A lower ratio shifts the peak of the distribution closer to the mean age. When the ratio is diminishing, the distribution approaches a delta distribution, which is the Piston flow model with a purely advective flow and a mean age equal to the tracer age. In many ocean applications only one tracer is available for retrieving the IG-TTD. Typically the ratio is then assumed to be one and the mean age is the only free

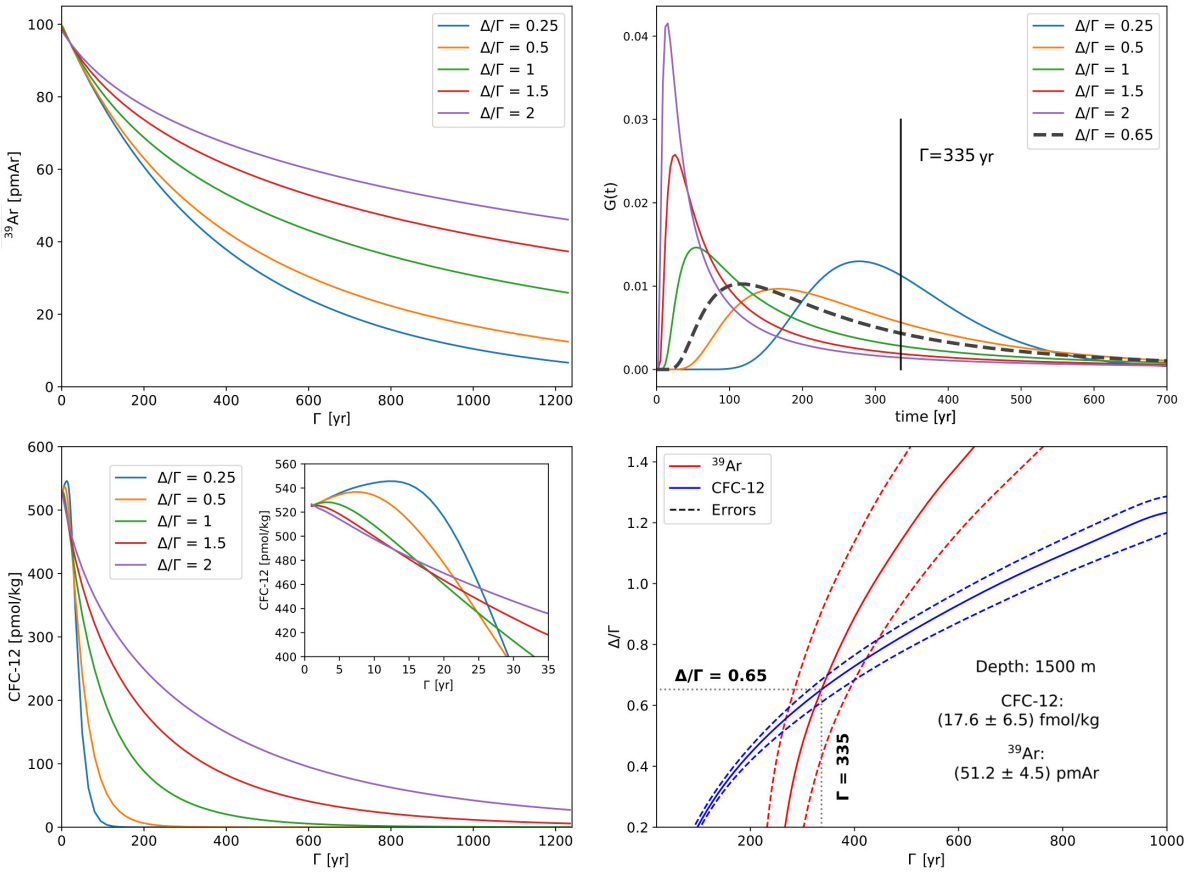

Figure 6.7.: Four plots illustrating the process of constraining the TTD with known ^{39}Ar and CFC-12 concentrations. The upper left plot shows the ^{39}Ar concentrations that a water parcel would have as a function of mean age Γ, calculated for 5 different Δ/Γ. In the lower left, the same is done for CFC-12. In the upper right corner, 6 different Inverse Gaussian probability density functions are plotted for fixed $\Gamma = 335$ yr and different Δ/Γ ratios. Their shape is fully constrained by the first two moments, mean age Γ and width Δ. In the lower right, Δ/Γ is plotted against Γ for the CFC-12 and ^{39}Ar concentration of the sample from 1500 m depth of station 82. The intersection constrains both moments of the TTD.

variable constrained with the measured tracer.

The two left plots in Figure 6.7 illustrate the result of the convolution integral (Equation 2.19) for a given input function for Γ between 0 and 1200 yr and 5 fixed Δ/Γ ratios. In the case of ^{39}Ar, the input is assumed to be constant with 100 pmAr. Even after half of the ^{39}Ar in a sample is decayed (i.e. an ^{39}Ar tracer age of 269 yr), the mean age is about 1200 years for an IG age distribution with $\Delta/\Gamma = 2$.

The ^{39}Ar tracer ages always underestimate the mean age calculated with an IG-TDD. The IG weighs the young fraction of water more and thus, yields higher mean ages than a Piston flow model. At least for very young waters this is different for CFC-12. Within a 30 yr BP, the tracer age overestimates the mean age of a IG-TTD due to the convex shape of the input function during this time, as seen in the

inset graph in the lower left plot.

Plotting now Γ versus Δ/Γ results in the graph shown in the lower right corner of Figure 6.7. Here, the ^{39}Ar and CFC-12 concentration are given, with each dot on the curve representing one solution for an age distribution with the specific combination of mean and width for this concentration. The concentrations taken are the ^{39}Ar and CFC-12 concentration measured at 1500 m depth for the combined profile 44/55. The solid lines represents the mean of the measured concentrations and the dashed line stands for the 1-σ interval. The intersection of the solid lines gives a Γ of 335 yr and a Δ/Γ ratio of 0.65 as a constraint for the age distribution of the sampled water. This distribution is represented by the thicker dashed line in the upper right graph of the same figure.

At this stage the great potential of ^{39}Ar as an age tracer for ocean dating becomes evident. In order to get a clear intersection, tracers with a sufficiently different but still overlapping time scale must be applied. As ^{39}Ar is the only tracer on the timescale between 50 and 1000 years, it is ideally suited for constraining the TTD together with a younger tracer like CFC-12 or ^{85}Kr. ^{14}C is in general also suitable to date in the range of centuries due to the high measurement accuracy of the Accelerator Mass Spectrometers nowadays. However, the interpretation of ^{14}C data in the ocean is very difficult (subsection 2.2.3).

Without the additional information of ^{39}Ar, a Δ/Γ of 1 was typically assumed, leading in this case to a mean age of ~700 yr when only relying on the CFC-12 data.

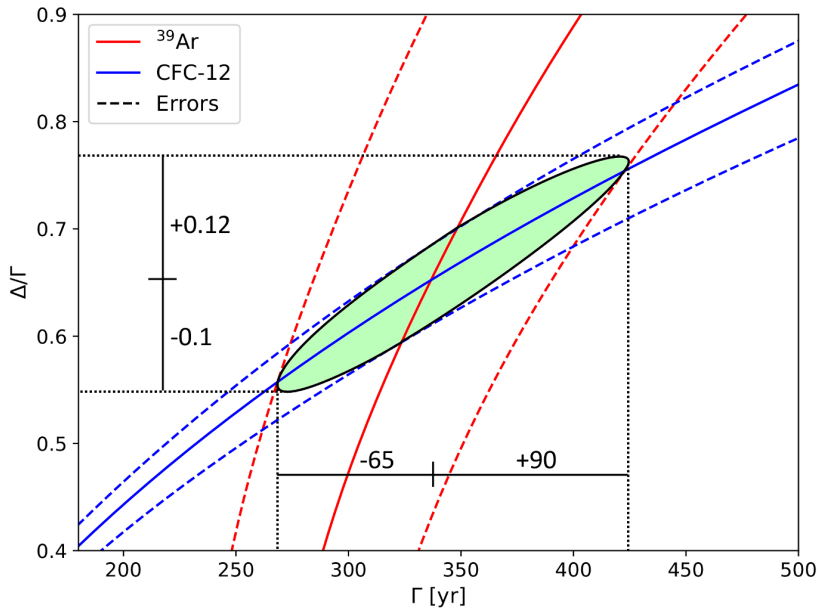

Figure 6.8.: Error estimation of Γ and Δ/Γ for the constrained TTD.

The error estimation of the constrained mean age and width is illustrated in Figure 6.8, following the idea of Ebser (2018). The intersection of the ^{39}Ar line with the error line of CFC-12 is the 1-σ interval

for ^{39}Ar and the same applies for CFC-12. Hence, all combinations of Γ and Δ/Γ in a 1-σ interval around the crossing of the mean concentrations of ^{39}Ar and CFC-12 are expected to be within the green area formed by the distorted ellipse. As a conservative estimate of the error, the largest extent in x and in y direction of the ellipse is now taken as the error of Γ and Δ/Γ.

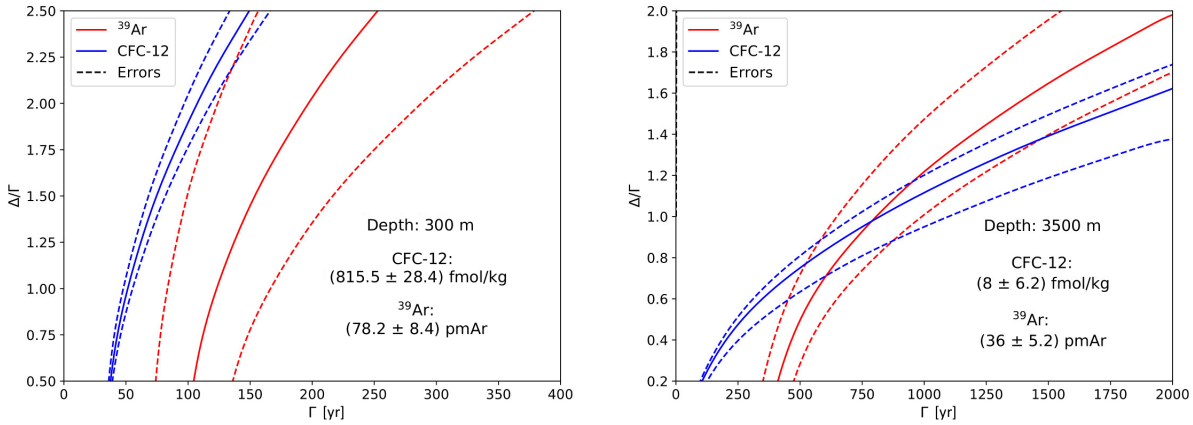

Figure 6.9.: Two examples from depths in which the TTD can not be well constrained by the tracer combination CFC-12 and ^{39}Ar. On the left site, a sample from the oxygen minimum zone is displayed and on the right side, the sample from 3500 m depth is shown.

Constraining the TTD does not work equally well in all depths. In Figure 6.9, Γ is plotted against Δ/Γ for one sample from the center of the oxygen minimum zone and for the sample from 3500 m depth of profile 82. The left plot clearly demonstrates, that no reliable statement on the age distribution can be derived from the combination of the two tracers in this depth. First, because the error of the ^{39}Ar values is much too large and secondly, because the curves are almost parallel up to a ratio of 2.5. This behavior is caused by the fact that ^{39}Ar is already quite depleted with 77.7 pmAr, while the CFC-12 concentration is still comparably high. For modeling the trend of the CFC-12 concentration for this depth, an infiltration temperature of 25 °C was used, which could be argued is too high when the water is influenced by AAIW. Still, the main problem of the large uncertainty of the ^{39}Ar value for all samples in the upper 500 m makes an application of the TTD method not feasible.

For the deepest sample, constraining the TTD results in large errors as well. Here, because of the almost parallel trend of both tracers due to the smaller concentrations of ^{39}Ar. In this region it would be more beneficial to use ^{14}C in combination with ^{39}Ar, as it has a much steeper slope and therefore, a more orthogonal intersection. The final results of all Γ and Δ/Γ that could be constrained with the measured CFC-12 and ^{39}Ar concentrations are plotted in Figure 6.10 and listed in Table 6.2.

The TTDs that could not be well constrained are easily recognizable in Figure 6.10 by the large error bars. The samples taken around 400 m at station 44 and 55 yield good results for the mean age, however, the Δ/Γ is very badly constrained as a consequence of the large error of ^{39}Ar and the still relatively high

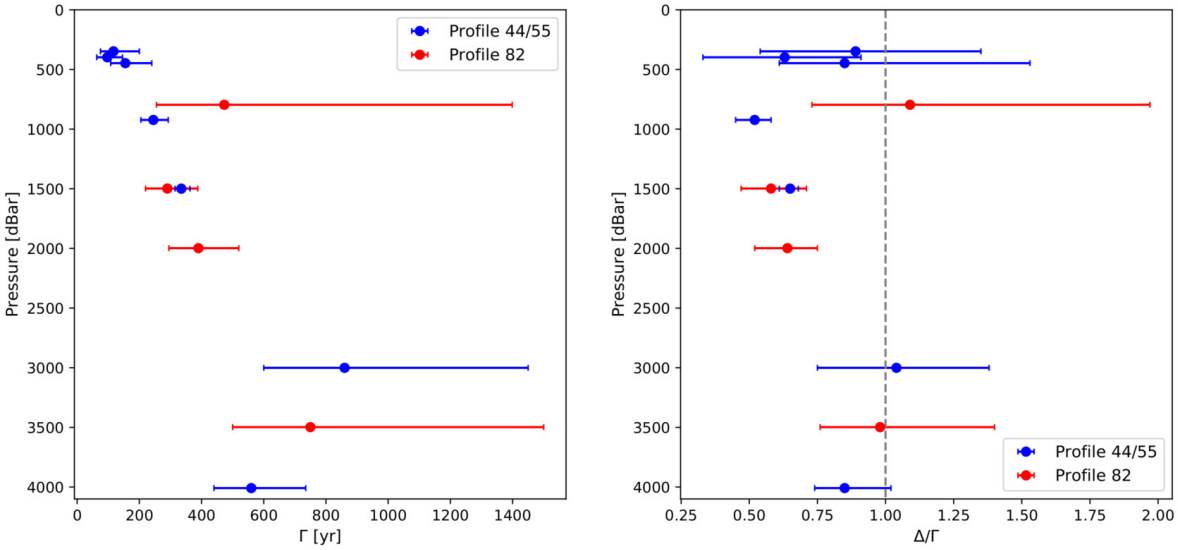

Figure 6.10.: Γ and Δ/Γ are plotted against depth for the joint profiles 44/55 and profile 82.

CFC-12 concentrations. For the samples from 3000 m and 3500 m depth it is the other way around. The Δ/Γ is about one and the errors are slightly smaller, but the mean age is poorly constrained. The samples between 1000 and 2000 meters yield the best results, as already discussed above. Looking at the trend in the mean ages with depth, it is striking that the mean age jumps from about 400 yr at 2000 m depth to about 800 yr at 3000 m depth. Although the mean age is very uncertain here, it is interesting that such a trend is only revealed when calculating mean ages and not from the tracer ages, as the different Δ/Γ ratios drastically change the age distribution. It would be really good to have a higher sample resolution in this region and more precise ^{39}Ar measurements to further investigate the transition between these two different flow regimes.

Once the TTD is known for a particular part of the ocean, it can be applied to any other substance that originates in the atmosphere and infiltrates the ocean. The most prominent example is the calculation of the anthropogenic CO_2 budget of the ocean as done in Schneider et al. (2012) and Steinfeldt et al. (2009). Since fossil fuels are burnt on a major scale since the beginning of industrialization ~150 years ago, a record of the atmospheric budget of this ^{14}C dead carbon is extracted from multiple proxies like trees. Due to the high solubility of CO_2 the ocean is by far the largest carbon sink, while the CO_2 budget of the biosphere is highly unknown. Hence, constraining the anthropogenic CO_2 budget of the ocean helps evaluating the anthropogenic CO_2 budget of the biosphere.

Considering the major role of CO_2 in climate change, it also helps to better predict the effect of future climate change scenarios when the buffer capacity of the ocean is known. For example when CFC-12 is the only tracer and the IG age distribution of the water body at 920 m depth at station 44/55 is estimated with $\Delta/\Gamma = 1$, then a mean age of $\Gamma = 700$ years is calculated. The anthropogenic carbon

Table 6.2.: The final results for Γ and Δ/Γ are listed as well as the ^{39}Ar and CFC-12 values that were used to constrain the TTD for the specific depth.

Station	**pressure**	**T**	**S**	**^{39}Ar**	**CFC-12**	Γ	Δ/Γ
#	dBar	℃	‰	pmAr	fmol/kg	yr	
44/55	4009	2.38	34.88	$41.9^{+3.8}_{-3.6}$	13.2±6.4	560^{+175}_{-120}	$0.85^{+0.17}_{-0.11}$
44	3001	2.74	34.92	$35.0^{+4.4}_{-4.1}$	7.8±6.2	860^{+590}_{-260}	$1.04^{+0.34}_{-0.29}$
44/55	1499	4.32	34.88	$51.2^{+4.6}_{-4.3}$	17.6±6.5	335^{+28}_{-20}	$0.65^{+0.03}_{-0.04}$
44/55	923	5.8	34.78	$57.7^{+4.3}_{-4.0}$	16.2±6.4	245^{+48}_{-40}	$0.52^{+0.06}_{-0.07}$
44/55	447	9.86	35.08	$72.1^{+5.5}_{-5.2}$	431.6±17.9	155^{+85}_{-47}	$0.85^{+0.68}_{-0.24}$
44/55	398	10.44	35.13	$79.6^{+5.9}_{-5.5}$	547.6±21.1	97^{+49}_{-34}	$0.63^{+0.28}_{-0.3}$
44/55	348	11.1	35.19	$77.7^{+5.7}_{-5.3}$	686.6±24.9	117^{+83}_{-42}	$0.89^{+0.46}_{-0.35}$
44/55	10	25.74	35.89	$97.0^{+7.1}_{-6.6}$	1017.6±34.0	-	-
82	3498	2.51	34.91	$36.0^{+5.4}_{-5.0}$	8.0±6.2	750^{+750}_{-250}	$0.98^{+0.42}_{-0.22}$
82	1998	3.66	34.98	$46.4^{+6.1}_{-5.6}$	6.4±6.2	390^{+130}_{-95}	$0.64^{+0.11}_{-0.12}$
82	1498	4.66	35.01	$54.1^{+6.3}_{-5.8}$	15.6±6.4	290^{+98}_{-70}	$0.58^{+0.13}_{-0.11}$
82	796	7.07	34.92	$51.1^{+8.8}_{-7.9}$	99.2±8.7	473^{+926}_{-218}	$1.09^{+0.88}_{-0.36}$
82	298	12.15	35.44	$78.2^{+8.7}_{-8.0}$	815.5±28.4	-	-

budget estimated from that age distribution is significantly lower than when an IG age distribution with a $\Delta/\Gamma = 0.65$ is taken and a Γ of 335 yr is derived. This is obvious, as in the first scenario a larger part of the water body consists of older water that had no, or a much lower uptake of anthropogenic CO_2 when it last equilibrated with the atmosphere.

For robust statements on the anthropogenic carbon budget in the ocean or for conclusions on ventilation processes in general, the ocean must be investigated with ^{39}Ar on a much larger scale, which will hopefully be done in many future ocean cruises. As currently only 5 L of seawater is required for analysis with ATTA, the sampling for ^{39}Ar can be included in the standard sampling routine together with other tracers during one CTD cast. With that, the biggest obstacle for ocean applications with ^{39}Ar is removed and thus, the way is paved into a new era of ^{39}Ar ocean dating.

7. Conclusion and Outlook

The work performed in the context of this thesis pushes the application of noble gas radionuclide dating in hydrology and oceanography in two respects. First, by developing sampling and sample preparation methods for argon and krypton and secondly, by applying ^{39}Ar and ^{85}Kr to various environmental reservoirs.

The technical progress comprises the sampling techniques applied for measuring ^{39}Ar on seawater during the M116 cruise, the support in constructing a groundwater degassing setup and an argon purification setup at the Institute of Environmental Physics (IUP) in Heidelberg, as well as the construction and further development of an argon and krypton separation setup at the CSIRO in Adelaide. The recommissioning and improvement of the proportional counter setup for ^{85}Kr analysis at the CSIRO could only be accomplished to a certain extent as the stay in Australia came to an end.

The performance and efficiency of the setups satisfy the expectations. The argon and krypton separation setup in Adelaide yields an argon purity of >99 % and a recovery of >95 % and a krypton purity and recovery of >90%. Both noble gases can be separated from a 5 L to 80 L gas sample within 6 hours. The argon purification setup for water samples of up to 20 L and ice samples of up to 10 kg yields a purity >98 % and a recovery of >95 % while multiple samples can be purified in one day.

Three different environmental reservoirs have been investigated in the context of this thesis by applying the noble gas radio isotopes ^{39}Ar and ^{85}Kr (amongst other tracers).

The first study reported on a groundwater field campaign on Rottnest Island in Western Australia. Here, 8 different wells were sampled in order to investigate the island's freshwater lens. The field trip was carried out under extreme conditions as the analysis of ^{39}Ar and ^{85}Kr with Low-Level counting requires about one ton of water which could not be extracted from the thin monitoring wells. Back then, the ArTTA apparatus in Heidelberg was not ready yet to promise the analysis of ^{39}Ar on 20 L water samples. In the end, the data analysis was limited to four wells and four tracers resulting in different mean ages of the freshwater lens. The evaluation with a lumped parameter model could only vaguely confirm the recharge rate to the lens estimated in former studies.

Unfortunately, the sample size required for LLC can be a restricting factor even in groundwater studies. If only 20 L of water had been needed for ^{39}Ar and ^{85}Kr analysis, as is currently the case for ATTA, the outcome of the study would have been most likely much more satisfying.

The second study is based on the weekly sampling of atmospheric ^{85}Kr at the CSIRO in Adelaide and

represents the first ^{85}Kr data set taken in the southern hemisphere in more than five years. Sampling began in July 2015 in the context of this thesis and was continued in Adelaide on a weekly basis, resulting in a data record of more than two years. The new southern hemispheric ^{85}Kr data was compared with existing data from the southern hemisphere and with the atmospheric concentration of ^{85}Kr measured at the Schauinsland station near Freiburg, Germany.

Several conclusions were drawn from the evaluation and comparison of the data sets: First, the atmospheric ^{85}Kr input functions for the southern hemisphere, the northern hemisphere and for the area represented by the Schauinsland data were calculated. Secondly, an interhemispheric exchange time of about 17 months was derived from the ^{85}Kr activity concentration difference of the two hemispheres. Finally, the impact of an uncertainty in the atmospheric input function on calculations of ^{85}Kr tracer ages was estimated.

For the third study, 3 depth profiles with 20 water samples in and around the oxygen minimum zone near Cape Verde have been taken, prepared and evaluated in the course of this thesis. Two main conclusions could be drawn from the study: First, by evaluating the ^{39}Ar results together with CFC-12, the age distribution of the sampled water mass could be constrained for that particular part of the ocean. In doing so, the waters between 1000 and 3000 meters depth were identified to have a lower mean age than assumed from only using CFC-12. This has significant consequence for the anthropogenic carbon budget, for instance.

The second important outcome is the "Yes we can!" message. The reduction in sample size for ^{39}Ar analysis with ATTA to about 5 L of water opens the door to large scale ocean campaigns for mapping the entire ocean with ^{39}Ar. From a technical perspective, this was possible from the moment the ArTTA apparatus was operated in recycling mode but a first application was crucial as proof. Thanks to the joint effort of the complete ArTTA group in Heidelberg, the demonstration succeeded.

Such applications are only the start of a wide range of campaigns yet to come. Groundwater is the reservoir in which noble gas radioisotopes have been applied the most so far since the extraction of larger water quantities is easiest there. However, as experienced during the Rottnest Island study, there are groundwater systems that can only be analyzed with noble gas radioisotopes when significantly smaller sample sizes than required for LLC are sufficient.

The potential of a tracer for dating a specific reservoir is closely related to the time scales they work on. ^{81}Kr with its dating limit of above one million years is perfectly suited to date old groundwater and ice, as already shown in different studies (Sturchio et al., 2004; Buizert et al., 2014).

The largest potential of ^{39}Ar as an age tracer is clearly its application in oceanography. Ideally, samples for ^{39}Ar would be taken on a large scale ocean campaign to cover the entire ocean, as has been done for CFCs and ^{14}C during the World Ocean Circulation Experiment (WOCE). For such an undertaking, the analytical capabilities must be raised significantly by setting up new ATTA laboratories for ^{39}Ar analysis around the globe.

Another promising application of ^{39}Ar is the dating of glacier ice that formed during the last millennium. In Europe, alpine glaciers are an obvious target and the analysis of their flow behavior, growth rate and preserved climate signals will be one of the next objectives of the ArTTA group in Heidelberg.

The dating range of ^{85}Kr is well covered by many other tracers. Still, due to its nearly perfect tracer properties it will be applied more often, once the costs for analysis with ATTA are comparable to those for tritium and CFC analysis. The possibility of measuring ^{85}Kr together with ^{81}Kr on the same sample is very useful to quantify atmospheric contamination during sampling and might be done for ^{39}Ar analysis in the near future as well.

All these scenarios must be accompanied by corresponding developments of sampling and sample preparation methods to allow for an easy field application for oceanographers, groundwater hydrologists and glaciologists.

The studies and method developments conducted in the course of this thesis constitute an important step towards the outlined future applications of dating with noble gas radioisotopes.

A. Appendix

Further krypton purification with the getter at the Ar and Kr separation setup

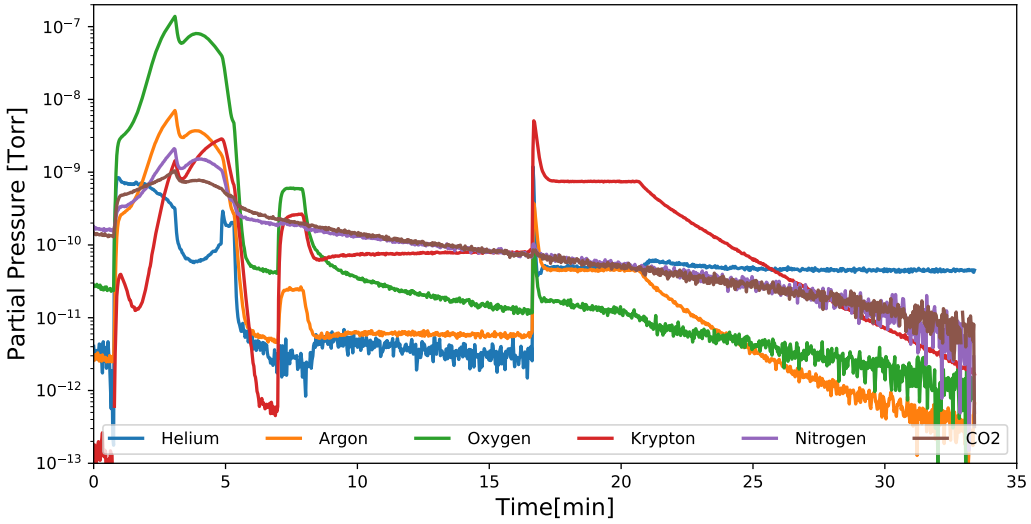

Figure A.1.: The RGA scan illustrated the further purification of the krypton fraction after the separation process on the zeolite columns.

In the following, the further krypton purification is explained along the scan in Figure A.1. In minute 1, the Dewar cooling ACT3 is removed while the trap is still pumped. The following 5 minutes the trap is slowly thawing, releasing the oxygen and argon first, which gets pumped away. Once the krypton signal exceeds the argon signal, the trap is closed and the pump is turned off. Now ACT3 is heated to 100 °C with boiling water and all trapped gas is released into the getter. At minute 8, the oxygen is still the largest gas fraction that was trapped on ACT3. Now the getter is opened and the reactive gasses are chemisorbed. The jump in minute 17 results from a further opening of the dose valve in order to better monitor the process. From minute 22 on, the gas is frozen on $ACT4_{Ar}$ to measure the final krypton purity and amount by comparing it with the krypton standard.

Quantifying pure krypton at the Ar and Kr separation setup

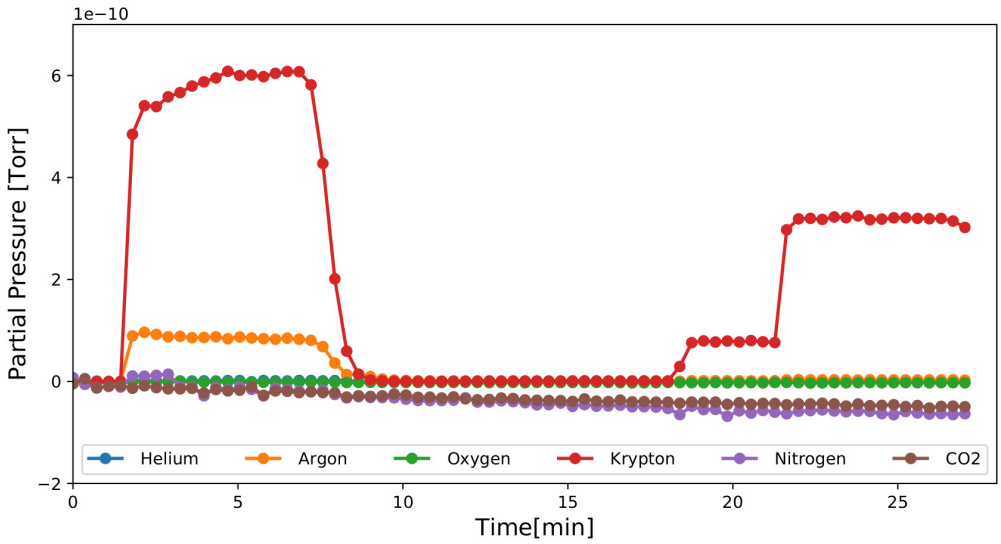

Figure A.2.: The plot displays the measurement of the purified krypton amount with the RGA by comparing the signal with that of the krypton standard.

Figure A.2 illustrates the process of measuring the final krypton amount and purity by using the krypton standard. The krypton peak between minute 1 and 8 results from the purified sample. The ratio of the RGA signals gives the final purity of the sample, which is for this specific sample 92.5 % krypton, 7.3 % argon and 0.2 % helium. The krypton amount is determined by comparing the RGA signal with that of pipettes of the krypton standard of two different sizes. The krypton signal at minute 20 corresponds to a krypton amount of 19.1 μL and the peak around minute 25 corresponds to 81.7 μL of krypton. Extrapolating the two points to the krypton signal of the sample results in a final krypton sample size of (151.3$\pm$2.2) μL.

Tuning the columns of the Ar and Kr separation setup

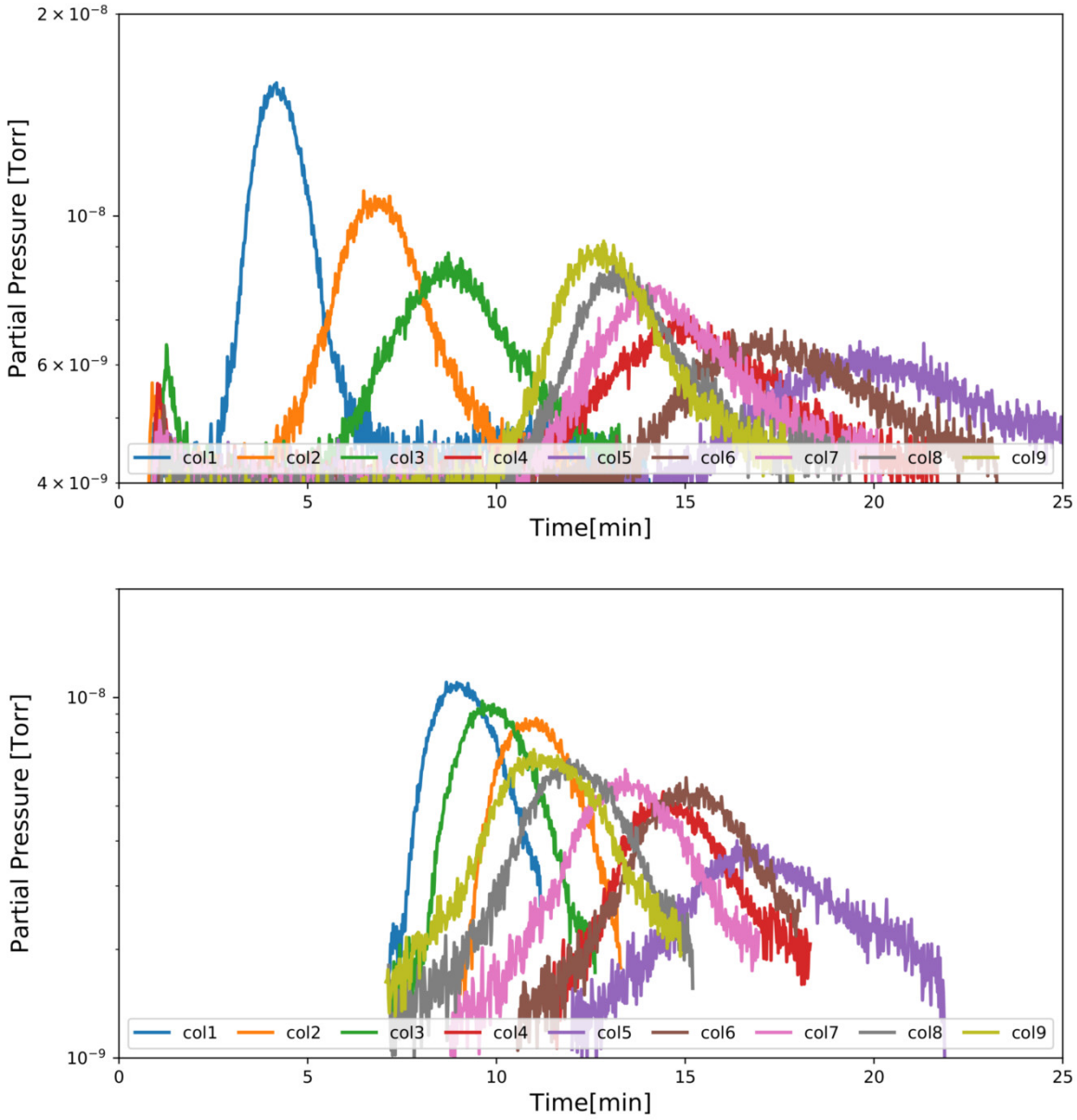

Figure A.3.: The process of tuning the columns is illustrated. In the upper plot the original state is shown. Especially the separation performance of column 1 and 5 diverge significantly leading to an overlap of the rising oxygen peak of column 1 with the argon still leaving column 5. In the lower plot, the column performance has been modified by changing the flow through the single column. This has been achieved by clamping the outlet of the 'faster' columns.

Groundwater study on Rottnest Island

Table A.1.: Results of the Rottnest Island groundwater campaign.

Well	Screen depth	^{85}Kr	SF_6	CFC-11	CFC-12	^{3}H
#	m AHD	dpm/ccKr	fmol/L	pMol/Kg	pMol/Kg	TU
P02-77	0.09	25.1 ± 1.1	8.47 ± 0.21	1.27 ± 0.03	1.04 ± 0.03	0.7 ± 0.03
P01-83	-0.63	29.3 ± 1.3	5.63 ± 0.13	1.95 ± 0.05	1.41 ± 0.05	1.05 ± 0.04
P2-90	-0.55	21.3 ± 1	4.63 ± 0.12	1.74 ± 0.04	1.09 ± 0.04	0.73 ± 0.03
P16-90	-0.7	39.6 ± 1.6	-	0.45 ± 0.01	0.95 ± 0.03	1 ± 0.05
P03-93	-0.51	23.3 ± 2	-	1.87 ± 0.05	1.23 ± 0.04	0.68 ± 0.03
M18-90	-11.27	1.1 ± 0.2	-	0.18 ± ?	0.16 ± ?	0.05 ± ?
M25-90	-6.21	-	-	-	-	0.2 ± 0.05
M15-90	-14.99	-	-	-	-	0.05 ± ?

Well	T	EC	pH	Halon-1301	^{14}C	δ^{13}C
#	°C	μS/cm		fmol/kg	pmc	‰
P02-77	20.8	1098	7.51	4.08 ± 0.16	39.1 ± 0.16	-6.6 ± 0.1
P01-83	21.2	1002	7.53	5.64 ± 0.18	56.9 ± 0.23	-7.3 ± 0.1
P2-90	20.9	1096	7.58	4.26 ± 0.16	37.22 ± 0.16	-6 ± 0.1
P16-90	22.1	1176	7.33	-	71.64 ± 0.31	-8.9 ± 0.1
P03-93	20.4	1250	7.52	-	43.03 ± 0.21	-6.2 ± 0.1
M18-90	20.4	38952	7.24	-	34.29 ± 0.15	-5.8 ± 0.1
M25-90	20.12	28481	7.35	-	-	-
M15-90	21.22	37125	7.37	-	-	-

Well	O_2	He	Ne	Ar	Kr	Xe
#	mg/L	$\times 10^{-8}$[ccSTP/g]	$\times 10^{-7}$[ccSTP/g]	$\times 10^{-5}$[ccSTP/g]	$\times 10^{-8}$[ccSTP/g]	$\times 10^{-9}$[ccSTP/g]
P02-77	1.48	5.43 ± 0.03	2.02 ± 0.08	32.5 ± 0.06	7.16 ± 0.1	9.32 ± 0.05
P01-83	2.02	5.27 ± 0.04	1.97 ± 0.08	32.3 ± 0.060	7.12 ± 0.13	9.35 ± 0.07
P2-90	2.94	15.0 ± 0.10	2.36 ± 0.09	33.9 ± 0.070	7.53 ± 0.14	9.86 ± 0.07
P16-90	3.83	16.0 ± 0.10	5.27 ± 0.21	50.6 ± 0.120	9.40 ± 0.21	1.15 ± 0.09
P03-93	1.97	5.38 ± 0.05	2.00 ± 0.08	32.7 ± 0.060	7.21 ± 0.14	9.40 ± 0.07
M18-90	0.28	4.84 ± 0.02	1.82 ± 0.07	29.4 ± 0.06	6.42 ± 0.08	8.40 ± 0.06
M25-90	0.22	4.95 ± 0.03	1.79 ± 0.07	29.3 ± 0.060	6.63 ± 0.08	8.80 ± 0.06
M15-90	0.47	4.81 ± 0.02	1.78 ± 0.07	28.4 ± 0.060	6.09 ± 0.07	7.90 ± 0.05

Atmospheric ^{85}Kr concentrations

In Figure A.4, polynomials of different degrees are fitted to the lower envelope of the atmospheric ^{85}Kr concentration monitored at the Schauinsland station, and to the southern hemispheric data set. The goodness of the fit does not change significantly anymore for polynomials of a higher degree than 7. Hence, a 7th degree polynomial is chosen for the data evaluation in chapter 5.

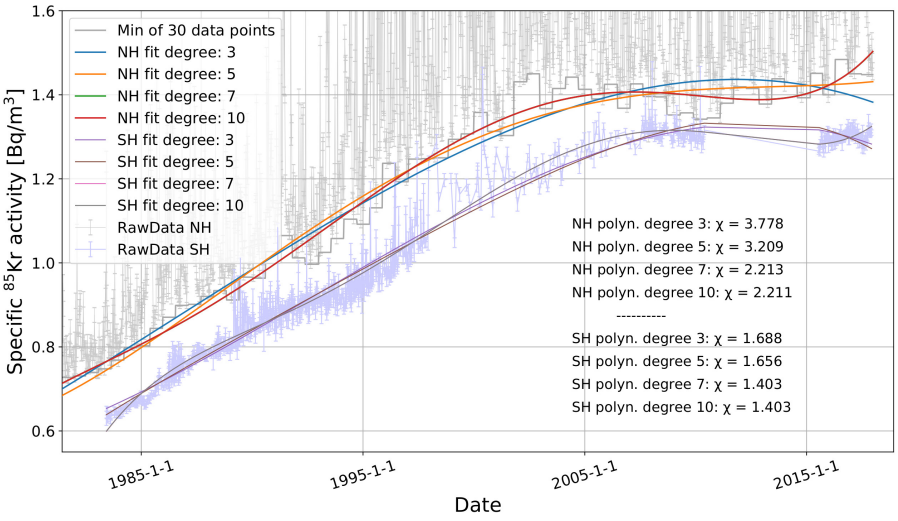

Figure A.4.: Polynomial fits of different degrees are plotted to the lower envelope of the ^{85}Kr concentration monitored at the Schauinsland station and to the southern hemispheric data set.

In Table A.2, the coefficients of the three input functions of the Schauinsland data, the lower envelope of that data and the southern hemisphere data are listed. With a degree of i = 7, the polynomials can be written as:

$$P(x) = \sum_{i=0}^{n} a_i x^i \tag{A.1}$$

Important is, that the x values of the data set are the days since the 1st of January year 0. Hence, date 1.1.1985 is represented by x = 724642.

Table A.2.: Coefficients of the 7th degree polynomial fits that best describe the local input function derived from the Schauinsland data set, the lower envelope of the Schauinsland data set and the southern hemispheric data set are listed.

Fit of:	$\mathbf{a}_0$	$\mathbf{a}_1$	$\mathbf{a}_2$	$\mathbf{a}_3$	$\mathbf{a}_4$	$\mathbf{a}_5$	$\mathbf{a}_6$	$\mathbf{a}_7$
Schauinsland	$1.89{\cdot}10^{-14}$	$-4.52{\cdot}10^{-08}$	$2.43{\cdot}10^{-02}$	$1.57{\cdot}10^{+04}$	$-1.14{\cdot}10^{+10}$	$-9.44{\cdot}10^{+15}$	$9.27{\cdot}10^{+21}$	$-2.05{\cdot}10^{+27}$
NH	$1.12{\cdot}10^{-14}$	$-2.68{\cdot}10^{-08}$	$1.44{\cdot}10^{-02}$	$9.30{\cdot}10^{+03}$	$-6.75{\cdot}10^{+09}$	$-5.60{\cdot}10^{+15}$	$5.51{\cdot}10^{+21}$	$-1.22{\cdot}10^{+27}$
SH	$2.37{\cdot}10^{-14}$	$-5.69{\cdot}10^{-08}$	$3.08{\cdot}10^{-02}$	$1.96{\cdot}10^{+04}$	$-1.45{\cdot}10^{+10}$	$-1.18{\cdot}10^{+16}$	$1.17{\cdot}10^{+22}$	$-2.61{\cdot}10^{+27}$

List of Figures

List of Tables

Bibliography

[1] Aeschbach-Hertig, W: Helium und Tritium als Tracer für physikalische Prozesse in Seen. PhD thesis. ETH Zurich, 1994.

[2] Aeschbach-Hertig, W: Physics of aquatic systems. Part 1 - Lecture notes. 2012.

[3] Aeschbach-Hertig, W and Solomon, D K: Noble gas thermometry in groundwater hydrology. In: *The noble gases as geochemical tracers*. Springer, 2013, pp. 81–122.

[4] Aggarwal, PK: Introduction. Chapter 1 - Isotope methods for dating old groundwater. In: *Isotope methods for dating old groundwater*. 2013.

[5] Aggarwal, PK et al.: Krypton-81, Helium-4 and Carbon-14 based estimation of groundwater ages in the Guarani Aquifer System: implications for the He-4 geochronometer. In: *AGU Fall Meeting Abstracts*. 2012.

[6] Aghedo, A, Rast, S, and Schultz, MG: Sensitivity of tracer transport to model resolution, forcing data and tracer lifetime in the general circulation model ECHAM5. In: *Atmospheric Chemistry and Physics Discussions* 8.1 (2008), pp. 137–160.

[7] Ahlswede, J et al.: Update and improvement of the global krypton-85 emission inventory. In: *Journal of environmental radioactivity* 115 (2013), pp. 34–42.

[8] Alley, W M et al.: Flow and storage in groundwater systems. In: *science* 296.5575 (2002), pp. 1985–1990.

[9] Allison, GB and Hughes, MW: The history of tritium fallout in southern Australia as inferred from rainfall and wine samples. In: *Earth and Planetary Science Letters* 36.2 (1977), pp. 334–340.

[10] Appelo, C A J and Postma, D: Geochemistry, groundwater and pollution. CRC press, 2004.

[11] Assouline, S: Infiltration into soils: Conceptual approaches and solutions. In: *Water Resources Research* 49.4 (2013), pp. 1755–1772.

[12] Baglin, C M: Nuclear data sheets update for A= 81. In: *Nuclear Data Sheets* 69.2 (1993), pp. 267–373.

[13] Barlow, P M: Ground Water in fresh water-salt water environments of the Atlantic. Vol. 1262. Geological Survey (USGS), 2003.

[14] Bauer, M R and Yavitt, J B: Processes and mechanisms controlling consumption of CFC-11 and CFC-12 by peat from a conifer-swamp and black spruce-tamarack bog in New York State. In: *Chemosphere* 32.4 (1996), pp. 759–768.

[15] Benetti, P et al.: Measurement of the specific activity of 39Ar in natural argon. In: *Nuclear Instruments and Methods in Physics Research Section A: Accelerators, Spectrometers, Detectors and Associated Equipment* 574.1 (2007), pp. 83–88.

[16] Benson, B B and Krause Jr, D: Empirical laws for dilute aqueous solutions of nonpolar gases. In: *The Journal of Chemical Physics* 64.2 (1976), pp. 689–709.

[17] Benson, C-S: Stratigraphic studies in the snow and firn of the Greenland ice sheet. In: (1962).

[18] Beyer, M et al.: Halon-1301–further evidence of its performance as an age tracer in New Zealand groundwater. In: *Hydrology and Earth System Sciences* 21.8 (2017), p. 4213.

[19] Beyer, M et al.: Potential groundwater age tracer found: Halon-1301 (CF3Br), as previously identified as CFC-13 (CF3Cl). In: *Water Resources Research* 50.9 (2014), pp. 7318–7331.

[20] Beyersdorfer, S: Argon extraction from glacier ice and ocean water for dating with 39Ar - ATTA. MA thesis. Germany: Heidelberg University, 2016.

[21] Bollhöfer, A et al.: Variability of atmospheric krypton-85 activity concentrations observed close to the ITCZ in the southern hemisphere. In: *Journal of environmental radioactivity* 127 (2014), pp. 111–118.

[22] BOM: *Australian Government Bureau of Meteorology - Climate Averages Tables, Rottnest Island*. 2018. URL: http://www.bom.gov.au/climate/averages/tables/cw_009038_All.shtml (visited on 02/13/2018).

[23] Brosi, AR, Zeldes, H, and Ketelle, BH: Argon 39 Beta-Spectrum. In: *Physical Review* 79.5 (1950), p. 902.

[24] Bryan, E, Meredith, K T, Baker, A, Andersen, M S, et al.: Carbon dynamics in a Late Quaternary-age coastal limestone aquifer system undergoing saltwater intrusion. In: *Science of The Total Environment* 607 (2017), pp. 771–785.

[25] Bryan, E, Meredith, K T, Baker, A, Post, V E, et al.: Island groundwater resources, impacts of abstraction and a drying climate: Rottnest Island, Western Australia. In: *Journal of Hydrology* 542 (2016), pp. 704–718.

[26] Buizert, C et al.: Radiometric 81Kr dating identifies 120,000-year-old ice at Taylor Glacier, Antarctica. In: *Proceedings of the National Academy of Sciences* 111.19 (2014), pp. 6876–6881.

[27] Burnard, P et al.: The Noble Gases as Geochemical Tracers. Springer, 2013.

[28] Busenberg, E and Plummer, L N: Dating groundwater with trifluoromethyl sulfurpentafluoride (SF5CF3), sulfur hexafluoride (SF6), CF3Cl (CFC-13), and CF2Cl2 (CFC-12). In: *Water Resources Research* 44.2 (2008).

[29] Busenberg, E and Plummer, L N: Dating young groundwater with sulfur hexafluoride: Natural and anthropogenic sources of sulfur hexafluoride. In: *Water Resources Research* 36.10 (2000), pp. 3011–3030.

[30] Chen, CY et al.: Ultrasensitive isotope trace analyses with a magneto-optical trap. In: *Science* 286.5442 (1999), pp. 1139–1141.

[31] Clark, I D and Fritz, P: Environmental isotopes in hydrogeology. CRC press, 1997.

[32] Collon, P, Kutschera, W, Loosli, H H, et al.: 81 Kr in the Great Artesian Basin, Australia: a new method for dating very old groundwater. In: *Earth and Planetary Science Letters* 182.1 (2000), pp. 103–113.

[33] Collon, P, Kutschera, W, and Lu, Z-T: Tracing noble gas radionuclides in the environment. In: *Annu. Rev. Nucl. Part. Sci.* 54 (2004), pp. 39–67.

[34] Cuffey, K M and Paterson, W S B: The physics of glaciers. Academic Press, 2010.

[35] Database, The GNIP. 2012. URL: http://www.iaea.org/water.

[36] Domenico, P A and Schwartz, F W: Physical and chemical hydrogeology. Vol. 506. Wiley New York, 1998.

[37] Dwyer, G S, Cronin, T M, and Baker, P A: Trace elements in marine ostracodes. In: *The Ostracoda: Applications in Quaternary Research* (2002), pp. 205–225.

[38] Ebser, S: Dating of Ice and Ocean Samples with Argon Trap Trace Analysis of 39Ar. 2018.

[39] Emery, W J and Meincke, J: Global water masses-summary and review. In: *Oceanologica acta* 9.4 (1986), pp. 383–391.

[40] Felsberg, A et al.: Simulating the mesoscale transport of krypton-85. In: *Journal of environmental radioactivity* 181 (2018), pp. 85–93.

[41] Firestone, R B et al.: Table of Isotopes, 8-th ed. In: *John Willey & Sons, New York* (1996).

[42] Godwin, H: Half-life of radiocarbon. In: *Nature* 195.4845 (1962), p. 984.

[43] Group, SAES: Datasheet for CapaciTorr HV 200. URL: https://www.saesgetters.com/sites/default/files/Capacitorr%20Pumps%20datasheet%20HV%20200.pdf (visited on 01/30/2018).

[44] Hall, T M and Plumb, R A: Age as a diagnostic of stratospheric transport. In: *Journal of Geophysical Research: Atmospheres* 99.D1 (1994), pp. 1059–1070.

[45] Hebert, D: Tritium in precipitation of Vostok (Antarctica): conclusions on the tritium latitude effect. In: *Isotopes in environmental and health studies* 47.3 (2011), pp. 265–272.

[46] Hoffmann, H: Micro radiocarbon dating of the particulate organic carbon fraction in Alpine glacier ice: method refinement, critical evaluation and dating applications. PhD thesis. 2016.

[47] Hunter, J D: Matplotlib: A 2D graphics environment. In: *Computing in science & engineering* 9.3 (2007), pp. 90–95.

[48] Ice Group Data Base. Institute for Environmental Physics, 2017.

[49] Jiang, W. et al.: An atom counter for measuring 81Kr and 85Kr in environmental samples. In: *Geochimica et Cosmochimica Acta* 91.Supplement C (2012), pp. 1–6. ISSN: 0016-7037. DOI: https://doi.org/10.1016/j.gca.2012.05.019. URL: http://www.sciencedirect.com/science/article/pii/S0016703712003067.

[50] Jurgens, B C, Böhlke, J K, and Eberts, S M: *TracerLPM (Version 1): An Excel® workbook for interpreting groundwater age distributions from environmental tracer data*. Tech. rep. US Geological Survey, 2012.

[51] Katz, B G, Böhlke, J K, and Hornsby, H D: Timescales for nitrate contamination of spring waters, northern Florida, USA. In: *Chemical Geology* 179.1-4 (2001), pp. 167–186.

[52] Kaufman, S and Libby, W F: The natural distribution of tritium. In: *Physical Review* 93.6 (1954), p. 1337.

[53] Keller, J U and Staudt, R: Gas adsorption equilibria: experimental methods and adsorptive isotherms. Springer Science & Business Media, 2005.

[54] Kersting, A: A new method of krypton purification for groundwater dating with atom trap trace analysis. MA thesis. Germany: Heidelberg University, 2013.

[55] Kersting, A: Manual for the argon and krypton separation setup. 2016.

[56] Kuhlbrodt, T et al.: On the driving processes of the Atlantic meridional overturning circulation. In: *Reviews of Geophysics* 45.2 (2007).

[57] Kutschera, W et al.: Long-lived noble gas radionuclides. In: *Nuclear Instruments and Methods in Physics Research Section B: Beam Interactions with Materials and Atoms* 92.1-4 (1994), pp. 241–248.

[58] Langmuir, I: The adsorption of gases on plane surfaces of glass, mica and platinum. In: *Journal of the American Chemical society* 40.9 (1918), pp. 1361–1403.

[59] Leibundgut, C, Maloszewski, P, Külls, C, et al.: Tracers in hydrology. Wiley Online Library, 2009.

[60] Lepple, F K and Millero, F J: The isothermal compressibility of seawater near one atmosphere. In: *Deep Sea Research and Oceanographic Abstracts*. Vol. 18. 12. Elsevier. 1971, pp. 1233–1254.

[61] Levin, I and Hesshaimer, V: Radiocarbon–a unique tracer of global carbon cycle dynamics. In: *Radiocarbon* 42.1 (2000), pp. 69–80.

[62] Levin, I and Hesshaimer, V: Refining of atmospheric transport model entries by the globally observed passive tracer distributions of 85krypton and sulfur hexafluoride (SF6). In: *Journal of Geophysical Research: Atmospheres* 101.D11 (1996), pp. 16745–16755.

[63] Lewis, E: The practical salinity scale 1978 and its antecedents. In: *IEEE Journal of Oceanic Engineering* 5.1 (1980), pp. 3–8.

[64] Loosli, H H: A dating method with39Ar. In: *Earth and Planetary Science Letters* 63.1 (1983), pp. 51–62.

[65] Loosli, H H: Argon-39: A tool to investigate ocean water circulation and mixing. In: *Handbook of environmental isotope geochemistry* 3 (1989), pp. 385–392.

[66] Loosli, H H, Heimann, M, and Oeschger, H: Low-Level gas proportional counting in an underground laboratory. In: *Radiocarbon* 22.2 (1980), pp. 461–469.

[67] Loosli, H H, Lehmann, B E, and Balderer, W: Argon-39, argon-37 and krypton-85 isotopes in Stripa groundwaters. In: *Geochimica et Cosmochimica Acta* 53.8 (1989), pp. 1825–1829.

[68] Loosli, H H and Oeschger, H: 37Ar and 81Kr in the atmosphere. In: *Earth and Planetary Science Letters* 7.1 (1969), pp. 67–71.

[69] Lott, D E: Improvements in noble gas separation methodology: A nude cryogenic trap. In: *Geochemistry, Geophysics, Geosystems* 2.12 (2001).

[70] Lower, S: *Catalysts and catalysis*. 2017. URL: https://chem.libretexts.org/Textbook_Maps/General_Chemistry_Textbook_Maps/Map%3A_Chem1_(Lower)/17%3A_Chemical_Kinetics_and_Dynamics/17.6%3A_Catalysts_and_catalysis (visited on 01/28/2018).

[71] Lu, Z-T et al.: Tracer applications of noble gas radionuclides in the geosciences. In: *Earth-science reviews* 138 (2014), pp. 196–214.

[72] Lucas, L L and Unterweger, M P: Comprehensive review and critical evaluation of the half-life of Tritium. In: *Journal of research of the National Institute of Standards and Technology* 105.4 (2000), p. 541.

[73] McDougall, TJ et al.: The International Thermodynamic Equation Of Seawater 2010 (TEOS-10): Calculation and Use of Thermodynamic Properties. In: *Global Ship-based Repeat Hydrography Manual, IOCCP Report No* 14 (2009).

[74] Meyer, RA et al.: Level properties of Rb 48 37 85 from the decay of the Kr 85 and Sr 85 isomers and the cluster-vibration model. In: *Physical Review C* 21.6 (1980), p. 2590.

[75] Millero, F J: History of the equation of state of seawater. In: *Oceanography* 23.3 (2010), pp. 18–33.

[76] Müller, F: Zonation in the accumulation area of the glaciers of Axel Heiberg Island, NWT, Canada. In: *Journal of Glaciology* 4.33 (1962), pp. 302–311.

[77] National, Groundwater Association: Groundwater facts. 2015.

[78] Oeschger, H et al.: 39 Ar dating of groundwater. In: *Isotope techniques in groundwater hydrology 1974, Vol. II. Proceedings of a symposium*. 1974.

[79] Oster, H, Sonntag, C, and Münnich, K O: Groundwater age dating with chlorofluorocarbons. In: *Water Resources Research* 32.10 (1996), pp. 2989–3001.

[80] Pickard, G L and Emery, W J: Descriptive physical oceanography: an introduction. Elsevier, 2016.

[81] Playford, P E, Leech, R E J, and Kendrick, G W: Geology and hydrology of Rottnest Island. Vol. 6. Geological Survey of Western Australia, 1977.

[82] Plummer, L N and Glynn, P D: Radiocarbon dating in groundwater systems. In: *Isotope methods for dating old groundwater* (2013), pp. 33–89.

[83] Plummer, L N, Busenberg, E, Cook, P G, et al.: Use of Chlorofluorocarbons in Hydrology. In: *International Atomic Energy Agency* (2006).

[84] Purtschert, R, Yokochi, R, and Sturchio, N C: Krypton-81 dating of old groundwater. Chapter 5. In: *Isotope methods for dating old groundwater*. 2013.

[85] Reardon, E J: Anaerobic corrosion of granular iron: Measurement and interpretation of hydrogen evolution rates. In: *Environmental Science & Technology* 29.12 (1995), pp. 2936–2945.

[86] Reichel, T: Groundwater degassing and separation of argon from air for 39Ar dating with ATTA. PhD thesis. 2013.

[87] Reimer, P J et al.: IntCal09 and Marine09 radiocarbon age calibration curves, 0–50,000 years cal BP. In: *Radiocarbon* 51.4 (2009), pp. 1111–1150.

[88] Reynolds, J H: A new long-lived krypton activity. In: *Physical Review* 79.5 (1950), p. 886.

[89] Riedmann, R A: Separation of Argon from atmospheric air and measurements of 37Ar for CTBT purposes. PhD thesis. Universität Bern, 2011.

[90] Riedmann, R A and Purtschert, Roland: Separation of argon from environmental samples for Ar-37 and Ar-39 analyses. In: *Separation and Purification Technology* 170 (2016), pp. 217–223.

[91] Ritterbusch, F. personal communication. Feb. 10, 2018.

[92] Ritterbusch, F: Dating of groundwater with atom trap trace analysis of 39 Ar. PhD thesis. 2014.

[93] Ritterbusch, F et al.: Groundwater dating with Atom Trap Trace Analysis of39Ar. In: *Geophysical Research Letters* 41.19 (2014), pp. 6758–6764.

[94] Rodriguez, J: Beiträge zur Verteilung von 39Ar im Atlantik. PhD thesis. 1993.

[95] Ross, O, Schluenzen, K H, and Kalinowski, M B: Simulation of atmospheric krypton-85 transport to assess the detectability of clandestine nuclear reprocessing. PhD thesis. Hamburg University Hamburg, 2010.

[96] Schlitzer, R et al.: A meridional 14C and 39Ar section in northeast Atlantic deep water. In: *Journal of Geophysical Research: Oceans* 90.C4 (1985), pp. 6945–6952.

[97] Schlosser, C et al.: Analysis of radioxenon and Krypton-85 at the BfS noble gas laboratory. In: *Applied Radiation and Isotopes* (2016).

[98] Schneider, A et al.: An evaluation of tracer fields and anthropogenic carbon in the equatorial and the tropical North Atlantic. In: *Deep Sea Research Part I: Oceanographic Research Papers* 67 (2012), pp. 85–97.

[99] Schneider, A et al.: Changes in ventilation of the Mediterranean Sea during the past 25 year. In: *Ocean Science* 10.1 (2014), pp. 1–16.

[100] Schwefel, R: Methoden zur Probenaufbereitung von Eis- und Grundwasserproben zur 39Ar-Datierung mittels atom trap trace analysis. MA thesis. Germany: Heidelberg University, 2011.

[101] Schwerdtfeger, P: Table of experimental and calculated static dipole polarizabilities for the electronic ground states of the neutral elements (in atomic units). In: *Centre for Theoretical Chemistry and Physics, Massey University* (2015).

[102] Smith, A et al.: Geohydrology of the Tamala Limestone Formation in the Perth Region: Origin and role of secondary porosity. In: (2012).

[103] Smíšek, M and Černỳ, S: Active carbon: manufacture, properties and applications. Vol. 12. Elsevier Publishing Company, 1970.

[104] Solomon, D K and Cook, P G: 3h and 3he. In: *Environmental tracers in subsurface hydrology*. Springer, 2000, pp. 397–424.

[105] Stanley, R HR et al.: Noble gas constraints on air-sea gas exchange and bubble fluxes. In: *Journal of Geophysical Research: Oceans* 114.C11 (2009).

[106] Steinfeldt, R et al.: Inventory changes in anthropogenic carbon from 1997–2003 in the Atlantic Ocean between 20 S and 65 N. In: *Global Biogeochemical Cycles* 23.3 (2009).

[107] Stewart, R H: Introduction to physical oceanography. Robert H. Stewart, 2008.

[108] Stone, N J: Table of nuclear magnetic dipole and electric quadrupole moments. In: *Atomic Data and Nuclear Data Tables* 90.1 (2005), pp. 75–176.

[109] Stout, V L and Gibbons, M D: Gettering of gas by titanium. In: *Journal of applied physics* 26.12 (1955), pp. 1488–1492.

[110] Stöven, T and Tanhua, T: Ventilation of the Mediterranean Sea constrained by multiple transient tracer measurements. In: *Ocean Science* 10 (2014), pp. 439–457.

[111] Stramma, L et al.: The flow field of the upper hypoxic eastern tropical North Atlantic oxygen minimum zone. In: *Ocean Science* 12.1 (2016), pp. 153–167.

[112] Sturchio, N C et al.: One million year old groundwater in the Sahara revealed by krypton-81 and chlorine-36. In: *Geophysical Research Letters* 31.5 (2004).

[113] Styra, B I and Butkus, D: Geophysical problems of Krypton-85 in the atmosphere. In: (1991).

[114] Suckow, A: Lumpy - Lumped Parameter Modelling of Age Distributions using up to two Parallel Black Boxes. 2014.

[115] Suckow, A: The age of groundwater–definitions, models and why we do not need this term. In: *Applied geochemistry* 50 (2014), pp. 222–230.

[116] Suess, H E: Radiocarbon concentration in modern wood. In: *Science* 122.3166 (1955), pp. 415–417.

[117] Tadros, C V et al.: Tritium in Australian precipitation: A 50 year record. In: *Journal of hydrology* 513 (2014), pp. 262–273.

[118] Tomczak, M: Some historical, theoretical and applied aspects of quantitative water mass analysis. In: *Journal of Marine Research* 57.2 (1999), pp. 275–303.

[119] Torgersen, T et al.: Chlorine 36 dating of very old groundwater: 3. Further studies in the Great Artesian Basin, Australia. In: *Water Resources Research* 27.12 (1991), pp. 3201–3213.

[120] Tu, L-Y et al.: Analysis of Krypton-85 and Krypton-81 in a few liters of air. In: *Analytical chemistry* 86.8 (2014), pp. 4002–4007.

[121] Visbeck, M: Oxygen in the Tropical Atlantic OSTRE Third Tracer Survey: Cruise No. M116/1. In: (2016).

[122] Vogel, J C: Investigation of groundwater flow with radiocarbon. In: *pp 355-69 of Isotopes in Hydrology. Vienna, International Atomic Energy Agency, 1967.* (1968).

[123] Von Hippel, F, Albright, D H, and Levi, B G: Stopping the production of fissile materials for weapons. In: *Scientific American* 253.3 (1985), pp. 40–47.

[124] Wagenbach, D et al.: Ice block sampling at Gorner Glacier. In: (2014).

[125] Waugh, D W, Hall, T M, and Haine, T W: Relationships among tracer ages. In: *Journal of Geophysical Research: Oceans* 108.C5 (2003).

[126] Weiss, R F: The solubility of nitrogen, oxygen and argon in water and seawater. In: *Deep Sea Research and Oceanographic Abstracts*. Vol. 17. 4. Elsevier. 1970, pp. 721–735.

[127] Welte, J: Atom Trap Trace Analysis of 39Ar. PhD thesis. PhD thesis, Universität Heidelberg, 2011.

[128] Winger, K et al.: A new compilation of the atmospheric 85 krypton inventories from 1945 to 2000 and its evaluation in a global transport model. In: *Journal of environmental radioactivity* 80.2 (2005), pp. 183–215.

[129] Yang, G-M et al.: Analysis of 85Kr: a comparison at the 10-14 level using micro-liter samples. In: *Scientific reports* 3 (2013).

[130] Yang, R T: Adsorbents: fundamentals and applications. John Wiley & Sons, 2003.

[131] Zeldes, H, Ketelle, BH, and Brosi, AR: Radiations of Krypton 85. In: *Physical Review* 79.5 (1950), p. 901.

Acknowledgment

Many people have supported me over the past three years and contributed in one or the other way to the successful completion of my thesis.

Zuallererst gebührt mein Dank meinem Betreuer Prof. Dr. Werner Aeschbach, der mich seit meinem ersten Tag am IUP als Diplomstudent bei all meinem Tun immer konstruktiv unterstützt hat. Für die angenehme Arbeitsatmosphäre, die lehrreichen fachlichen Unterhaltungen, das Schach während der Weihnachtsfeiern und seinem Besuch in Australien.

Weiter danke ich Prof. Dr. Norbert Frank für die Übernahme meines Zweitgutachtens und für manch lehrreiches Gespräch in der Küche des IUP.

Mein ganz besonderer Dank gilt Axel Suckow, meinem Betreuer und Freund am CSIRO in Adelaide. Für die unzählbaren und oft kontroversen Diskussionen über im Grunde jedes Thema und für das Teilhabenlassen an seinem großen Erfahrungsschatz auf dem Gebiet der Grundwasserhydrologie.

Vielen Dank an die Mitglieder aller drei Arbeitsgruppen, von denen ich Teil sein durfte: Danke an die Grundwasser- und Paläoklimagruppe für die wunderbare Arbeitsatmosphäre, fürs sommerliche Grillen, die legendären Weihnachtsfeiern und das allmittägliche Essen in der Mensa. Danke an die ArTTA-Crew des KIPs für die angenehme Zusammenarbeit, den fachlichen Austausch und das hoffentlich nicht einzige ArTTA-Dinner. Besonderer Dank an Sven Ebser, der seinen Sommer 2017 geopfert hat, um im Labor 90 Tage rund um die Uhr die Ozeanproben zu messen!

Thanks to everybody at the CSIRO I worked with, for making my year in Adelaide a very pleasant experience. Special thanks to Alec Deslandes for being a wonderful colleague and friend, and for introducing me to Rogaines.

Vielen Dank an meine Bürokolleg*innen Ben, Josef, Florian und Flora(!) für die spaßige Atmosphäre und den Glühwein im Dezember.

Danke an Simon Mayer, Therese Weißbach, Florian Jenner, Benno Beck, Stefan Beyersdorfer, Emeline Mathouchanh, Philip Hopkins und Viola Rädle dafür, dass ihr meinen Alltag am IUP ungemein bereichert habt und mehr Freund*innen als Kolleg*innen wart.

Einen besonderen Dank an Florian Ritterbusch, zum einen für das Korrekturlesen meine kompletten Dissertation und die konstruktive Kritik, zum anderen für die angenehme Zusammenarbeit im ersten Jahr meiner Promotion und für all die teils unangenehmen Arbeiten, bei denen er mich unterstützt hat.

Einen riesigen Dank an alle meine weiteren Korrekturleser*innen: Gaia, Simon, Viola, Max, Ben und Axel für die hilfreichen Verbesserungen, Kommentare und Anmerkungen.

Merci Emeline pour ton amitié pendant ton séjour à l'IUP et en Australie. Pour toutes les parties sauvages, les belles conversations et la danse amusante!

Einen ganz besonderen Dank verdienen meine lieben Mittbewohner*innen, die mich in meiner Zeit des Schreibens von allen häuslichen Pflichten entbunden haben (die ich sonst immer gewissenhaft erledige).

Und nicht zuletzt vielen Dank an meine drei Eltern Annette, Jürgen und Uli und meinen Lieblingsbruder Daniel, dass ihr mich mein ganzes Leben lang in allem was ich getan habe unterstützt habt.